FLORIDA INTERNATIONAL UNIVERSITY

Miami, Florida

DEVELOPMENT AND OPTIMIZATION OF ADAPTIVE VOLTAGE AND FREQUENCY CONTROLLERS IN HYBRID MICROGRID

A dissertation submitted in partial fulfillment of the

requirements for the degree of

DOCTOR OF PHILOSOPHY

in

ELECTRICAL AND COMPUTER ENGINEERING

by

Anjan Debnath

2023

To: Dean John L. Volakis
College of Engineering and Computing

This dissertation, written by Anjan Debnath, and entitled Development and Optimization of Adaptive Voltage and Frequency Controllers in Hybrid Microgrid, having been approved in respect to style and intellectual content, is referred to you for judgment.

We have read this dissertation and recommend that it be approved.

Sumit Paudyal

Nezih Pala

Norman Munroe

Arif Sarwat, Major Professor

Date of Defense: June 22, 2023

The dissertation of Anjan Debnath is approved.

Dean John L. Volakis
College of Engineering and Computing

Andrés G. Gil
Vice President for Research and Economic Development
and Dean of the University Graduate School

Florida International University, 2023

DEDICATION

Dedicated to my parents and my wife for their boundless support.

ACKNOWLEDGMENTS

My dissertation could not have been completed without the support of my advisor, committee members, colleagues, friends, and family. I am extremely grateful to my major professor, Dr. Arif Sarwat, for providing me the opportunity to join the Energy, Power, and Sustainability-Intelligenace (EPSi) Group, giving motivation and encouragement throughout my research, and allowing me to conduct independent research and assisting me to progress as a researcher over the past three and half years. I am also appreciative of the support, insightful comments, and constructive suggestions from my committee members: Dr. Sumit Paudyal, Dr. Nezih Pala, and Dr. Norman Munroe, especially during my proposal defense. I am also grateful to the EPS Group members - Dr. Temitayo Olowu, Dr. Imtiaz Parvez, Hugo Riggs, Sukanta Roy, and Alexander Stevenson who fostered a collaborative work environment, and the staff of the Electrical and Computer Engineering Department who provided excellent student services. I am grateful to the National Science Foundation (NSF) and FIU graduate school's doctoral DYF fellowship for providing partial research funding without which my work would not have been possible.

Last, but not least, I want to dedicate my dissertation to my parents for their love and support towards my academic pursuits.

ABSTRACT OF THE DISSERTATION

DEVELOPMENT AND OPTIMIZATION OF ADAPTIVE VOLTAGE AND FREQUENCY CONTROLLERS IN HYBRID MICROGRID

by

Anjan Debnath

Florida International University, 2023

Miami, Florida

Professor Arif Sarwat, Major Professor

A microgrid, associated with Distributed Energy Resources (DERs), is subject to voltage and frequency fluctuations due to the dependency on weather parameters, besides voltage deviations due to load side variations which could create instability in both the AC and DC sides of AC-DC microgrids. In that regard, this dissertation is aimed at developing adaptive controllers to regulate the voltage and frequency of PV-based microgrids. For voltage regulation, the dissertation proposes a new control strategy to unify maximum power point tracking (MPPT) from photovoltaic (PV) arrays and voltage regulation (VR) in a load-adaptive way where PV has been utilized as a voltage source. An Artificial Neural Network (ANN) is used to determine the Maximum Power Point (MPP) of the PV system, and a DC-DC buck converter with the proposed control technique is used to regulate the DC bus voltage at the desired operating point. The effectiveness of the proposed control strategy is demonstrated by varying irradiance from the input side and load variations from the output side. For frequency regulation, this dissertation proposes a novel method of frequency regulation for power systems with high penetration of inverter-based renewable energy resources, such as Photovoltaic (PV) systems. The method generates virtual inertia (VI) based on the frequency dynamics of the system using the conventional swing equation and feeds an Artificial Neural Network (ANN) to de-

termine the corresponding operating point for the PV. Simulation results show that the proposed control mechanism provides high accuracy, and a fast-tracking speed, and has the potential to significantly improve stability during frequency disturbance in PV-based power systems.

In addition, the dissertation proposes a hierarchical control strategy for islanded microgrids that prioritizes PV as the primary control and battery as the secondary control for dynamic frequency regulation. The PV operating point on the P-V curve is determined based on frequency deviation, and the battery control is activated to avoid moving the PV outside a predefined region. The control parameters of the local controllers for PV and battery are optimized by the particle swarm optimization (PSO) algorithm and simulations show the proposed architecture reduces battery cycling, increases longevity, and reduces overall system cost.

Moreover, the dissertation also explored and proposed a straight-line-based simple MPPT algorithm to extract maximum power from PV with high efficiency for rapidly changing weather parameters, a binary search algorithm for optimal sizing of photovoltaic and energy storage systems with annual zero load deficit constraint, and particle swarm optimization (PSO)-based PID controller design for converters and inverters with faster settling time and reduced transients- overshoots and undershoots of the response signals.

TABLE OF CONTENTS

CHAPTER PAGE

LIST OF FIGURES

CHAPTER 1

INTRODUCTION

There is always some level of uncertainty in load demand as well as unpredictability associated with renewable energy-based resources that can challenge the current microgrid system. Most of the loads are rated for some nominal operating voltage and if a large deviation occurs at the load side voltage – this could cause damage or malfunction of the loads. The disturbances either from the load side or change in irradiance or temperature might have the potential in collapsing the DC bus voltage, subsequently will create a drop in the ac side as well for ac-dc microgrids. The majority of the currently installed PV sources operate in the maximum power point tracking (MPPT) mode. They directly regulate PV currents and turn PV converters into current sources. The power balance is maintained by other equipment in the microgrid, such as energy storage systems (ESS) or grid-connected converters, using these control approaches. Unfortunately, as PV penetration rises, maximum power point tracking (MPPT) controllers may put system stability in jeopardy. A simple solution to the problem could be to increase the capacity of ESS. On the other side, increasing the ESS's capacity may increase the system's investment and maintenance expenses. The charging of ESS, on the other hand, is restricted by the charging power constraint as well as the level of charge (SOC). As a result, the necessity for PV to participate in voltage regulation mode is essential and contributes to system stability apart from the fact the PV controllers extract maximum power in the current-source control mode. Utilizing PV as a voltage source would help reduce the size of ESS, thereby reducing overall system cost. This case is also applicable for grid-following (GFL) inverters where also the PV source acts as a current source and export maximum power to the grid or in other words, works as MPPT mode. This current source-based PV control is suitable for grid-connected mode

because grid voltage is usually stiff and PV source can always provide maximum power based on the grid voltage set points. However, when there is grid-outage occurs and bulk-grid remains absent, this type of GFL inverter cannot provide voltage and frequency regulation during this islanding mode. So, one of the main goals in microgrids is the regulation of voltage and frequency to the previously defined reference points with some degree of robustness to tackle the disturbances in the system. Therefore, a control structure is necessary where PV can be treated as a voltage source and capable of maintaining bus voltage stability for dc microgrid and voltage and frequency stability for ac microgrid during the load transients and input side weather variations such as irradiance and temperature. From the controller's perspective, a fast maximum power point (MPP) tracker with optimal step size for smooth and fluctuating irradiance is also a necessity for extracting the maximum power from the PV modules. Based on the MPPT controller's reference points, an optimal controller with less transients, overshoots and faster response are desirable for the converter in order to transfer energy.

1.0.1 Proposed Implementation approach

In order to tackle the aforementioned issues, this dissertation proposes the following approach for implementation:

The proposed MPPT algorithm has the capability of reaching the MPP very fast and after reaching the MPP, it does have minimum oscillations around the MPP – that would make it suitable for the rapidly changing weather parameters. In addition, the proposed algorithm is the module independent and has the capability of easy implementation. The ability of the proposed algorithm has been further enhanced by an iterative-based optimal step size algorithm to achieve fast dynamic response as well as maximum energy extraction from the overall system with

higher efficiency. Then, in order to optimize a PV-battery system, a binary-search algorithm-based PV-plus-Battery system is proposed for optimally determining the appropriate number of PVs and batteries for a given load conditions. Practical load data has been utilized with the consideration of area constraints for the PVs and Battey energy sources. Another objective of the proposed algorithm is to make the total load rejection zero with minimum overall system cost throughout the year. Then in order to address the voltage regulation problem for the microgrid, a single-stage PV-based voltage source controller is designed with a battery energy source for voltage regulation of the DC-link capacitor. In order to check the robustness of the PV-based controller, step change irradiance and step change load scenarios are checked during the condition when PV power is higher than the load power and the battery is fully charged and remains idle - not capable of taking the surplus. The disconnection prevents the battery from being overcharged, thereby prolonging the lifetime of the battery. This concept is further enhanced by designing a unified controller to combine the voltage regulation and MPPT modes with the help of a single reference control signal for both grid-connected or battery-connected and islanding modes. This concept is also applied to a DC-AC microgrid in an islanding mode where the voltage regulation of the DC capacitor is controlled by the unified control mechanism, i.e. MPP and voltage regulation by single control signal - where MPP control was governed by ANN predictor.

In order for achieving better performance with minimum overshoot and fast settling time, the controllers' parameters are optimized by a metaheuristic algorithm: particle swarm optimization (PSO). The objective of the optimization is to compare 4 different cost functions: The integral of Absolute Error (IAE), Integral of Square Error (ISE), Integral of Time-weighted Square Error (ITSE) and Integral of Square Time-weighted Squared Error (ISTSE) in order to check which cost or fitness func-

tion out of these four performed best in terms of reducing the transient effects. The best cost function is then utilized to determine the optimal control parameters of the converters.

Besides voltage regulation of microgrid, the dissertation explored frequency regulation by the implementation of an artificial neural network (ANN).

1.1 Literature Review

Due to the weather-dependence of power generation from photovoltaic (PV) systems and the relatively lower efficiency of PV modules (compared to other sources of power generation), extracting maximum power from PV systems (at varying weather conditions) becomes highly imperative [1]. Maximum power point tracking (MPPT) algorithms are usually developed to enable PV systems to operate at maximum power by varying the operating voltage at varying weather conditions. There are lots of algorithms proposed in the literature. In [2], an optimization-based P&O is analyzed for harnessing maximum energy. The authors also used SVM for the classification of irradiance data from two places. In [3], the authors proposed a new algorithm for the sudden change of irradiance. Their algorithm is divided into two: current perturbation and adaptive control algorithm. The authors of [4] use a variable step size-based P&O algorithm in order to reduce the oscillations around the MPP.

In order to track the point of maximum power along a PV system (based on the widely used perturb and observe algorithm) operating P-V curve, the optimal step size is needed in order to maximize the total PV energy generation and improve the dynamic response of the PV system[2, 5–10] with varying weather conditions. The authors in [11] use adaptive auto-tuning-based Incremental Conductance (InC)

MPPT algorithm in a photovoltaic system. The step size and perturbation frequency are adaptive in nature in the proposed algorithm and they have shown that the proposed algorithm reduces the steady state and dynamic oscillations of the overall system. In [12], the authors proposed an optimization algorithm that can adjust the step size of the MPPT algorithm automatically. They have also studied convergence, stability, and convergence order of the overall system. The authors in [13] use fuzzy-logic system-based step size control of P&O and InC algorithms and compare without the fuzzy-logic system and show that fuzzy-logic system-based control generates more energy extraction and significant speed enhancement compared to the classical MPPT algorithms. In reference [14], the authors implemented particle swarm optimization (PSO) based variable step size in order to reduce steady-state oscillations. The authors also mentioned that the implementation of PSO shows good performance even in partial shading conditions. In [15], the authors use an online-trained adaptive linear neuron (ADALINE) algorithm for maximum power point tracking from the photovoltaic module with indirect control mode. They also use a proportional-integral (PI) controller to increase the dynamic and transient performance of the overall system. The authors also compared their proposed methodology with conventional algorithms in terms of convergence speed and efficiency at fast and slow irradiances. In [16], the authors use an optimized modified sine-cosine MPPT algorithm with high convergence speed in grid application. Then, they compare their proposed algorithm with particle swarm optimization and artificial bee colony algorithms. The authors in [17] use an overall distribution-based MPPT algorithm in order to rapidly search for the maximum points. They also integrated particle swarm optimization into their proposed method for the enhancement of overall accuracy.

The rapid decline in the cost of photovoltaic (PV) cells and improvements in their efficiency is driving a massive increase in grid-connected and standalone PV systems [1, 18]. Many government policies have been put in place across various countries to encourage the installation of small-scale PV systems (especially rooftops) which also allows owners to sell their excess energy generation to the local power utility company thereby acting as a prosumer. The main challenge with the efficient and cost-effective installation of PV-plus-battery (PPB) systems is to optimally determine the number/size of PVs and batteries to be used in order to satisfy a particular amount of load or load profile. Since the capacity factor of PV systems is relatively low compared to traditional power generating systems (such as diesel generators) and its power generation is weather-dependent, combining it with energy storage systems such as batteries can help improve its capacity factor. The use of batteries allows for intelligent control and dispatch of power from the PV system. The cost of the PPB system and the variability in power generation from PVs make it imperative to accurately and optimally design the PPB system. Many commercial PPB system design software has been developed over the years. These programs are very expensive to use and usually not available to the general public/individual who might want to develop/design such systems. Also, these commercially available software are not flexible to use since the users have to control the source of the algorithms.

Several methods and optimization algorithms for PPB systems have been proposed in the literature. Authors of [19] proposed an optimal sizing algorithm for a solar-plus-storage (SPS) system to minimize the cost of the total electricity used during the lifetime of the SPS system. Also, a method of quantifying the resiliency provided by the SPS at a given location is also developed. The results show that the number of optimal PVs and batteries depends on the value attached to the re-

siliency. The optimal number of these components increases as the resiliency value increases.

An optimization algorithm to size a for PV-energy storage systems for islands is proposed in [20]. The proposed algorithm is developed to minimize the electricity generation cost by optimally selecting the rated power of the PV and the energy storage. Different technologies of PV and energy storage are also considered in the optimization. A method of optimally selecting PV and battery sizes for residential grid-connected PV-battery systems is proposed in [21]. The paper used yearlong time series data while applying a genetic algorithm to minimize the total electricity cost for the whole year. The proposed algorithm selects the optimal number of PVs and batteries by varying the batteries charging and discharging process based on the solar availability (irradiance) and the time-of-use cost of electricity. The results of the proposed algorithm show that co-optimizing the batteries and the PV sizes can reduce the amount of electricity used by the houses from the grid as well as the overall annual cost of electricity. The optimal batteries and PV sizes also strongly depend on the residential load profile as well as the cost of electricity and battery. The proposed algorithm can also be extended to aggregated PV and batteries of other residential households.

Authors of [22] also proposed an optimization algorithm for sizing grid-connected PV-plus-battery systems. The optimization algorithm allows users to define the probability that there will be a loss of load. The study considered both residential and commercial load profiles to achieve an optimal cost for the entire system. The effects of varying load curves and net metering tariffs are also considered under different grid-outage times.

Other methods of optimizing PV and battery designs that have been proposed in literature can be classified (according to [22]) as intuitive [23, 24], numerical [25], analytical [26, 27], Artificial intelligence [28] and hybrid [29]. The intuitive methods [23, 24] used simple PV and battery sizing calculations and considered averaged weather data (daily and monthly) which could cause over/underestimation of the PV/battery sizes. The numerical approach used in [25] proposed an energy balance algorithm based on time series data where the cost of the PV (consequently the size of the PV) is determined from cost-reliability data. The results of this technique could be sub-optimal since the size of the PV is changed linearly based on the energy balance between the generation and the load. The analytical methods used in [26, 27] are not flexible in the computation of the PV sizes while the AI-based [28, 30, 31] and hybrid [29] methods are very complex and are computationally expensive. Most of the papers discussed above used conventional MPPT algorithms such as P&O, Incremental Conductance MPPT, and other newly proposed algorithms such as straight line approximation-based MPPT, adaptive step size based MPPT algorithms for extracting maximum power from PV modules [4, 32, 33].

DC-DC converters are one of the most widely used power electronic converter typologies. They are used in applications such as switching-mode power supplies, solid-state transformers, resonant converters, smart inverters, maximum power point tracking charge controllers, and wireless power transfer. with increasing penetration of distributed energy resources (DERs) such as photovoltaic (PV) and battery energy storage systems, the demand for efficient and robust controllers for DC-DC converters is on the rise [34, 35]. DC-DC Buck converters are used for reducing (buck) the input voltage to the desired output voltages using a design control technique such as the Pulse Width Modulation (PWM) switching configuration. Getting the output voltage at the desired level is often complicated due to the input side

variation and load fluctuations [36]. In addition to these challenges, the converter parameters get aged over time. Therefore, a controller is required to regulate the output voltage despite the existing noisy environment. Due to its simplicity in design and control, Proportional Integral (PI) controllers are widely used in many industrial applications. Several methods for optimizing the controller parameters of DC-DC converters have been proposed in the literature. The authors in the [37] propose Neural Network Predictive Controller (NNPC) to reduce the output voltage deviations despite having input and load side fluctuations. They first trained the controller by the optimal parameters that helped the controller to know ahead of time what optimal parameters are required to generate whenever the fluctuations occur. In [38], the authors propose a Generalized State Space Averaging (GSSA) and AI method for designing the buck-converter controller parameters. They used the combination approach of PSO and Adaptive Tabu Search (ATS) methods for variations in both command input and load. In [39], the authors used Harmony Search Algorithm (HSA) as an optimizer for the controller which was able to stabilize the output voltage at desired DC level. They used a discrete time-based PI controller and different cost functions: Integral of Time-weighted Square Error (ITSE), Integral of Square Error, (ISE), and Integral of Absolute Error (IAE), for making the comparisons amongst the optimized control parameters. In [32, 40, 41], the authors used maximum power point tracking (MPPT) in order to extract maximum power from a Photovoltaic (PV) system where a PI controller was deployed in order to reduce the error between the MPPT controller and the PV operating point. They used a second controller for controlling the speed of the DC motor where the controlled voltage is fed to the DC motor, generated by the DC-DC converter. For both PI controllers, the authors used Artificial Bee Colony (ABC) algorithm in order to search for the controller parameters. Later they compared the performance of the

proposed ABC-based algorithm with the conventional genetic algorithm (GA) for different disturbances. The authors in [42] used online neural network-based control (OLNNC) scheme for a DC-DC buck-boost converter to improve the performance while the converter works in the transient mode, they also check the performance of their proposed system by varying the reference voltage and compared it with PI controller. In the research paper [43], the authors proposed a data-driven sigmoid-based PI controller in order to reduce the angular velocity errors of the DC motor governed by the DC-DC buck converter. They employed a Global Simultaneous Perturbation Stochastic Approximation (GSPSA) algorithm in order to find the PI controller parameters that helped in reducing the overall system errors. The authors in [44] proposed a self-learning Genetic Algorithm (GA) based fuzzy PI controller in order to minimize the output voltage variations for a closed loop DC-DC buck converter regardless of input-side and load-side fluctuations.

With the increase in deployment of DC sources such as battery energy storage systems, Electric vehicles (EVs), and PVs, significant improvement in power electronics converters technology, and increase use of DC loads, the development of DC microgrid is fast growing [1] [45]. The advantages of DC microgrids over their AC counterpart are the reduced amount of losses (due to reduced power conversion stages), lack of skin effect, no need for reactive power control, and reduced control complexity (only active power control is required) [46]. Consequently, it is envisaged that DC microgrids will be an integral part of the future smart grid technology [47].

The authors in [36] use a PV-battery-based charging strategy using anti-windup technology for the PI compensator that is used to drive the buck converter. They have shown the modeling of the DC-DC buck converter with the linear PV array model. Their simulation results have shown the different modes of operations with fewer undershoots and overshoots. In [48], the authors proposed a power manage-

ment scheme for a DC microgrid that is composed of a PV-Battery with different modes. They used DC bus voltage as an information carrier to differentiate between different modes. The authors in [49] proposed an adaptive battery control framework that learns the control parameters based on the model predictive controller (MPC) by adopting a neural network (NN) whenever data is available in the operating environment. They evaluate their control strategy using a PV-Battery-based system that shows optimal performance. The authors in [50] applied dc-bus signaling (DBS) as a distributed control strategy in order to control the converters that include voltage level changes to communicate with the other control nodes. They applied their proposed technique to a hybrid renewable system where the renewable sources supply the average load demand and the storage maintained the power balance to address the issue of the intermittent nature of the renewable sources. The authors in [51] utilize the sliding mode control technique in order to regulate the DC bus voltage for a standalone photovoltaic system.

In investigating the reliable operation of the microgrid, in [52] the authors had shown that an integral-based linear quadratic Gaussian controller can maintain the tracking of desired operation point under changing operating conditions like switching of supplying power from a PV, battery. The control topology was evaluated in an industrial area with a highly nonlinear impact on a local grid. In [53] the authors investigated on applying three different voltage scales to get new coordination for a tertiary control among the microgrid's central controllers. A recent work present in [54], has shown how Integral Sliding Mode Control (ISMC) scheme can bring total stability to each unit in a PV-based microgrid. The authors had shown that their proposed controller scheme could verify the active power flow and the voltage consistency of the DC bus within the standard limits. Low voltage DC grid is the point of interest in most of areas to facilitate the local demand and sudden

crisis. An adaptive droop control with sliding mode control can adjust the droop coefficient adaptively by utilizing a third loop in proportional integral control as present in [55] to minimize the current sharing errors and the bus voltage deviation. This also can reduce the communication burden, which seems interesting. In a similar approach but for reactive power sharing, the authors in [56] had proposed optimal secondary control with a non-iterative power flow-based algorithm, which can maintain reactive power sharing while regulating multiple load-bus voltages. In this work, modified Decoupled Linear power flow was used.

The development of DC microgrids is accelerating globally, with the incremental advent of DC sources such as battery energy storage systems, electric vehicles (EVs), and cheaper-efficient photovoltaic (PVs), and significant advancements in power electronics converter technology [1]. The increased percentage further demands this scenario of DC loads within a household and commercial consumers [45]. Some advantages of DC microgrids have made them uniquely favorable to their AC counterparts, such as more minor losses (due to fewer power conversion stages), no skin effect, no requirement for reactive power control, and lower control complexity (only active power control is required) [46]. As a result, DC microgrids are expected to be a key component of future smart grid, and electric power infrastructure [36].

The authors in [57] proposed a derivative-based controller to regulate the DC bus voltage by presenting a decentralized coordination control strategy for multiple PV modules. The authors also utilized the conventional V-I droop slope for PV participation in voltage regulation and power-sharing. Though the simulation and experimental validations showed promising results, finding the derivative is always challenging to accomplish, especially with a micro-controller. The authors in the research article [58] present an autonomous control scheme for DC micro-grid systems considering both grid-connected and islanding modes. The authors used

conventional droop control to regulate the bus voltage, using different controllers for different sources. The switching between controllers usually creates transients and voltage stress on the IGBTs, which is not analyzed in the paper. Finding the droop parameters are also critical for distributed energy resources (DERs) since the I-V curves are non-linear. In [59], the authors proposed a dynamic droop-based control mechanism for proper power-sharing of DERs. They have used communication for the control scheme, which could be ineffective if there is a communication failure.

The authors in [60] proposed a power management scheme using local converter controls by focusing on integrated operations of the controllers for the DC microgrid. They used low bandwidth communication to assist the control actions for making the system automated. The authors also validated their proposed control scheme by Hardware-in-the-loop (HIL) setup.

Inertia was always a vital subject in favor of the AC grid. In recent years, virtual inertia has been heavily investigated, with DC grid systems bringing similar characteristics to the AC grid. In such a research work [61], impedance was virtually increased in series with the DC-DC converter's inductor by a controller; ultimately, their technique was able to compensate for ripple magnitude or second-order ripple current. Moreover, researchers are also trying to bring some unification between AC and DC grids in the aspects of global usage. In work, [62], a solar converter, with its two terminals, is declared as universal usage with DC or AC (single phase to ground) sources. The authors had used to design a unified output filter while maintaining proper protection for AC or DC grid selection.

In the paper [63], the authors proposed a power management technique to address the voltage regulation issue using voltage ride-through capability. The authors investigated the active and reactive power flow along with the voltage profile in order

to maintain the stability of the network. The authors in [64] proposed an ANN-based controller to replace the conventional PI controllers and showed better performance; however, they used the conventional droop control for power-sharing and regulation, which falls into the identical drawback of minimum voltage regulation for high droop gain- that requires a secondary controller to regulate the bus voltage.

In conventional microgrids, PV systems typically operate at the Maximum Power Point (MPP) in order to maximize energy extraction irrespective of their capability to participate in system frequency regulation (FR). In view of FR, several studies have investigated the use of Battery Energy Storage Systems (BESS) to provide Virtual Inertia (VI). However, high maintenance costs and expensive recycling, combined with the impact of high-current ramping on the longevity of BESSs make the development of alternative FR methods increasingly important. Since the use of PV systems is becoming ubiquitous in microgrids, and thus inducing a reduction in available sources of rotational inertia, it is crucial to design control mechanisms for PV systems to intelligently participate in FR within microgrid systems. [65–68].

Several studies have been carried out to address the use of PV systems for frequency regulation. The authors in [69] use a fuzzy-based frequency control method for injecting PV power whenever required in a PV-Diesel hybrid system. The fuzzy output command has three inputs: frequency deviation, average insolation, and change of insolation. They have shown their proposed framework provides better performance than the conventional energy storage system (ESS) based method.

In [70], the authors use Virtual Synchronous Generator (VSG) based PV generation control to provide frequency regulation. Their proposed algorithm generates PV voltage deviation and modified pre-defined power versus voltage curve to provide primary frequency support. The authors in [71] proposed a decentralized-based frequency regulation technique using droop control where each PV unit uses its own

droop slope to provide the required frequency support. In [72], the authors used PSO optimization to have optimal control parameters for the PI-based grid-forming inverter control during islanding operation. They demonstrated that the optimal control parameters provide good transient responses during variations in power and frequency. In [73], the authors proposed VI-based frequency control by utilizing the dynamics of DC-link capacitor voltage for an islanded microgrid. They used local measurements without using an extra phase locked loop to enhance the reliability of the overall system. In [74], the authors proposed a methodology to provide FR that consists of two layers: the power reserve control (PRC) layer and the FR layer. In the PRC layer, they proposed a power tracking control method based on a curtailment power curve whereas in the FR layer, they used a combination of droop and VI to adjust the given power reserve ratio. In reference [75], the authors developed a mathematical model 'rapid active power control (RAPC)' to provide frequency support to the grid. They coupled the RAPC with a maximum power estimation method which is also mathematical. The RAPC method they used, utilized a look-up table which contains interpolated data from the PV array.

In conventional microgrids, PV systems are normally intended to operate at the Maximum Power Point (MPP) just to maximize energy extraction irrespective of its capability to participate in the system Frequency Regulation (FR) process. In view of FR, several studies have investigated Battery Energy Storage Systems (BESS) only or combined PV+BESS systems to provide the required Virtual Inertia (VI). However, the introduction of a BESS increases the system cost significantly and the larger the size of a battery, the higher the cost will be. Moreover, if the battery is not properly controlled, the frequent charging-discharging cycles of the battery could potentially lessen the longevity of the very expensive device. Therefore, it is highly important to design the control mechanism of Distributed Energy Resource

(DER) based microgrid systems intelligently to allow PV to participate in FR as the primary source for the best utilization of the PV power, where the battery would act as the secondary source when PV is no longer capable of providing the required FR [65–68].

Several studies have been conducted to address this issue of FR. In [70], the authors use a Virtual Synchronous Generator (VSG) based PV generation control to provide FR. Their proposed algorithm generates the PV voltage deviation and a modified pre-defined P-V curve to provide primary frequency support. The authors in [71] proposed a decentralized frequency regulation technique using droop control where each PV unit uses its own droop slope to provide the required frequency support. In [73], the authors proposed VI-based frequency control by utilizing the dynamics of the DC-link capacitor voltage for an islanded microgrid. They used local measurements without using an extra phase locked loop to enhance the reliability of the overall system. In [74], the authors proposed a methodology to provide FR that consists of two layers: A Power Reserve Control (PRC) layer and an FR layer. In the PRC layer, they proposed a power tracking control method based on curtailment of the P-V curve whereas in the FR layer, they used a combination of droop and VI to adjust the given power reserve ratio. According to [76], if the battery state of charge (SOC) is regulated by power offset signals determined by a PV forecast and projections of the energy needed to run FR, the planned engagement of DERs can provide a number of benefits. As reported in [77], the stability of microgrid frequency seems well regulated with lower droop gains of smart loads in cases of varying PV generation. In [78], a fuzzy control scheme is investigated in its supervisory role to regulate a battery's power flow in maintaining the energy balance, hence ensuring fast frequency recovery. This immediate response to frequency change and supply energy balance led to microgrid resiliency. In the case of communicative DERs inside

a microgrid, the authors in [79] proposed a fixed-time observer to get the typical battery State Of Charge (SOC) using only data from nearby batteries towards the SOC balancing. In [75], the authors developed a mathematical model 'Rapid Active Power Control (RAPC)' to provide frequency support to the grid. They coupled the RAPC with a maximum power estimation method which is also mathematical. The RAPC method they used utilized a look-up table that contains interpolated data from the PV array.

There has been a massive global increase in the implementation of microgrids due to their ability to disconnect from the main grid and operate autonomously. The significant advancements in power electronic converter technology [1], the steady decrease in cost, and improved efficiency of renewable energy resources such as Photovoltaic (PVs) have contributed to an increase in microgrid designs and deployments. Microgrids can improve the resilience of the main grid and also facilitate quick recovery during extreme events. However, with the increasing number of inverter-based resources, the reduction of inertia is also becoming a concern due to its possible impact on the stability of the grid. To address this, battery energy storage systems (BESS) have been used traditionally to improve the dispatch ability of the microgrid and also to provide frequency regulation-based ancillary services in both grid-connected and islanded scenarios [80]. The cost of BESS is one of the main constraints in their mass deployments. This has led to investigating the possibility of using PV systems for frequency regulation services, overall system costs to be reduced and even allowing for greater flexibility. Also, since inverters require a stable DC-link voltage to inject AC current, PVs can be used to provide stable DC consequently providing a well-regulated AC output voltage. In [81], the authors demonstrate the correlation between irradiance and harmonics while DC-bus was controlled by a grid-following inverter control technique. The authors show that

THD is higher usually in the morning and evening. The authors in [57] proposed a derivative-based controller to regulate the DC bus voltage by presenting a decentralized coordination control strategy for multiple PV modules. The authors also utilized the conventional V-I droop slope for PV participation in voltage regulation and power-sharing. Though the simulation and experimental validations showed promising results, finding the derivative is challenging to accomplish. The authors in the research article [58] present an autonomous control scheme for DC micro-grid systems considering both grid-connected and islanded modes. The authors used conventional droop control to regulate the bus voltage, using different controllers for different sources. However, switching between controllers may create transients and voltage stress on the IGBTs, which is not analyzed in the paper. Finding the droop parameters are also critical for Distributed Energy Resources (DERs) since the I-V curves are non-linear. In [59], the authors proposed a dynamic droop-based control mechanism for proper power-sharing of DERs. They have used communication for the control scheme, which could cause failure if there is a communication breakdown. Inertia was always a vital subject in ensuring the stability of the electrical grid. In recent years, virtual inertia has been heavily investigated, with DC grid systems bringing similar characteristics to AC counterparts. As such in [61], impedance was virtually increased in series with the DC-DC converter's inductor using a controller. Moreover, researchers are also trying to bring some unification between AC and DC grids in the aspects of global usage.

The authors in [60] proposed a power management scheme using local converter controls focusing on integrated operations of the controllers for a DC microgrid. They utilize low bandwidth communication to assist the control actions for making the system automated. The authors also validated their proposed control scheme with a Hardware-in-The-Loop (HIL) simulation setup. A power management tech-

nique is proposed in [63] to address the voltage regulation issue using voltage ride-through capability. The authors investigated active and reactive power flow along with the voltage profile in order to maintain the stability of the network. The authors in [64] proposed an ANN-based controller to replace conventional PI controllers, which achieved better performance; however, they used conventional droop control for power-sharing and regulation, which has the identical drawback of minimum voltage regulation for high droop gain. Thus requiring a secondary controller to regulate the bus voltage. The aforementioned papers and many others in the literature did not develop a control strategy that allows the operating point of PV to be in order to effectively regulate the microgrid's DC bus voltage depending on the dynamics of the AC voltage and frequency. The authors in [82] used an adaptive discrete PID controller to regulate the inverter voltage control for PV and battery energy source-based microgrid where PV was working in MPP tracking mode always. In their control algorithm, the battery was solely responsible for DC-Bus voltage regulation since PV is being used as a current-controlled source. Their controlled strategy has the potential of stressing the battery when it is fully charged which might be an issue for battery longevity.

1.2 Research Objectives and Contributions

1. **Step-size Optimization of New Straight Line approximation-based MPPT Algorithm for Photovoltaic Systems**

   In this objective, a straight-line approximation-based maximum power point tracking (MPPT) algorithm using open circuit voltage of a Photovoltaic (PV) module is proposed and then employs an iterative-based optimization technique for determining the optimum step-size to extract maximum energy from

the PV module. The proposed algorithm is compared with the conventional P&O method in terms of maximum energy extraction at different step sizes.

The main contributions are as follows: i) The results obtained show that the proposed algorithm extracts more energy at optimized step size and at other different step sizes during fast and slow varying global horizontal irradiance (GHI) parameters.

ii) The simulation results also show that the proposed method is much faster than the conventional P&O algorithm in finding the MPP for the same step size. The fast-finding maximum power point (MPP) by the proposed algorithm not only allows for increasing the overall system efficiency but also helps by extracting more energy from PV module, especially for rapidly changing weather parameters

2. **A Binary Search Algorithm based Optimal Sizing of Photovoltaic and Energy Storage Systems**

   The use of PVs and storage systems behind the meter provides a backup power supply to owners as well as capable of providing ancillary services to the power grid such as peak load shifting, demand response, and energy arbitrage amongst others. This paper proposes a binary-search-based optimization algorithm determines the size of the photovoltaic (PV) plus battery standalone system in order to meet a defined load profile. The objective function formulation minimizes the overall system cost and makes sure that the total load rejection is zero by the PV-plus-battery (PPB) system for the load profile considered throughout the year. The optimization variable set in the proposed formulation are the number of the PVs and the batteries. The battery state-of-charge, the number of PVs, and the batteries are set as the optimization

constraints. The proposed algorithm is fed with a year-long actual irradiance and load profile data for the facility located in Miami FL. The cost factors for the PV and battery are also input to the proposed algorithm. The results show that the proposed algorithm can achieve a zero load deficit for the period and the load profile considered.

The main contributions of this research are as follows: i) The proposed algorithm is less computationally intensive compared to the AI-based methods since it uses the the middle value of a sorted array of variables and compares it with the target values that achieve the minimum objective functions of the total load rejection and the cost of installation of the PPB system.

ii) Another contribution is the possibility to ensure a zero load rejection by the PPB system with minimal cost of installation.

3. **Particle Swarm Optimization-based PID Controller Design for DC-DC Buck Converter**

   The performance of PID controllers depends on the appropriate choice of control parameters. These parameters are chosen in order to achieve reduced transient effects such as overshoot/undershoot settling time and steady-state errors. This objective presents a particle swarm optimization (PSO) based PID controller design for the optimal selection of the buck converter-control PID parameters: proportional (Kp), integral (Ki), and derivative (Kd). In order to address the wind-up issue with PI controllers, this objective proposes the use of an anti-windup control technique with a view to achieving very good voltage regulation in the output despite a wide range of input voltage and load variation. The performance of the proposed controller design is verified using MATLAB/Simulink.

The main contribution is stated as follows: The results demonstrate the ability of the optimization algorithm in reducing the aforementioned transient and steady-state errors, thereby, reducing the output voltage fluctuations despite input and load side fluctuations.

4. **Voltage Regulation and Battery Stress-reduction Strategy for DC Microgrid**

   A control strategy for Photovoltaic (PV) systems and energy storage systems (ESS) in an islanded DC microgrid is proposed.

   The major contributions are as follows: i) In contrast to conventional control techniques where the battery is mostly responsible for DC grid voltage regulation, the proposed strategy utilizes PV based controller separately in regulating the microgrid voltage when the battery is fully charged and disconnected, consequently reducing the overcharging stress on the battery, thereby prolonging the battery life.

   ii) Another point worth mentioning here is that the DC bus works as the sole information carrier for the entire system which curtails the extra addition of sensors in the system. The simulation results show the efficacy of the proposed controller in regulating the DC bus voltage despite varying irradiance conditions and varying load conditions.

5. **A Unified Controller for Hybrid PV-Battery system with DC Microgrid Voltage Regulation in Grid-connected and Islanding-mode**

   It is desirable that photovoltaic (PV) arrays provide maximum power during the grid-connected mode since when the bulk grid is present, PV can be controlled as a current source for injecting maximum power (MP) by using a maximum power point (MPP) tracker. During the grid-connected mode, the

bulk the grid itself can regulate the DC-bus voltage; however, when the bulk grid is not present, then the hybrid PV-Battery system has to generate the reference by itself, depending on the load power and the power-curtailment most likely would be necessary for voltage regulation at the DC-bus. Because if the PV still provides maximum power when PV power is higher than the load power during the islanding mode, the DC-bus voltage would swell - that might create voltage instability in the system. In order to address this issue, a unified controller which combines the control action of maximum power injection at grid-connected or battery-connected mode and voltage regulation at islanding mode by a single reference voltage generation is proposed. The proposed controller's performance is then verified by varying the load side resistance and also dynamic irradiance. The simulation results conducted in MATLAB/Simulink environment show promising results.

The significant contributions of this research article are as follows: i) Participation of photovoltaic arrays in regulating the DCbus voltage by the proposed unified controller ii) Reduction of sensors, i.e., there is no requirement of current-sensors since dc-bus voltage acts as an information carrier for the control-actions ii) Seamless transition between maximum power point mode during the grid-connected or battery-connected scenario and voltage regulation mode during an islanding scenario by a single reference control signal.

6. **ANN-based Dynamic Frequency Regulation of PV-based Hybrid Microgrid system**

The high penetration of inverter-based renewable energy resources, such as Photovoltaic (PV) systems in modern power systems often leads to reduced system inertia which makes efficient frequency control highly imperative. This

research develops a novel method of frequency regulation using PV system. The proposed method uses the conventional swing equation to generate the needed virtual inertia (VI) based on the frequency dynamics of the system and then feeds an already-trained Artificial Neural Network (ANN) to determine the corresponding operating point for the PV. A proportional-integral (PI) controller is then used to drive the operating point of PV towards the ANN-generated voltage reference. The shifting of the operating point to the desired voltage value will adjust the active power injection from PV in order to provide the desired frequency regulation. Simulation results show that the proposed control mechanism provides high accuracy, and a fast-tracking speed, and has the potential to significantly improve stability during frequency disturbance in PV-based power systems.

The main contributions of this work are as follows:

i) A VI-ANN control mechanism that emulates the behavior of a synchronous generator (SG) to provide primary frequency support with much faster dynamics to keep the frequency nadir within the desired limits. ii) Simplifying the overall control strategy by implementing the algorithm on the DC-DC converter rather than on the inverter side - allowing the inverter to only regulate DC-bus voltage and carry out reactive power control

7. **Dynamic Frequency Regulation based on Hierarchical Control of DERs in Microgrid**

   A dynamic frequency regulation technique and control which prioritizes the use of PV as the primary control and battery as the secondary control is proposed. When the frequency of the islanded microgrid varies, the frequency deviation is used to determine the operating point of the PV on the P-V

curve. The predefined PV's operating region is set, and the battery control kicks in (to either charge or discharge the battery) whenever the required active power needed for frequency regulation would drag the PV's operating point outside this region. In order to execute the proposed hierarchical control strategy, two novel local controllers are developed for both the PV and battery systems. The effectiveness of the control strategy and the local controllers are validated in MATLAB/Simulink and a real-time simulation platform. The proposed control architecture helps to reduce the number of battery charging and discharging cycles, consequently increasing its longevity as well as reducing the system's overall cost.

The main contributions of this work are summarized as follows:

i) A PV-side frequency-to-voltage reference generation controller that doesn't use a Virtual Inertia (VI) based power reference generator. This simpler design process makes the system resistant to noise amplification which may be caused by the derivative component of VI. ii) A battery-side current reference generation controller to maximize PV generation and utilize the battery as a secondary source of frequency regulation. This reduces the necessary battery size and therefore decreases the overall system cost. This also lessens the current throughput of the battery, potentially increasing battery life.

8. **A Unified Control Strategy for Voltage Regulation in a Microgrid System**

   A PV system can be operated either as a current-controlled source (at the maximum power extraction point) or a voltage-controlled source. This typically requires two independent controllers. This work proposes a unified maximum power extraction control and voltage control strategy which is load adaptive.

A trained Artificial Neural Network (ANN) is used to determine the Maximum Power Point (MPP) of the PV system. The proposed control strategy dynamically shifts the PV operating point along the right-side region of the P vs. V curve with respect to the MPP which enables it to operate instead as a voltage-controlled source. The controller is connected to an inverter through a DC-DC buck converter which regulates the DC bus voltage at the desired operating point. The inverter uses a v-f control strategy to regulate the AC side voltage at the desired reference value regardless of changes in load. The effectiveness of the proposed control strategy is verified in MATLAB/Simulink and a real-time simulator-based hardware platform.

The main contributions of this work include:

i) The use of PV in regulating DC-bus voltage by the proposed unified controller regardless of load and irradiance variations. When the load requires more power, the proposed controller shifts the PV operating point towards, and up to, the MPP. When the load is less than the PV power output, the proposed controller shifts the operating point towards the right, away from the MPP point, to make the overall system stable. ii) The proposed control strategy requires fewer sensors compared to existing methods in literature because there is no requirement for current or power sensors for load measurement. The DC bus voltage measurement is used to sense load changes and to determine the appropriate control actions and set points. iii) Since the proposed controller utilizes PV to behave as a voltage-controlled source, it doesn't require extra constant voltage source devices, such as battery storage, consequently minimizing the overall system cost significantly

1.2.1 Dissertation Organization

The dissertation is organized as follows: Chapter 2 describes the development of fast MPPT algorithm for rapid changing weather conditions; Chapter 3 depicts an offline Optimization algorithm to determine the optimal number of PVs and Battery Energy Sources; Chapter 4 illustrates how to optimally design the control parameters of converter in order to reduce the transients while variations in both input and output-side; Chapter 5 depicts how a PV-side controller can address the voltage regulation issues alone without taking assistance from the Battery; Chapter 6 describes how the MPPT operation and voltage regulation operation can be combined as a single control signal with the help of ANN based voltage estimator; Chapter 7 shows how PV can participate in frequency regulation in microgrid with the help of VI-ANN based control system; Chapter 8 illustrates how PV can participate in restoring frequency of the system as a primary controller and Battery as a secondary controller; Chapter 9 illustrates how PV solely can regulate the bus voltage of AC-DC microgrid by unifying the MPPT and voltage regulation operation and Chapter 10 summarizes all the chapters of the dissertation with future directions for further exploration.

CHAPTER 2

STEP-SIZE OPTIMIZATION OF NEW STRAIGHT LINE APPROXIMATION-BASED MPPT ALGORITHM FOR PHOTOVOLTAIC SYSTEMS

This chapter is devoted to developing a fast maximum power point tracking (MPPT) algorithm for rapidly changing weather conditions. The developed algorithm reaches a maximum power point (MPP) using the intersection of two straight lines while irradiance is dynamically changing- making it faster compared to state-of-the-art MPPT algorithms. The algorithm also uses optimum step size to acquire the maximum amount of energy from PV modules with higher efficiency.

2.1 Proposed MPPT Algorithm

The conventional $P\&O$ algorithm starts with the initial point defined by the initial assignment of the duty cycle on the P-V curve. Based on this initial point, it gradually gets closer to the MPP using a fixed step size. If the step size is smaller it takes a longer time in reaching MPP while a larger step size helps the algorithm reach at MPP faster, however, it generates a lot of power losses because of the oscillations around the MPP. Fig. 5.3 shows the conceptual framework of the conventional P&O algorithm. If the initial point is lying on the left-hand side of MPP and after perturbation, the operating point goes further away from the MPP as illustrated in the figure by (i), then ΔP and ΔV are both negative; the algorithm will start going towards the right side. The same case would happen for (ii). Therefore, if the sign of ΔP and ΔV are either both positive or both negative, the algorithm will perturb towards the right side to reach MPP. However, if the sign of ΔP and ΔV are opposite, then the algorithm starts moving towards the left direction as shown

in the Fig. 5.3 by region (iii) and (iv) [83].

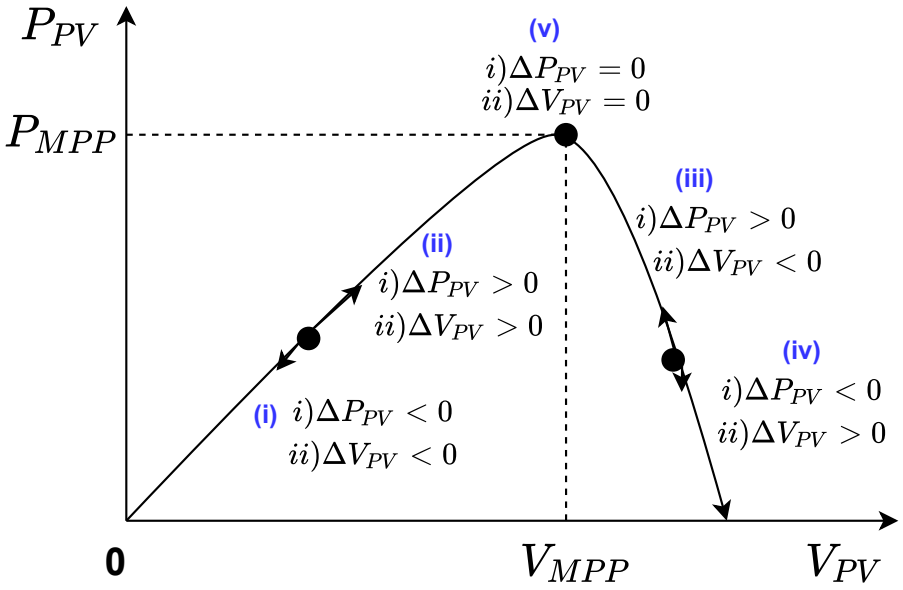

Figure 2.1: Concept behind P&O MPPT algorithm

In contrast, the proposed algorithm is initialized with 4 points on P-V curve, 2 on the left side of MPP: $(0,0),(0.1\times V_{oc}, P(0.1\times V_{oc}))$, other 2 on the right side of MPP: $(V_{oc},0),(0.9\times V_{oc}, P(0.9\times V_{oc}))$ as shown in Fig.2.2 - denoted by P_1, P_2, P_3, P_4 on the C_1 curve. These 4 points can be found in the PV module specifications.

The 10% and 90% of V_{OC} points have been found by studying different PV modules from low irradiance to high irradiance. The algorithm then draws 2 straights lines based on the 4 points, the intersection point - V_i^1 on curve C_1 and V_i^2 on curve C_2 of the 2 straight lines produce the starting point for the algorithm which is always very close to the MPP for low to higher GHI as shown in Fig. 2.2.

Afterward, the algorithm takes a few steps to reach MPP. The advantages of calculating the intersection point at first are in two folds: i) It takes less time to reach MPP, ii) a small step size can be chosen after getting the intersection point,

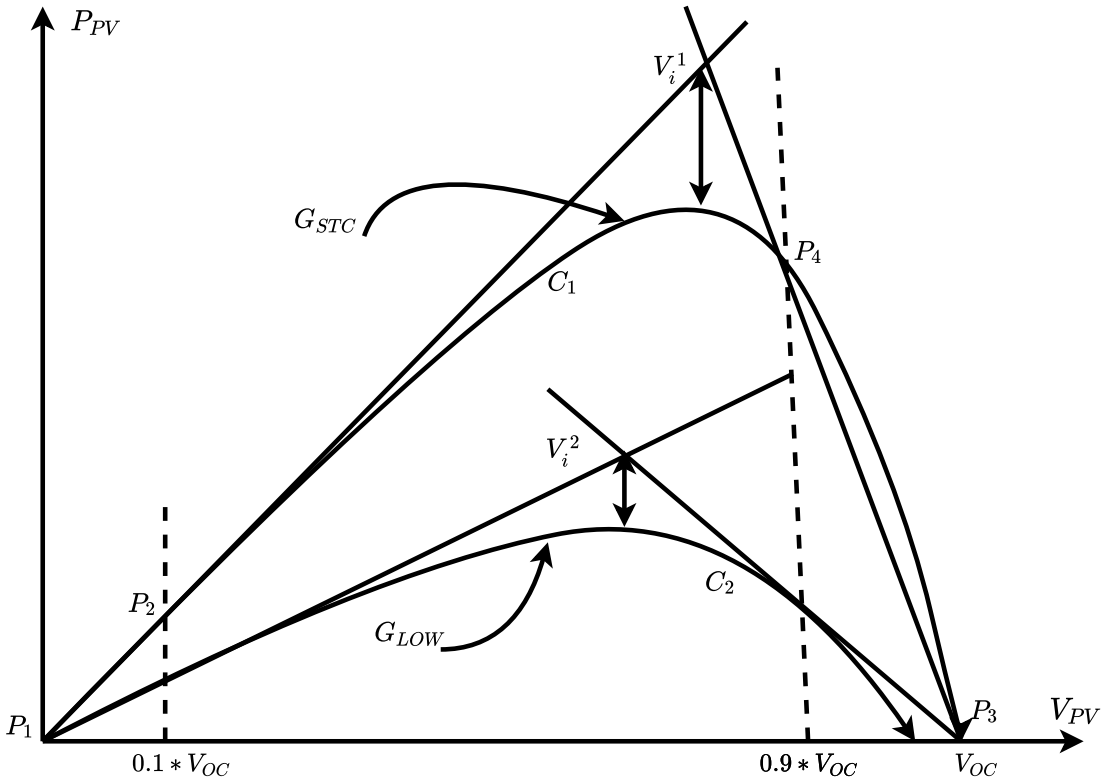

Figure 2.2: Conceptual figure of the proposed algorithm

hence, reducing the power loss around the MPP. This increases the total energy generation and efficiency of the entire PV system.

Fig. 2.3 shows the dynamic irradiance curve over a period of time and the corresponding maximum power over time at those irradiances. The sampling time for two consecutive irradiance data is δt, while Δt is the time the MPPT algorithm would take to calculate the MPP for that irradiance. Therefore, if δt is greater than Δt, then the algorithm can successfully find the MPP, however, if δt is smaller than Δt, then the algorithm will fail in finding the MPP point because it means the change in irradiance is faster than finding the MPP by the algorithm. This condition potentially could occur in the case of the P&O algorithm whenever the step size is smaller. In that case, δt could be smaller than Δt which might lead the algorithm going in the wrong direction. In contrast, the proposed algorithm does

not approach the MPP point using the step size in the beginning, rather it calculates the intersection point which is generally very close to the MPP. Therefore, for the proposed algorithm, potentially Δt would be smaller than δt which makes it suitable even for rapidly varying weather conditions.

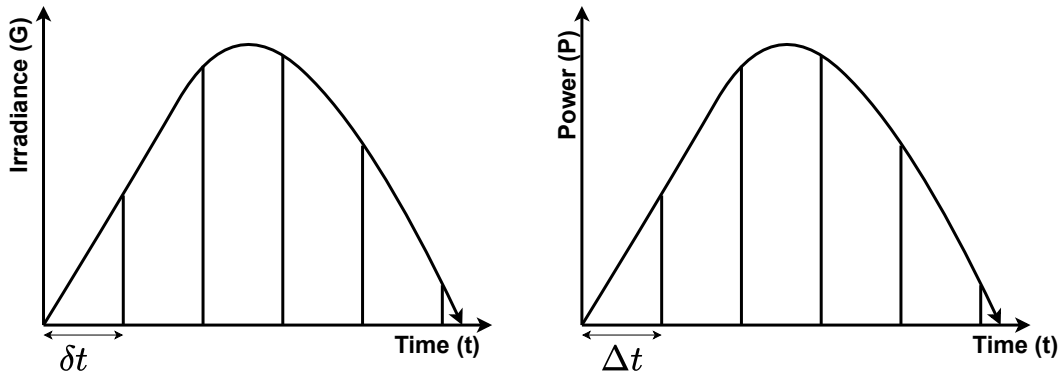

Figure 2.3: Condition for the correct finding of MPP

The proposed MPP algorithm is as presented in Algorithms 1 and 2. Based on the proposed algorithms, an iteration based optimization algorithm is carried out to determine the optimal step size. The flowchart is as shown in Fig.2.4.

A small search space of discrete step size is provided for the algorithm to find out the optimal step size that would generate maximum energy for fast and slow varying GHI.

2.2 Simulation Results and Discussion

The circuit diagram of the photovoltaic system is designed and simulated in the MATLAB/Simulink environment and the block diagram of the system design is shown in Fig. 2.5. A DC-DC boost converter is used for the duty cycle variation in achieving desired MPP. A PI controller is used to minimize the error between the calculated MPP by the proposed algorithm and the operating point of the PV

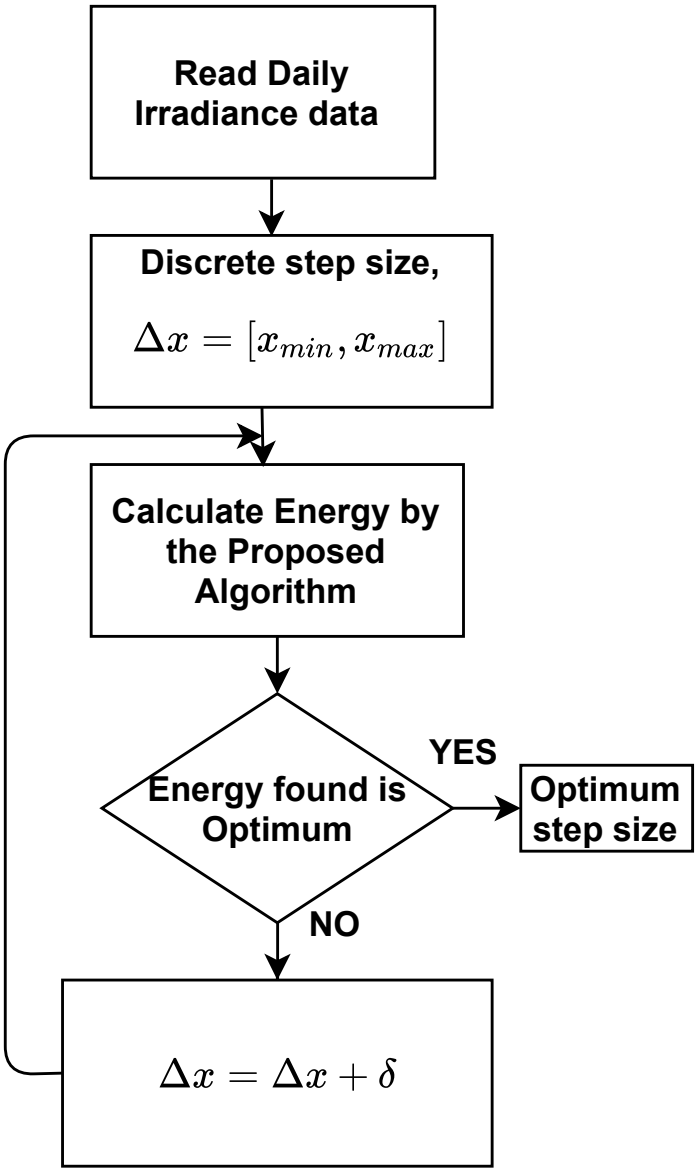

Figure 2.4: Flowchart of Optimization Algorithm

module. The control signal from the PI controller is then compared with a saw-tooth waveform to generate the desired duty cycle.

For the modeling of the PV module in MATLAB/Simulink, Table 2.1 PV-characteristics is used where the maximum power is $150W$ at standard temperature and irradiance conditions. For the modeling in Simulink/Matlab environment, the BP Solar BP SX 150S PV module is chosen.

Algorithm 1 Algorithm for finding the intersection between 2 straight lines

Input: $irradiance, temperature, V_{oc}$
Output: V_r

$V_{left} = 0.1 \times V_{oc}$
$I_{left} = PV(V_{left}, G, TaC)$
$P_{left} = V_{left} \times I_{left}$
$x_1 = [0, V_{left}]$
$y_1 = [0, P_{left}]$
$p_1 = polyfit(x_1, y_1, 1)$
$V_{right} = 0.9 \times V_{oc}$
$I_{right} = PV(V_{right}, G, TaC)$
$P_{right} = V_{right} \times I_{right}$
$x_2 = [0, V_{right}]$
$y_2 = [0, P_{right}]$
$p_2 = polyfit(x_2, y_2, 1)$
$x_{intersection} = fzero(@(x))polyval(p_1 - p_2, x), 5)$
$V_r = x_{intersection}$
return V_r

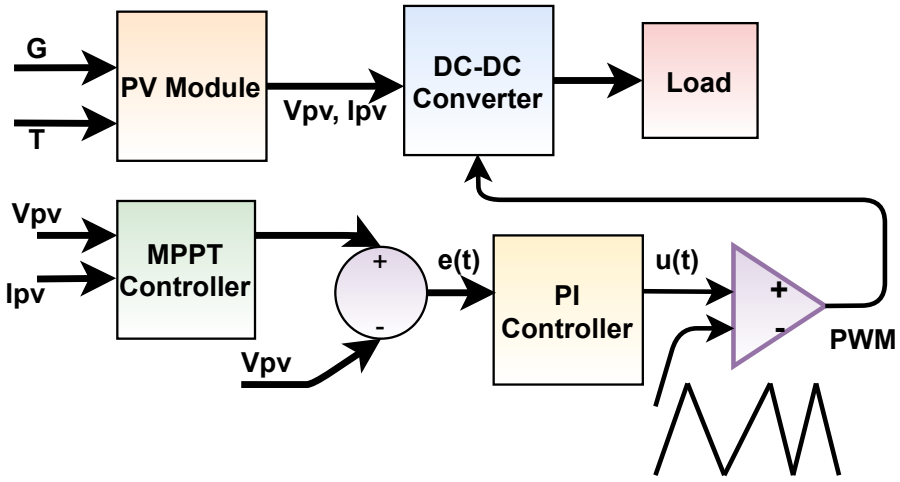

Figure 2.5: Block diagram of the system design in Simulink

The PV module provides 150 W of nominal maximum power. Table 2.1 shows the electrical parameters of the PV module used:

Fig. 2.6 illustrates the power vs voltage curves at different irradiance values for the chosen PV module. The irradiances are varied from $50W/m^2$ to $1000W/m^2$ at $50W/m^2$ step and the theoretical maximum power points are shown using red

Algorithm 2 Reaching at MPP from the intersection point

Input: $P_{old}, P_{new}, V_{old}, V_{new}$
Output: V_{ref}

Initialisation :
$V_{oc} = V$
$delV = \delta$
$V_r = callAlgorithm2$
$V_{ref} = V_r$
if $P_{new} > P_{old}$ **then**
  if $V_{new} > V_{old}$ **then**
    $V_{ref} = V_{ref} + delV$
  else
    $V_{ref} = V_{ref} - delV$
  end if
else
  if $V_{new} > V_{old}$ **then**
    $V_{ref} = V_{ref} - delV$
  else
    $V_{ref} = V_{ref} + delV$
  end if
end if
if $V_{ref} > V_{oc}$ **then**
  $V_{ref} = V_r$
else if $V_{ref} <= 0$ **then**
  $V_{ref} = V_r$
end if
return V_{ref}

Table 2.1: PV module design specifications

Maximum Power (P_{MAX})	150 W
Voltage at P_{MAX}(V_{MP})	34.5 V
Current at P_{MAX}(I_{MP})	4.35 A
Open Circuit Voltage (V_{OC})	43.5 V
Short Circuit Current (I_{SC})	4.75 A

asterisk on every irradiance curve.

The time it takes the proposed algorithm to reach MPP is compared with the standard P&O algorithm. A GHI of 900 W/m^2 is used and temperature 25^0C is chosen for the simulation. For a fair comparison, the same step size 0.001 is used for

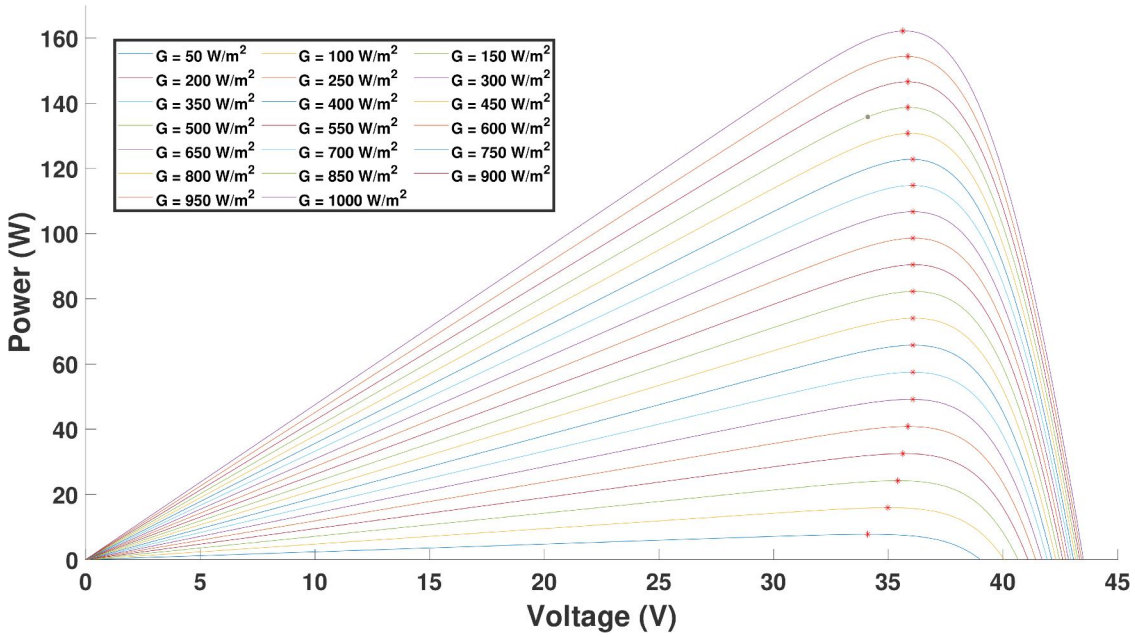

Figure 2.6: Power vs Voltage curves at difference irradiances with corresponding MPP

both the P & O and the proposed algorithm. As we can see from Fig. 2.7, the P&O takes about 0.35 seconds reaching at MPP whereas the proposed algorithm takes only about 0.02 seconds reaching at MPP. The fluctuations of the P&O algorithm could have been reduced by choosing an even smaller step size. However, that could make the algorithm even slower in reaching MPP, therefore, not making it suitable especially for rapidly changing weather parameters.

In order to test the performance of the proposed algorithm, real time dynamic irradiance data is used which is shown in Fig. 2.8. From this one year irradiance data, one clear day (slow irradiance change) and one cloudy day (rapid irradiance change) is chosen for the interpretation of the performance and comparison between the proposed and P&O algorithm. The clear day and cloudy day irradiance data are shown in Fig. 2.9 and Fig. 2.10 respectively.

The comparison between the proposed algorithm and the P&O algorithm is conducted using different step sizes for the above-mentioned clear and cloudy days.

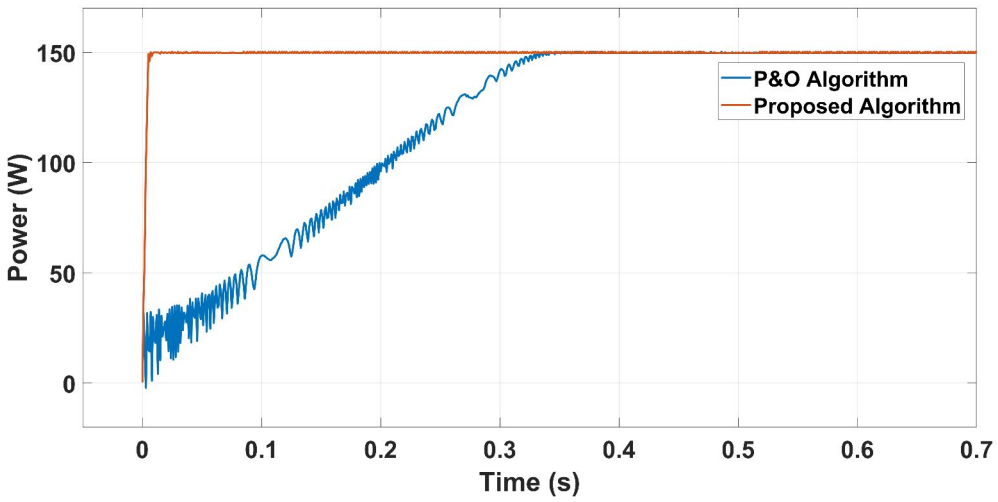

Figure 2.7: Time difference in finding MPP between P&O and Proposed Algorithm

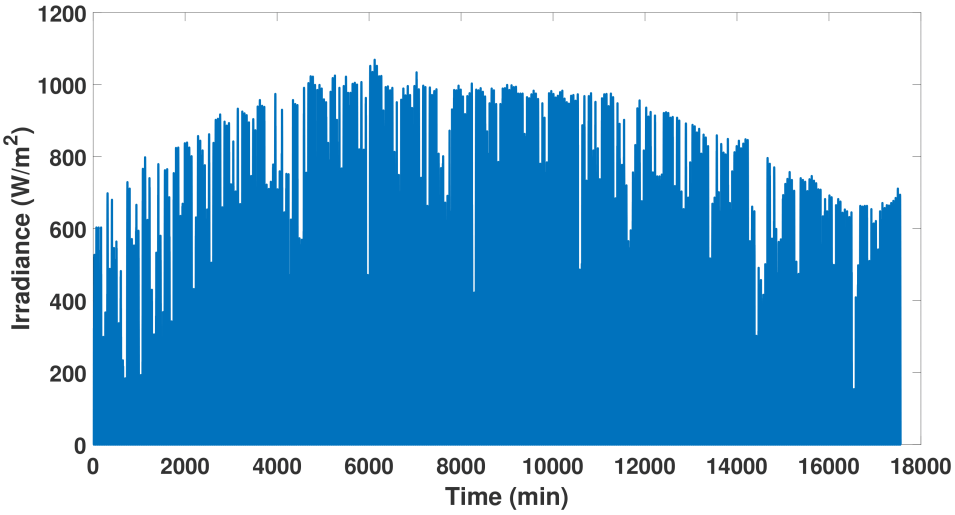

Figure 2.8: One-year irradiance data

Three different step sizes are used for both clear and cloudy days: 0.0001, 0.0005, and 0.003. The results are shown from Fig. 2.11 to Fig. 2.16. As we can see in Fig. 2.11, the proposed algorithm is able to extract the maximum power for dynamic irradiance even with the smallest step size of 0.0001. The performance of the P&O at this step size is worst since the dynamics of the P&O algorithm solely depend on the step size, the small step makes the algorithm very slow because of a large number of iterations it has to take in reaching at maximum power points,

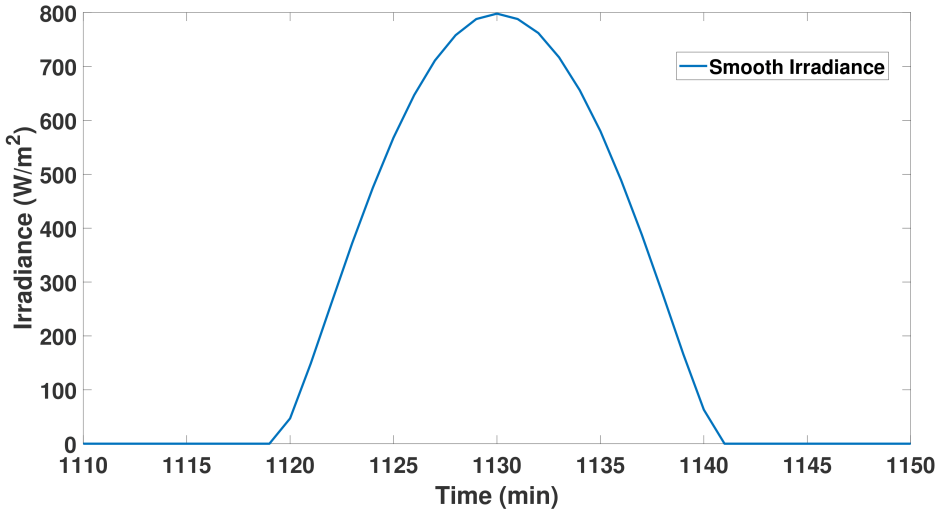

Figure 2.9: Clear Day Irradiance Data

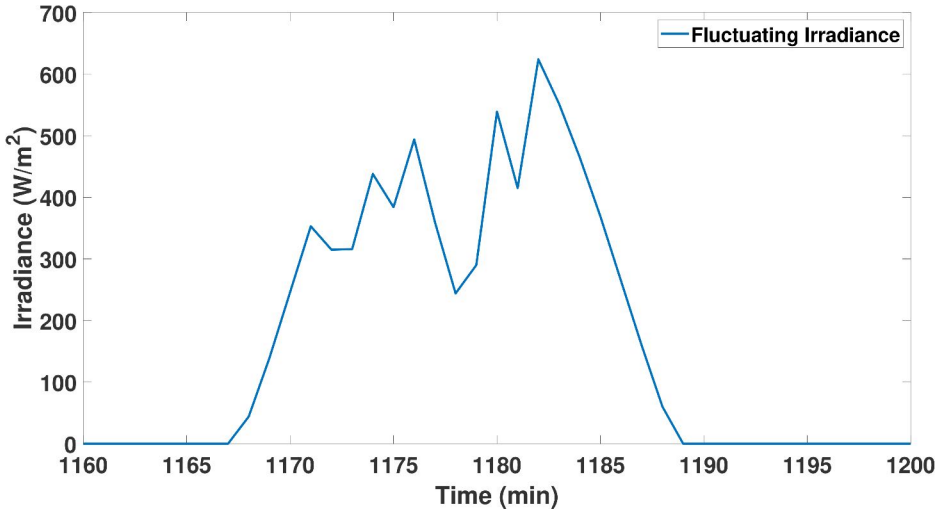

Figure 2.10: Cloudy Day Irradiance Data

consequently, not able to keep track of the dynamic irradiance changes, resulting in poor performance. The result is even worse for cloudy days as shown in Fig. 2.14 when the irradiance changes very fast. Though the P&O algorithm starts showing better performance while the step size increases, however, the oscillating behavior of the algorithm around the MPP will also grow proportional to the step-size increment which would cause energy loss.

This trade-off has been taken care of by the proposed algorithm that performs very well with this small step size because of its initial calculation of intersection

points using two straight lines. Since the intersection point generally lies in close proximity to the maximum power point, the algorithm would take less number of iterations in reaching the maximum power points from the intersection point.

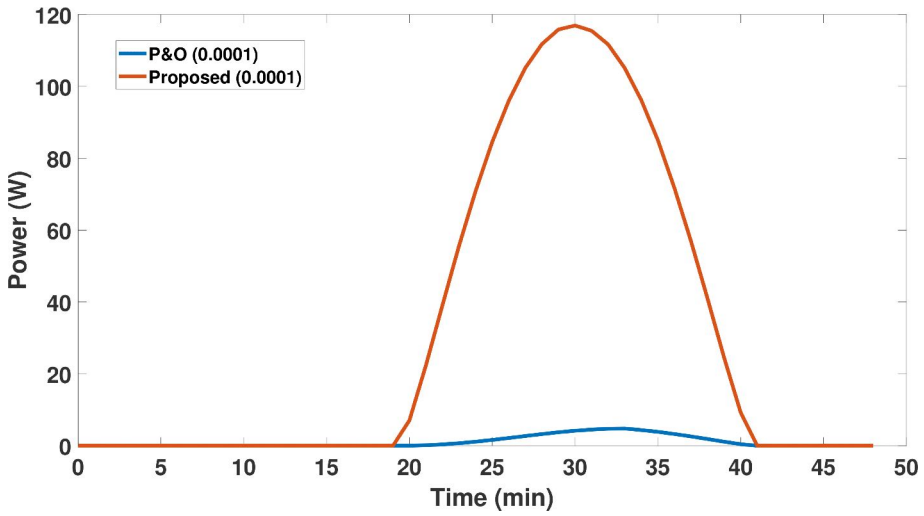

Figure 2.11: Comparison between proposed and P&O algorithm at the step size of 0.0001 for a sunny day

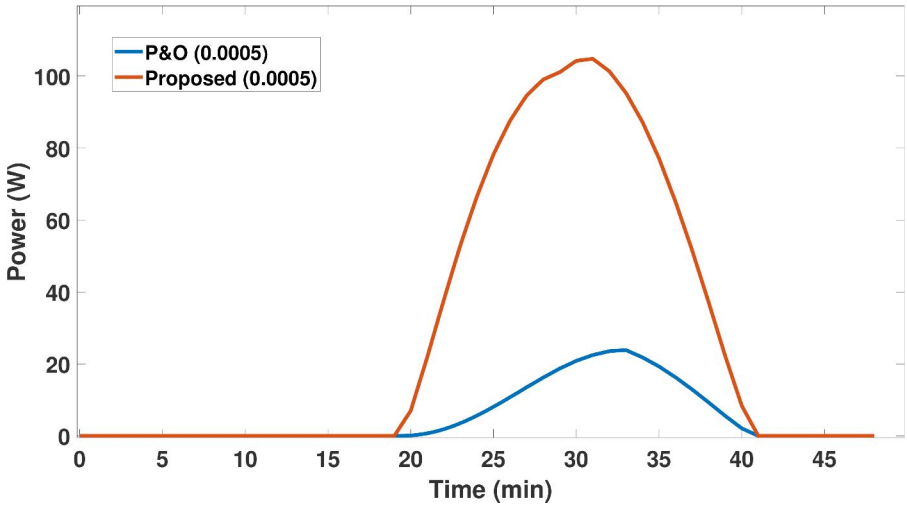

Figure 2.12: Comparison between proposed and P&O algorithm at the step size of 0.0005 for a sunny day

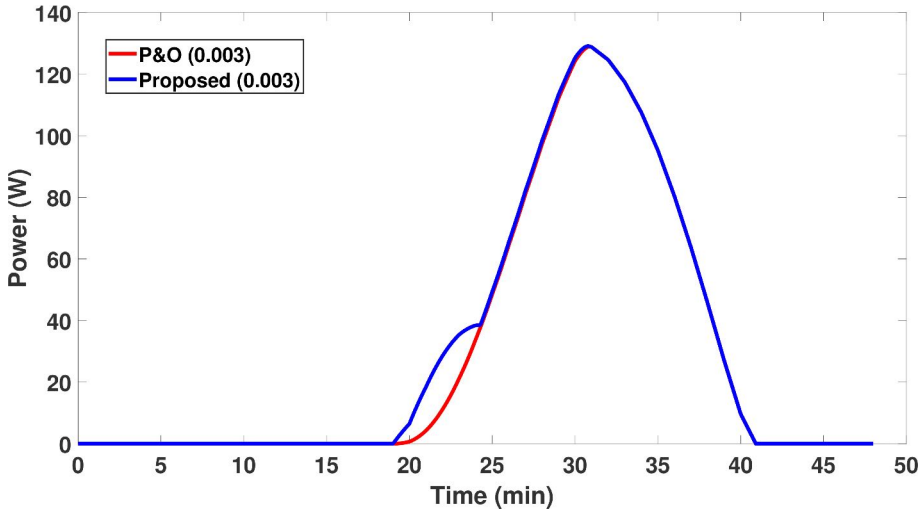

Figure 2.13: Comparison between proposed and P&O algorithm at the step size of 0.003 for a sunny day

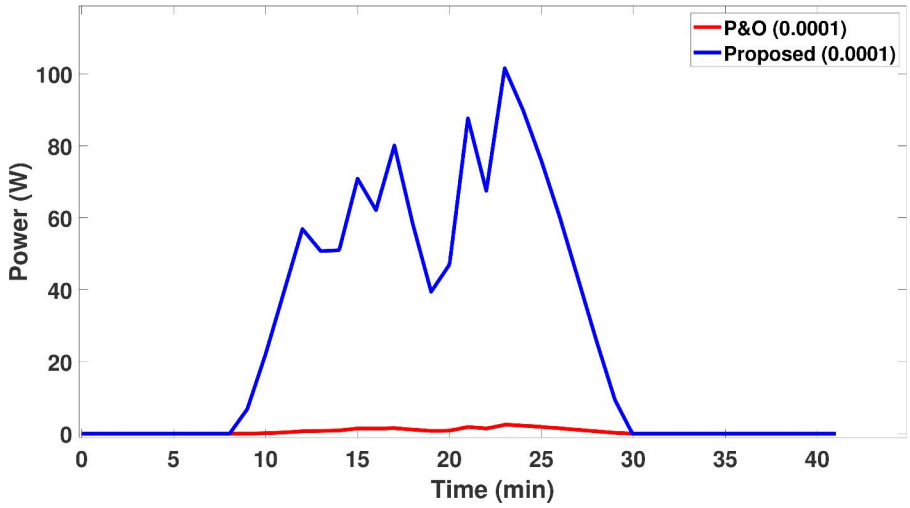

Figure 2.14: Comparison between proposed and P&O algorithm at the step size of 0.0001 for a cloudy day

In order to find the optimum step size of both P&O and the proposed algorithm and comparison, the linear-search-based algorithm that is shown in Fig. 2.4, is utilized, the results of which are depicted in Table 2.2. The energy generation results using the conventional P&O and the proposed algorithm are presented in Table 2.2 for the following step sizes: 0.0001, 0.0005, 0.003, 0.3. As can be seen from the table that the proposed algorithm outperforms the conventional P&O method at

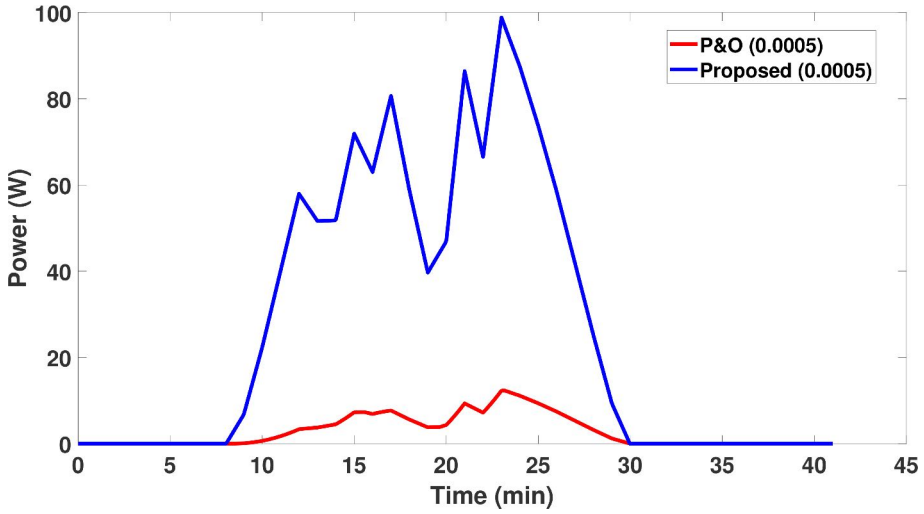

Figure 2.15: Comparison between proposed and P&O algorithm at the step size of 0.0005 for a cloudy day

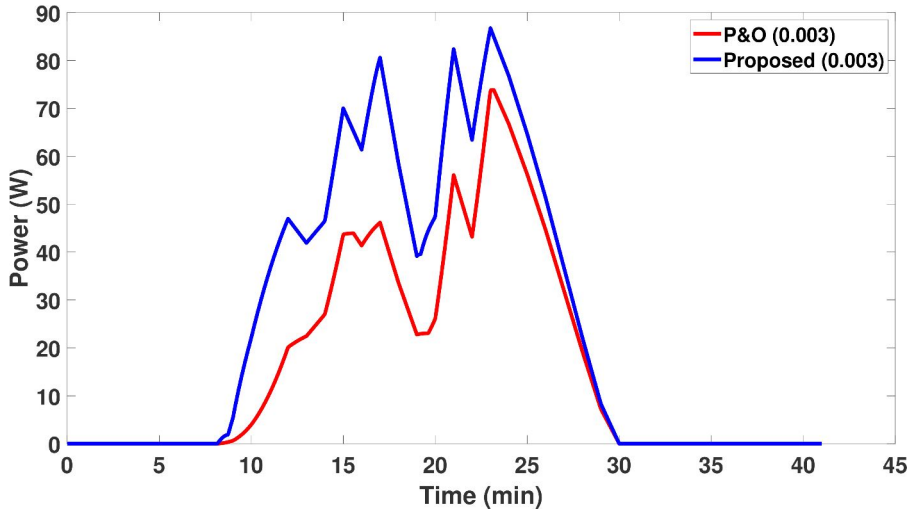

Figure 2.16: Comparison between proposed and P&O algorithm at the step size of 0.003 for a cloudy day

every step size. For the rapid weather change, the optimal step size for the P & O is found to be 0.003 which generates 388.61 Wh energy whereas the proposed algorithm generates 444.60 Wh. For steady irradiance changes, the P&O method produces 293.92 Wh energy at an optimum step size of 0.3 whereas the proposed method generates 321.86 Wh energy.

Table 2.2: Energy generation by P&O and Proposed Algorithm

	Step size	Energy Generation Wh	
		P & O	Proposed Algorithm
Fast changing GHI	0.0001	14.29	462.92
	0.0005	71.48	472.94
	0.003	388.61	444.60
	0.3	240.45	475.78
Slow changing GHI	0.0001	7.66	302.47
	0.0005	38.28	287.36
	0.003	229.60	253.71
	0.3	293.92	321.86

2.3 Summary

The comparison of energy generation based on different step sizes has been analyzed using the proposed algorithm with the P&O algorithm. Simulation results confirmed that the proposed algorithm is capable of extracting more energy than the P&O algorithm at any step size. The proposed algorithm generates 14.4% more energy than the P&O for smooth irradiance at the optimized step size of 0.003 and generates 9.5% more energy for fluctuating irradiance at the optimized step size of 0.3.

In future work, heuristic optimization tools such as the genetic algorithm, and particle swarm algorithm will be utilized to find the optimum step size that would provide the opportunity to find the most optimum step size from a larger search space for extracting maximum energy for the whole year data. The proposed algorithm will also be validated experimentally and a machine learning-based irradiance classification predictor will be researched to differentiate the fluctuating and smoothing irradiance to make the whole system automated.

CHAPTER 3

A BINARY SEARCH ALGORITHM BASED OPTIMAL SIZING OF PHOTOVOLTAIC AND ENERGY STORAGE SYSTEMS

The chapter starts by describing the optimization cost function to determine the optimal number of PVs and Batteries for a given load condition with the desired constraints. Then it applies Binary Search Algorithm to the Battery arrays to come up with the optimal cost for the given load condition. The algorithm uses real-field data to verify the proposed methodology.

3.1 Proposed Cost-Load Rejection-Based Algorithm

According to [84, 85], a search-based algorithm is designed to find a particular item from a dataset or data structure. There are several varieties of search algorithm methods in literature which include, linear search (also known as exhaustive search), fractional search, binary search, jump search, and exponential search among others [86]. The linear search algorithm is the simplest amongst the aforementioned methods and very easy to implement and suitable for less number of elements in the dataset [87]. The algorithm can start either from the lowest or highest value in the dataset and keep on searching one by one element exhaustively until it finds the desired target value. Therefore, the computational complexity is proportional to the total number of elements in the dataset. After the analysis of every possible cases, the average number of iterations can be expressed as (3.1) [88].

$$iter = \frac{(n+2)(n-1)}{2n} \tag{3.1}$$

where n is the total number of elements in the dataset.

On the other hand, the binary search algorithm starts by taking the average of the lowest and highest index of the dataset. It then compares the value of the middle

index with the desired one from the sorted data list. If the value gets matched, the algorithm stops, if the value at the middle index is lower than the desired value, the algorithm only searches the lower portion of the dataset and if the value is higher than the desired value, then it searches only on the upper subset of the data. The process is continued until the desired value is found. Based on the analysis for all possible scenarios, the average number of iterations can be calculated by using (3.2)

$$iter = \log_2(n) \tag{3.2}$$

Comparing equations 1 and 2, it can be inferred that the binary search algorithm is much faster than the exhaustive search, especially when the number of elements,n in the dataset is larger.

The flowchart of the binary search algorithm is illustrated in Fig.3.1 where mid denotes the middle index of the array, and low and high denotes the lowest and highest index of the sorted array.

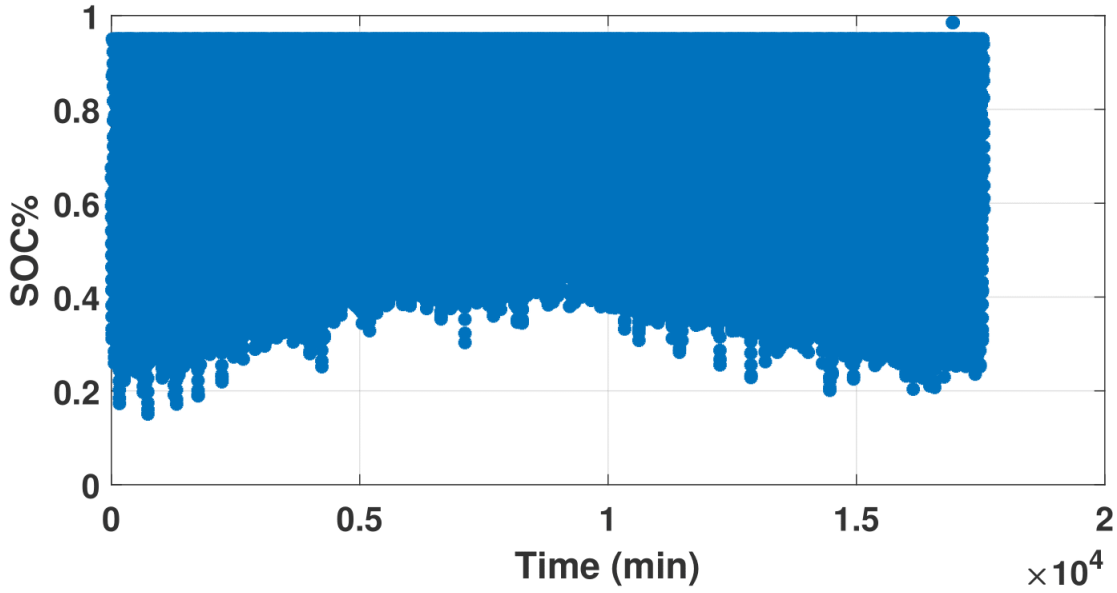

Figure 3.1: Flowchart of Binary Search Algorithm

Proposed Binary Search-based Optimization Algorithm

In the initialization process of the algorithm, the load data, temperature, and global horizontal irradiance (GHI) data for the entire year are kept in arrays. It then creates an array of PV modules sorted in ascending order and another array of batteries that are also sorted in ascending order. The algorithm calculates the maximum power at different GHIs and temperatures using (3.3) [89],

$$P_t^{pv} = N^{pv} P_{stc}^{pv} \left[\frac{G_t}{G_{stc}} \Big(1 - \kappa (T_t + \frac{G_t}{G_{NOCT}} (NOCT - 20) - T_{stc}) \Big) \right] \quad (3.3)$$

where N^{pv} is the number of PV arrays, P_{stc}^{pv} is the PV array power, G_{stc} is the irradiance at standard test conditions, T_{stc} is the temperature at standard test conditions, G_t is the irradiance at time t, $NOCT$ is the nominal operating cell temperature of PV array, G_{NOCT} is the irradiance at nominal operating cell temperature, and κ the temperature dependent degradation coefficient.

The algorithm then begins with a single PV module that generates the lowest amount of PV energy and then searches for the optimum battery from the battery array using the binary search algorithm. After calculating the middle index by averaging the highest and lowest index number, the algorithm checks whether the corresponding battery at the middle index number and PV module pair is capable of supplying the entire load demand throughout the year on an hourly basis. This can be accomplished by taking the summation of the total load deficit for the year. If it finds the total load deficit to be zero then it checks whether the total load deficit for the previous battery and current PV combination is non-zero. If this is the case, the algorithm finds the optimum battery for the current PV module. However, if

Algorithm 3 Algorithm for Optimum Battery and PV at Minimum Cost

Input: in
Output: out

Initialisation :
$optCost = inf$
$optPV = -1$
$optBat = -1$
$n_{bat} = 1$ to M
LOOP Process
for $n_{pv} = 1$ to N **do**
  $E_{PV} = n_{pv} * E_{pv}$
  $high = length(n_bat)$
  $low = 1$
  $prevCost = inf$
  while $high > low + 1$ **do**
    $step = step + 1$
    $mid = floor((low + high)/2)$
    $curStatus =$ Algorithm 2 for $n_{bat}(mid)$
    $preStatus =$ Algorithm 2 for $n_{bat}(mid - 1)$
    $cost$
    if $curStatus = 0$ and $preStatus \neq 0$ **then**
      $break$
    else if $curStatus = 0$ and $preStatus = 0$ **then**
      $high = mid$
    else
      $low = mid$
      $prevCost = curCost$
    end if
  end while
  if $curCost < optCost$ and $curStatus = 0$ **then**
    $optCost = curCost$
    $optBat = n_{bat}(mid)$
    $optBat = n_{pv}$
  end if
end for
return P

Algorithm 4 Algorithm for finding the status of Deficiency

Input: Irradiance data, Load data, PV, Battery;

Output: Return 1 When Total Deficit is not zero; Return 0 When Total Deficit is Zero;

Initialisation :

first statement

LOOP Process

for $t = 1$ to T **do**

  if $(E_{pv}(t) > E_{load}(t))$ **then**

    $E_{bat} = E_{batState} + E_{pv}(t) - E_{load}(t)$

    if $E_{bat>=E_{bat}^{max}}$ **then**

      $extra = E_{bat} - E_{bat}^{max}$

      $deficiency = 0$

      $E_{batState} = E_{bat}^{max}$

    else

      $extra = 0$

      $deficiency = 0$

      $E_{batState} = E_{bat}$

    end if

  else if $(E_{pv}(t) < E_{load}(t))$ **then**

    $E_{bat} = E_{batState} - (E_{load}(t) - E_{pv}(t))$

    if $E_{bat<E_{bat}^{min}}$ **then**

      $extra = 0$

      $deficiency = E_{batState} - E_{bat}$

      $E_{batState} = E_{bat}^{min}$

    else

      $extra = 0$

      $deficiency = 0$

      $E_{batState} = E_{bat}$

    end if

  end if

end for

if $\sum_{t=1}^{365} deficiency(t) = 0$ **then**

  $status = 0$

else

  $status = 1$

end if

return *status*

the total deficit is zero for the current PV module and the previous battery pair, the algorithm search only the left lower portion of the battery array. Therefore, the algorithm doesn't require checking all the elements in the battery array in a brute-force way, thus, expediting the whole process. It then calculates the cost function shown in equation 9.5 and replaces the previous cost value with the current cost value if the current cost value is lower than the previous case. The algorithm keeps on repeating the aforementioned process until finishing all the elements from the PV modules array. Algorithm 1 and Algorithm 2 illustrate the working process of concept formation. The cost minimization objective function and the other constraints are as expressed as (9.5) and (9.6) respectively,

Objective Function:

$$Cost = min(\alpha * n_{pv} + \beta * n_{bat} + \gamma) \tag{3.4}$$

Subject to:

$$\begin{cases} SOC_{min} \leq SOC \leq SOC_{max} \\ n_{pv}^{min} \leq n_{pv} \leq n_{pv}^{max} \\ n_{bat}^{min} \leq n_{bat} \leq n_{bat}^{max} \\ \sum_{t=1}^{n} deficiency(t) = 0 \end{cases} \tag{3.5}$$

where α is the unit cost of PV in $\$/kWh$, β is the per unit cost of battery in $\$/kWh$, γ is the total constant costs including the replacement cost of the battery for degradation, installation cost, etc while n is the total time interval for a year.

3.2 Results and Discussions for a Case study

In order to evaluate the performance of the proposed algorithm, a case study of the actual annual load profile of a facility located in Miami is considered. The load profile is as shown in Fig. 3.2.

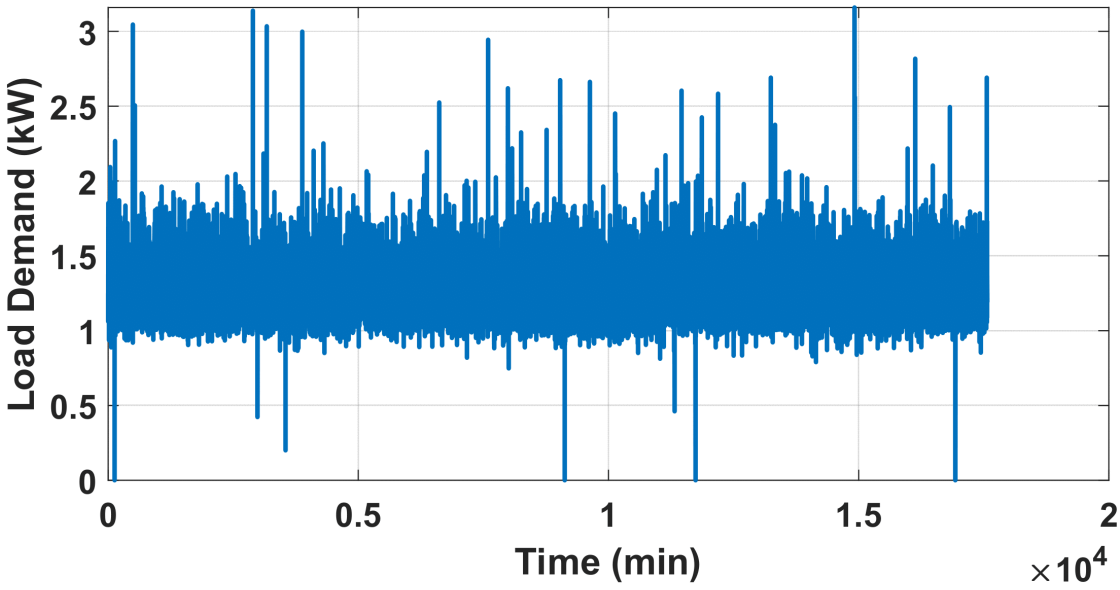

Figure 3.2: Load demand for one year

The energy demand is nearly constant due to the 24/7 operation of the devices used in the facility. The yearlong GHI data (at the location 25.7617° N, 80.1918° W) is used as shown in Fig. 5.8.

For each day, 48 samples are taken, so there are altogether 17568 data samples for the entire year which is shown in the time-axis of the GHI and the load profile data. An ideal maximum power point tracker (MPPT) is considered in this case

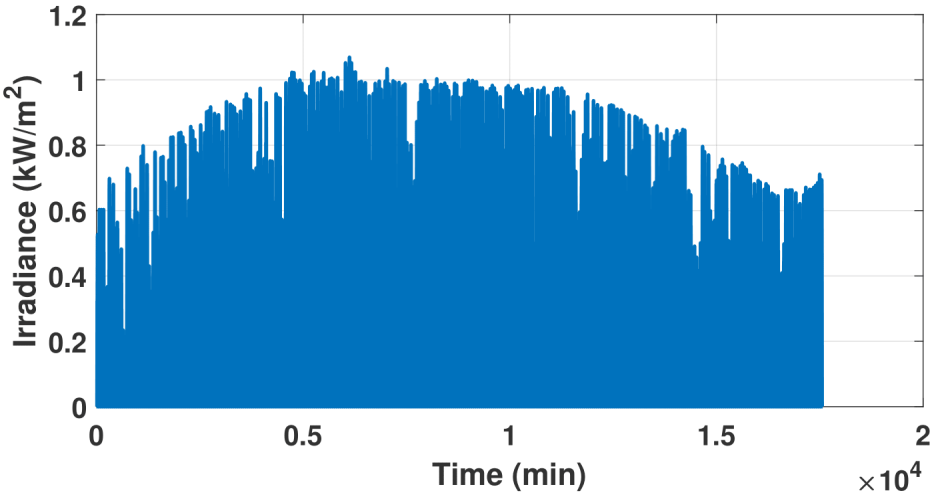

Figure 3.3: Solar Irradiance for one year

study. The specifications of the PV module and battery used in the simulation are presented in Table 3.1 and 3.2 respectively.

Table 3.1: Electrical characteristics of PV Module Specifications.

Maximum Power (P_{MAX})	315 W
Voltage at P_{MAX}(V_{MP})	54.7 V
Current at P_{MAX}(I_{MP})	5.7 A
Open Circuit Voltage (V_{OC})	64.4 V
Short Circuit Current (I_{SC})	6.0 A

Table 3.2: Electrical characteristics of Battery

Nominal Bank Capacity	100 Wh
Maximum SOC (SOC_{max})	95%
Minimum SOC (SOC_{min})	15%

After applying the proposed binary search-based algorithm to optimally size the PPB systems, the optimal number of PV-modules and batteries (go achieve minimum cost with zero load rejection) are found to be 146 and 504 respectively, which is shown in Fig. 3.4. The algorithm resulted in various PV-battery combinations,

which can be seen from the figure (i.e. Fig. 3.4.). The use of 146 PV modules and 504 batteries resulted in the minimum total cost of the system as expressed in (3.4).

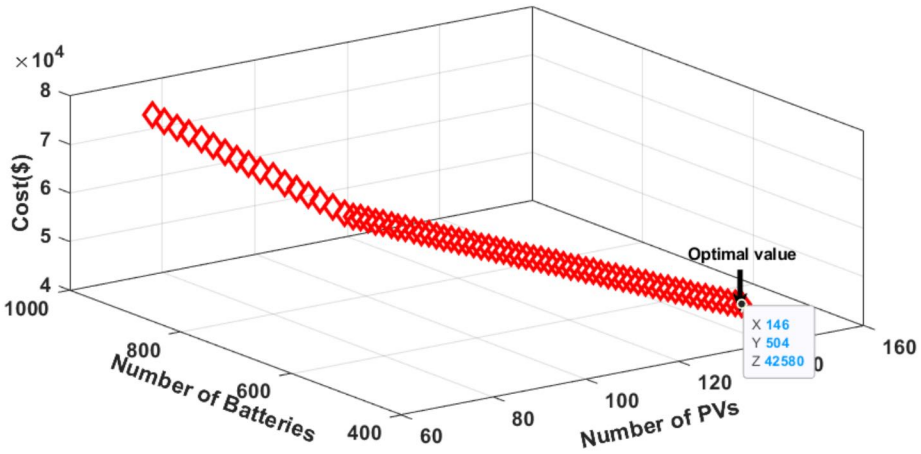

Figure 3.4: Optimum number of PVs and Batteries at minimum cost

Fig. 3.5 shows that the energy deficit by the optimal number of PV modules and batteries is zero for the whole year.

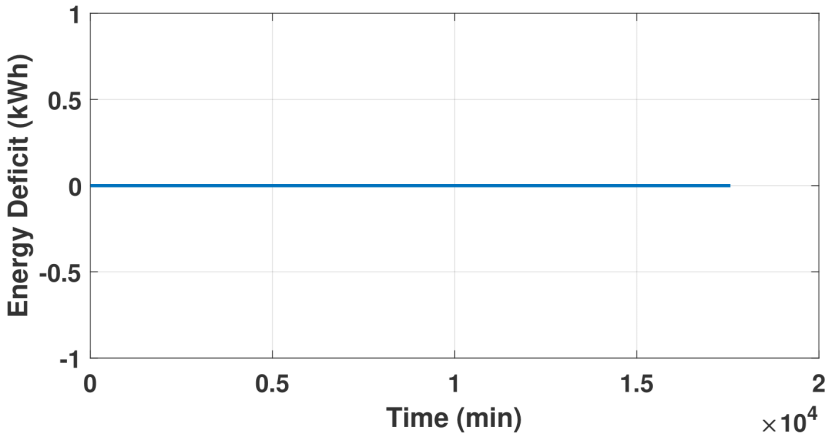

Figure 3.5: Zero Load Deficit for one year by the optimal number of batteries and PVs

In order to verify if the proposed binary search-based algorithm correctly found the optimal number of batteries and PV modules, we reduced the number of PV modules from 146 to 145, and the energy deficit produced is as shown in Fig. 3.6.

As we can see the energy deficit is a little greater than zero because of the reduction of one PV module from the optimal point. Fig. 3.7 also verifies that the state of charge of the battery remains within the predefined limit of SOC_{max} and SOC_{min} throughout the year. The maximum energy generated by the optimal number of PVs from the optimization is as shown in Fig. 3.8.

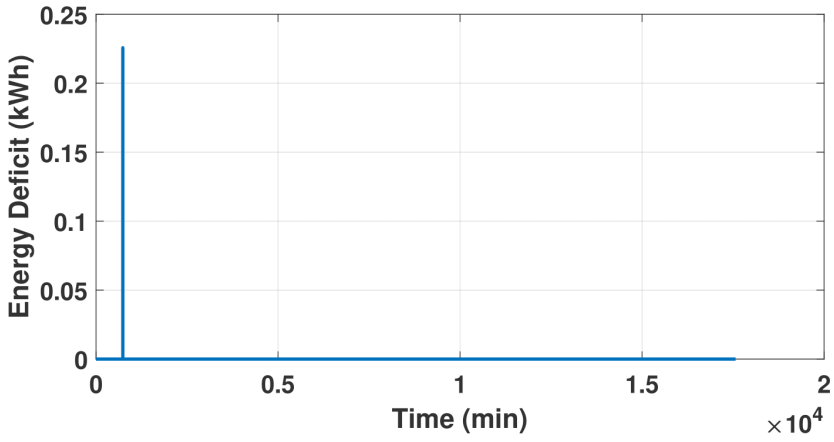

Figure 3.6: Load Deficit just before the optimum point

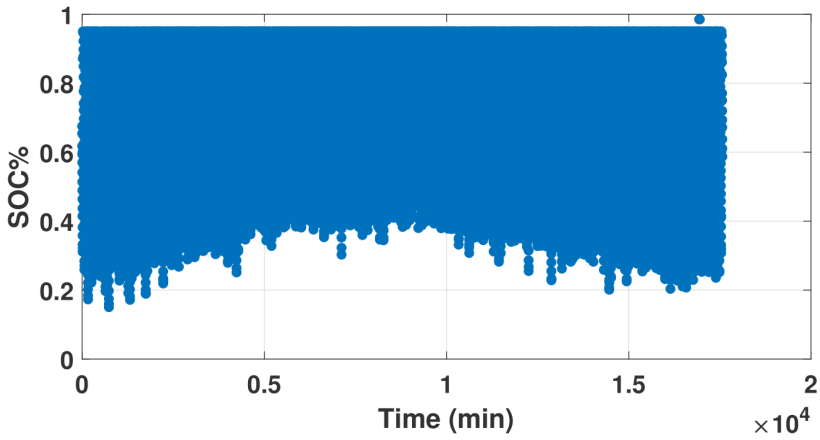

Figure 3.7: Battery state of charge for whole year

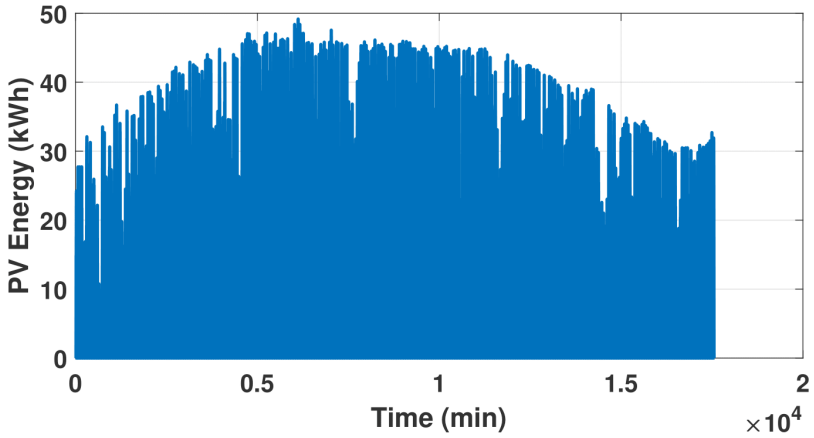

Figure 3.8: Maximum amount of PV Energy for one year by the optimum number of PVs

3.3 Summary

This chapter proposes an offline optimization process of PV and battery at minimum cost based on a binary search algorithm in order for faster finding of the optimum parameters - number of PV modules and number of batteries. The algorithm is based on the use of long one-year practical irradiance and load data. The proposed algorithm finds the optimum number of PV modules and batteries at the minimum cost. The objective function of the algorithm is based on the assumption that the total cost of the system is linearly dependent on the number of batteries and a number of PV modules. The simulation results verify that SOC_{max} and SOC_{min} remain within the predefined value - 95% and 15% respectively and the load deficit by the optimum parameters is zero throughout the year. This will help improve the battery's health, hence increasing the longevity of the battery life. At the application level, the proposed algorithm can be used by putting constraints on a number of PV modules and batteries based on the space availability of a particular location.

CHAPTER 4

PARTICLE SWARM OPTIMIZATION-BASED PID CONTROLLER DESIGN FOR DC-DC BUCK CONVERTER

This chapter provides a detailed overview of different transient analyses for buck-converter and compares four different objective functions - each of them has a different focus on addressing the transient issues - for input side and output side disturbances. Section 4.1 describes the open loop transfer function, section 4.2 provides a vivid description of the PID control system, section 4.3 describes particle swarm optimization algorithm, and four different objective functions with their constraints, section 4.4 analyze the results with performance analysis and section 9.3 provides the overall summary of the chapter.

4.1 DC-DC Buck Converter

The DC-DC buck converter is shown in Fig. 4.1, by a schematic diagram.

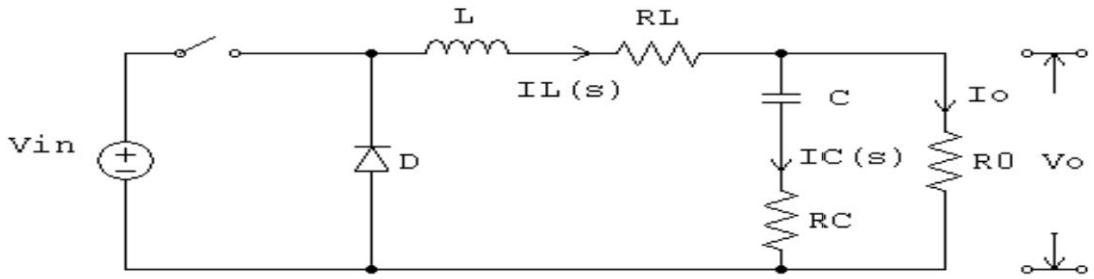

Figure 4.1: DC Bulk schematic diagram

In Fig. 2, V_o is noted for output voltage, D is for Duty cycle, C is for output filter capacitance, L is for inductance, and R_0 is the load resistance. However, R_L and R_C are the equivalent series resistance (ESR) of the inductor and capacitor respectively.

In small signal analysis, the control to output transfer function is given in equation 1, and the input to output transfer function is given by equation 2 [90].

$$\frac{\widehat{V}_o(s)}{\hat{d}(s)} = \frac{V_o}{D}\left[\frac{1+sR_CC}{denom}\right] \tag{4.1}$$

$$\frac{\widehat{V}_o(s)}{\hat{V_{in}}(s)} = \frac{R_oD}{R_o+R_L}\left[\frac{1+sR_CC}{denom}\right] \tag{4.2}$$

$$\begin{aligned} denom = 1 + s\left(R_CC + \frac{R_LR_O}{R_L+R_O}C + \frac{L}{R_L+R_O}\right) \\ +s^2LC\left(\frac{R_O+R_C}{R_O+R_L}\right) \end{aligned} \tag{4.3}$$

For simplicity, we have not considered ESR series resistance, R_L, and R_C.

4.2 PID Control System

The PID controller has three control parameters: proportional gain (K_p), integral gain (K_i), and derivative gain (K_d) which are vital for the controller to provide better performance. The method for finding the best control parameter is known as tuning. The PID control algorithm can be mathematically expressed as (4.4) and (4.5)

$$u(t) = K\left(e(t) + \frac{1}{T_i}\int_0^t e(t)d\tau + T_d\frac{d(e(t))}{dt}\right) \tag{4.4}$$

$$u(t) = K_pe(t) + K_i\int_0^t e(t)dt + K_d\frac{d(e(t))}{dt} \tag{4.5}$$

Here $u(t)$ is the control variable and $e(t)$ is the error between V_{ref} and V_{out}. The proportional term, K_p is responsible for the faster response when an error occurs while the integral term, K_i is responsible for reducing the steady-state errors. The

derivative control mode, denoted by K_d, provides additional control action to the controller when the error varies consistently. It also makes the system more stable that which allows using a higher controller gain and a faster integral gain.

There are four basic parameters [91]: rise-time (t_r), settling time (t_s), overshoot (δ), and steady-state error (ess) - that are used in order for evaluating the performance of DC-DC converter controller within a desired voltage range. All the parameters are shown pictorially in Figs. 4.2 and 4.3.

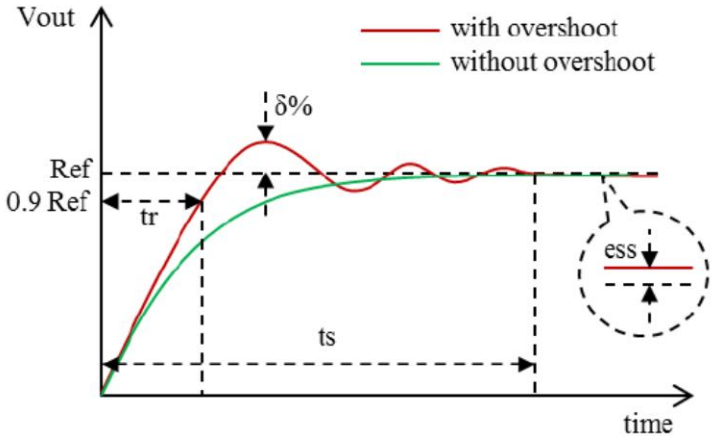

Figure 4.2: Response of DC-DC converter during starting

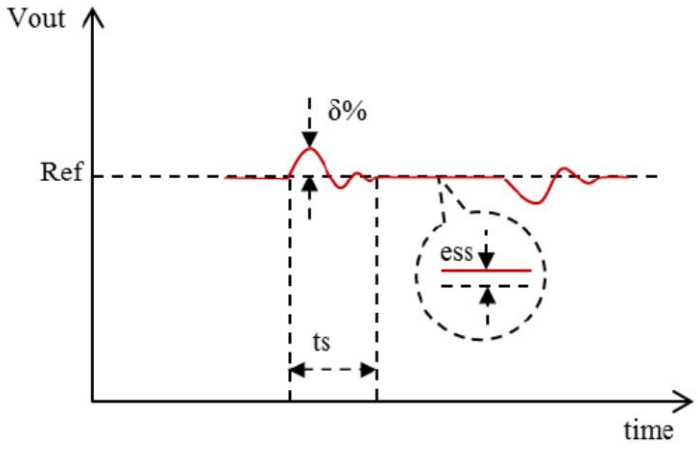

Figure 4.3: Response of DC-DC converter during transition

4.3 PSO-based controller parameters design

PSO was born out of a two-dimensional space simulation of bird flocking. To find the best solution, it employs a number of particles, known as candidate solutions, pBest that fly around in the search room. Meanwhile, the particles in their paths are all looking for the right particle, known as the best solution, gBest. To put it another way, particles consider both their own best solutions and the best solution discovered so far. The current location, current velocity, the distance between the current position and pBest, and distance between the current position and gBest are all used by each particle and try to change its position [92]. Figure 4.4 shows the flowchart of the PSO algorithm.

The PSO can be expressed mathematically using (4.6)-(4.8) [92]:

$$\begin{aligned} v_i^k(t+1) = w(t)v_i^k(t) + C_1 r_1 \left(pBest_i^k(t) - x_i^k(t)\right) \\ + C_2 r_2 \left(gBbest^k(t) - x_i^k(t)\right) \end{aligned} \tag{4.6}$$

$$x_i^k(t+1) = x_i^k(t) + v_i^k(t+1) \tag{4.7}$$

$$w(t) = \frac{(t_{\max} - t)\,(w_{\max} - w_{\min})}{(t_{\max} - 1) + w_{\min}} \tag{4.8}$$

Where, $x_i^k(t)$ denotes the position of the $i-th$ particle of the $k-th$ control variable at time(iteration) t, $v_i^k(t)$ denotes the velocity of the $i-th$ particle of the $k-th$ control variable at a time(iteration) t, $w(t)$ is the weighting factor of inertia that can be expressed dynamically by (4.8), C_1 and C_2 are positive-constants and r_1, r_2 are the random numbers that are uniformly distributed in the range 0 to 1.

The PSO algorithm will be deployed to minimize the cost of four objective functions stated below:

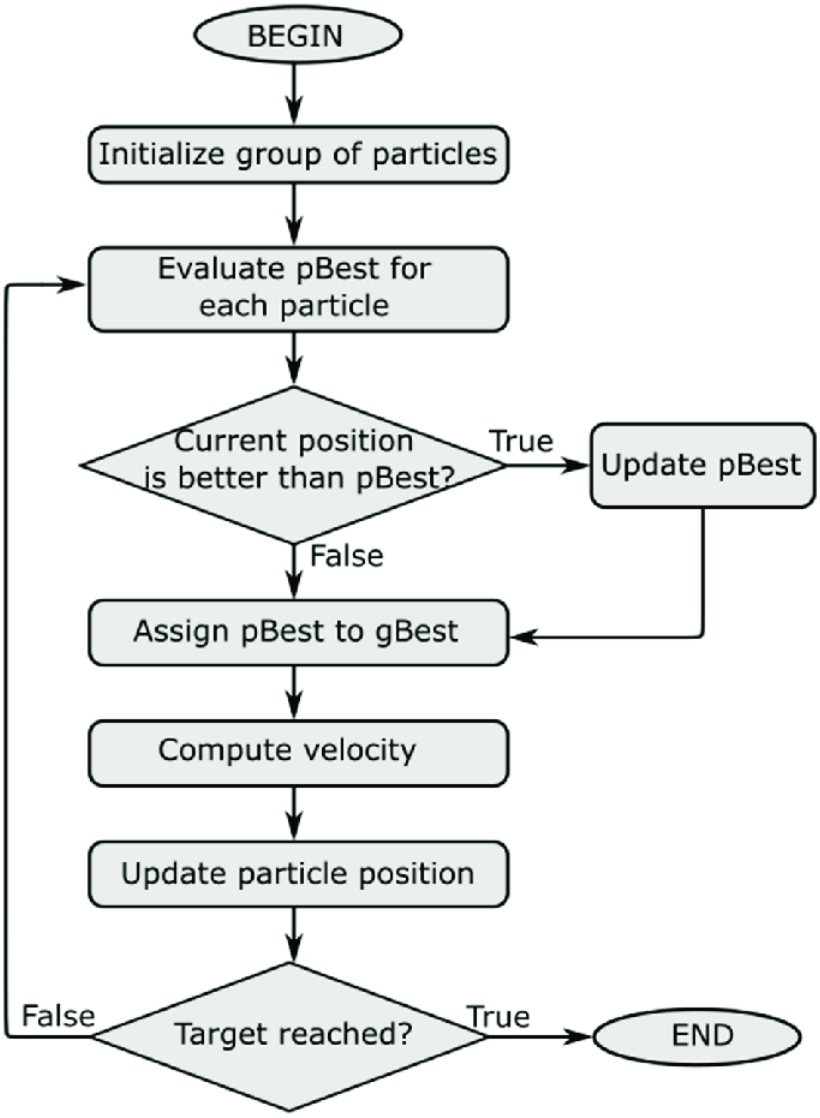

Figure 4.4: Particle Swarm Optimization Algorithm

$$IAE = \int_0^\infty |e(t)|dt \tag{4.9}$$

$$ISE = \int_0^\infty e^2(t)dt \tag{4.10}$$

$$ITSE = \int_0^\infty te^2(t)dt \tag{4.11}$$

$$ISTSE = \int_0^\infty t^2 e^2(t) dt \tag{4.12}$$

Where: $e(t) = V_{ref} - V_{out}$

By principal, IAE will be used to suppress the minute errors between V_{ref} and V_{out}. In doing this, IAE takes the absolute value of the errors. In parallel, ISE will remove the large errors because it squared the errors. ITSE will be helpful in reducing the rising time with a relatively small overshoot, however, a longer settling time might occur because it integrates the time parameter linearly. In that regard, ISTSE will be helpful in reducing the settling time and steady-state errors since it squares the time [93].

Mathematically, the optimization problem can be represented in the following compact form:

Objective Function:

$$\begin{aligned} F_1 = min\left| \int_0^\infty |e(t)| dt \right|; F_2 = min\left| \int_0^\infty e^2(t) dt \right|; \\ F_3 = min\left| \int_0^\infty te^2(t) dt \right|; F_4 = min\left| \int_0^\infty t^2 e^2(t) dt) \right| \end{aligned} \tag{4.13}$$

Subject to:

$$\begin{cases} K_p^{min} \leq K_p \leq K_p^{max} \\ K_i^{min} \leq K_i \leq K_i^{max} \\ K_d^{min} \leq K_d \leq K_d^{max} \end{cases} \tag{4.14}$$

4.4 Simulations and Dynamic Performance Analysis

In order to implement and examine the PSO for the buck converter's voltage regulation, Simulink/Matlab environment is chosen. The electrical parameter of the buck converter is provided in Table 4.1.

$$i_L = \frac{1}{L}\int_0^t (D \times V_{in} - V_{out})\, dt \tag{4.15}$$

$$v_C = \frac{1}{C}\int_0^t (i_L - i_{load})\, dt \tag{4.16}$$

In these expressions, i_L is noted for inductor current, D is Duty signal, and v_C is for voltage across the capacitor.

Table 4.1: Electrical parameters of Buck Converter

Input Voltage, V_{in}	$30 - 48V$
Desired Output Voltage, V_{out}	15 V
Load Resistance, R_{load}	3.0 to 5.0Ω
Inductance, L	1.5 mH
Capacitance C	250 μF

Fig. 4.6 shows the buck converter model based on equations (15) and (16) with input step change from $48V$ to $30V$ at $0.02sec$ and load step change from 3Ω to 5Ω at $0.04sec$ as shown in Fig. 4.5.

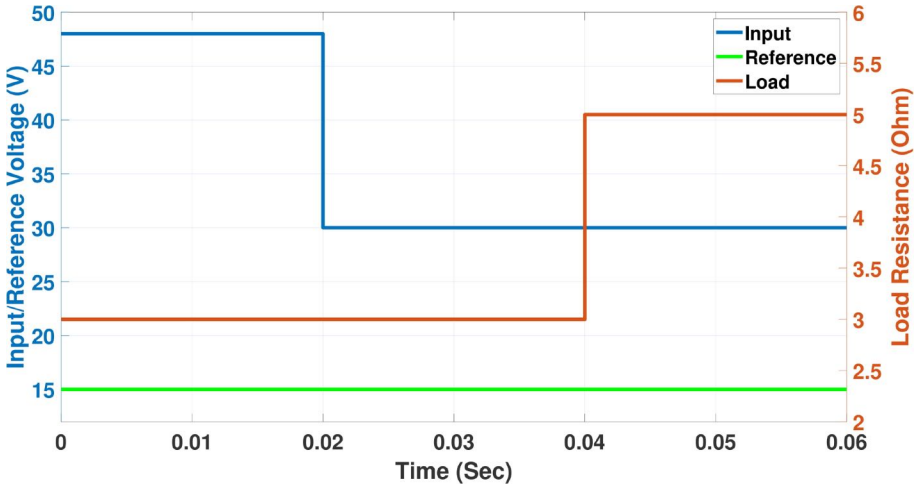

Figure 4.5: Input voltage, load resistance step change, and reference voltage for testing

The simulation was run for $0.06sec$. The reference voltage is set at $15V$. The mathematical model of the closed loop buck converter, shown in Fig. 4.6, models the MOSFET/IGBT switch by $D \times V_{in}$ where D varies from $0 - 1$.

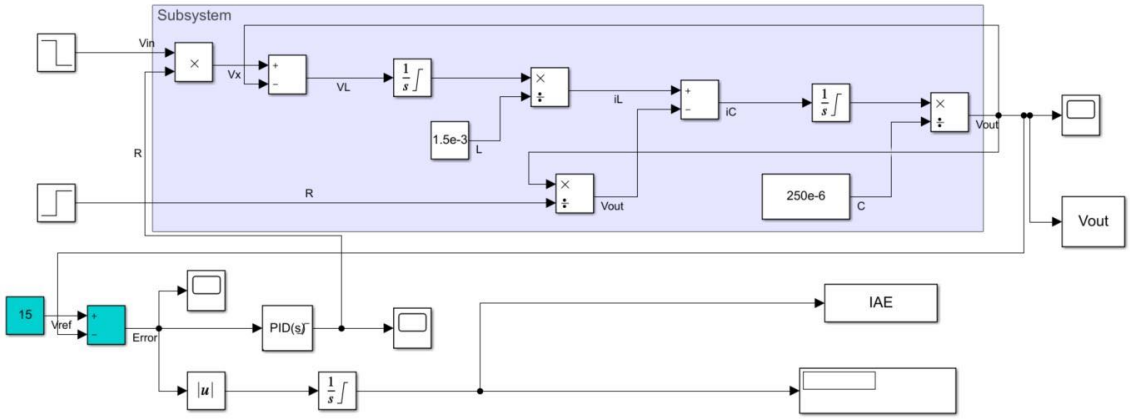

Figure 4.6: Mathematical model of Buck converter with input and output variations

We have not used any comparator in the Simulink model for comparing the duty signal to a high-frequency sawtooth wave to generate the pulse width modulation (PWM) signal, in order to expedite the whole simulation time.

The PSO algorithm along with the fitness function has been implemented in Matlab from which the Simulink buck-converter model control parameters have been called.

We start with the PI controller with the optimized K_p and K_i values, though the controller was able to track the reference voltage 15 V, there were high-frequency oscillations during the start-up period and also step load change period at 0.04 sec. Then the derivative controller has been added with a low pass filter. The cut-off frequency of the low pass filter has been estimated according to the high-frequency oscillations. The 4 different objective functions of the PSO algorithm are described with the constraints in the previous section in equation (13).

The details function of the PID controller is shown in Fig. 4.7 along with the low pass filter (LPF) to attenuate the high-frequency signals and Clamping control strategy for solving the anti-wind-up problem of the Integral Controller.

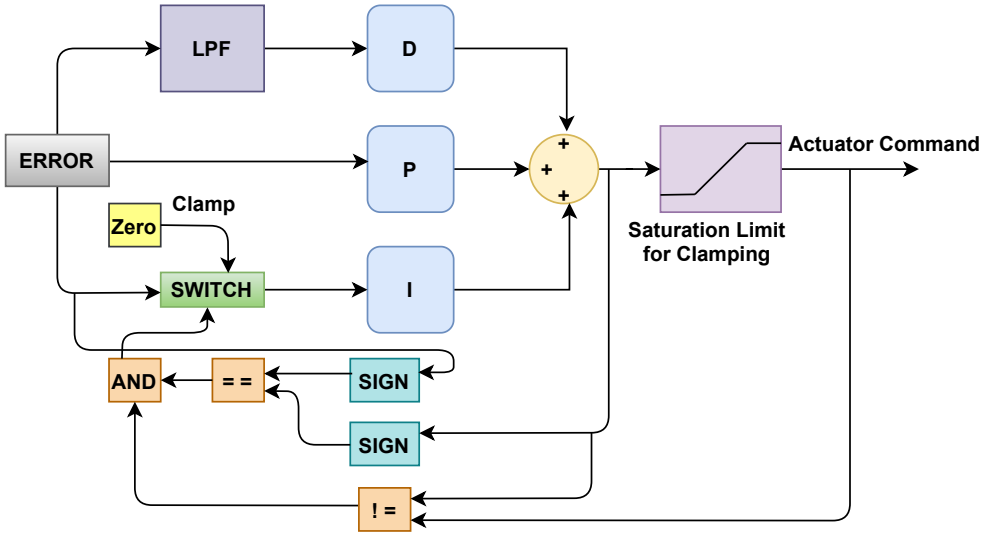

Figure 4.7: Detailed Block diagram of PID controller with LPF for Derivative and Clamping for Integral Controller

The PSO algorithm is run with a swarm size of 30 and the maximum number of iterations is chosen as 5. As we can see in Figs. 4.8-4.11, the minimum optimized values of the fitness function are obtained after 5 iterations. The lowest fitness function value is found by the ISTSE cost function. Figures 4.12-4.15 illustrate the output voltage graphs with the optimum control parameters of their corresponding fitness functions. As we can see in all those figures, oscillations, overshoots, and steady-state errors are very few, and rising time and settling time are very fast. Table 4.2 shows the optimal control parameters with their quantified values of performance and robustness using the 4 different fitness functions shown in Table 4.3.

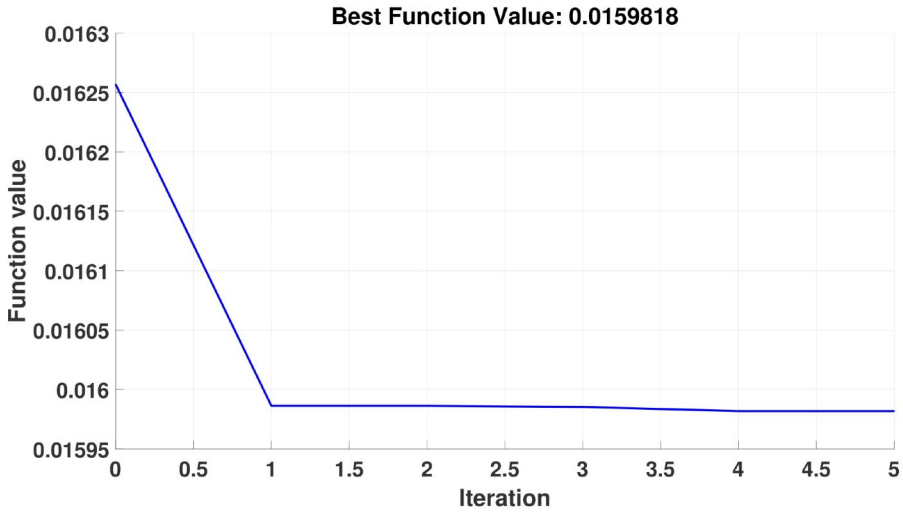

Figure 4.8: Finding the optimum value of ISE

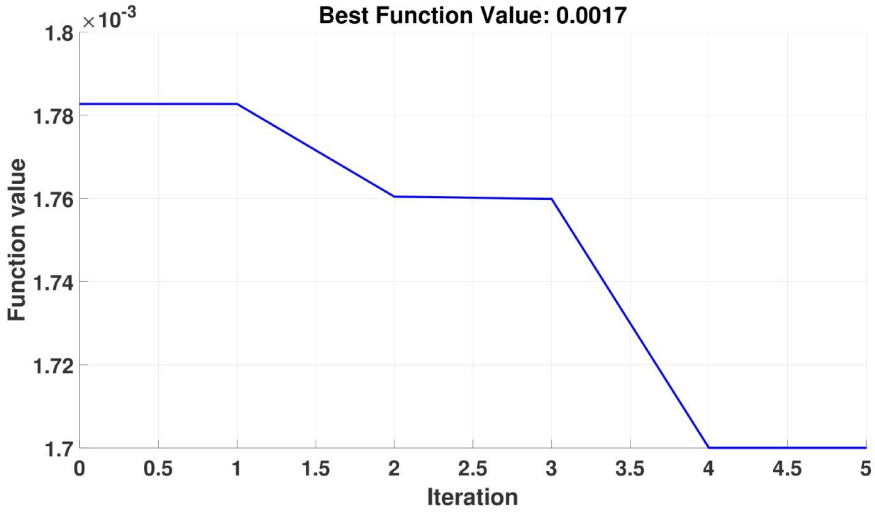

Figure 4.9: Finding the optimum value of IAE

Table 4.2: Controller Parameters

	ISE	IAE	ISTSE	ITSE
Proportional Gain, K_p	43.4615	99.1443	50	50
Integral Gain, K_i	28.7113	5.8938	100	92.9876
Derivative Gain, K_d	0.0017	0.0042	0.01	0.0023
Filter Coefficient, N	314740	715590	238630	726430

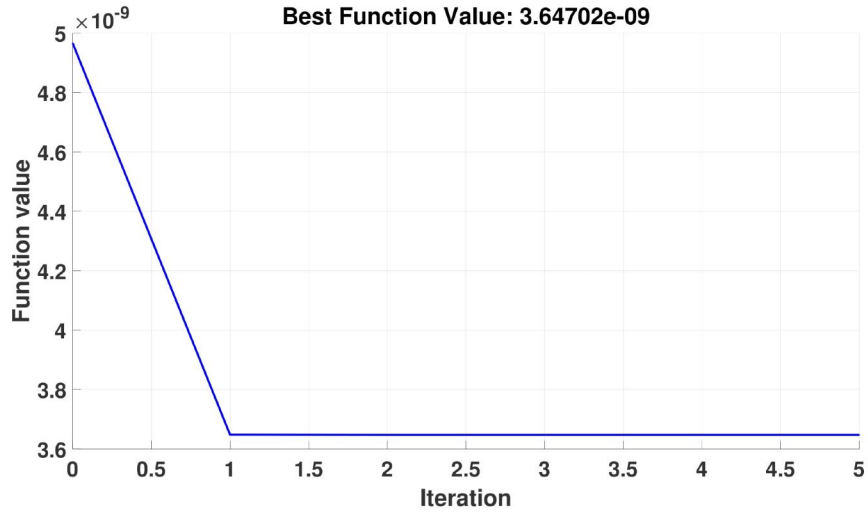

Figure 4.10: Finding the optimum value of ISTSE

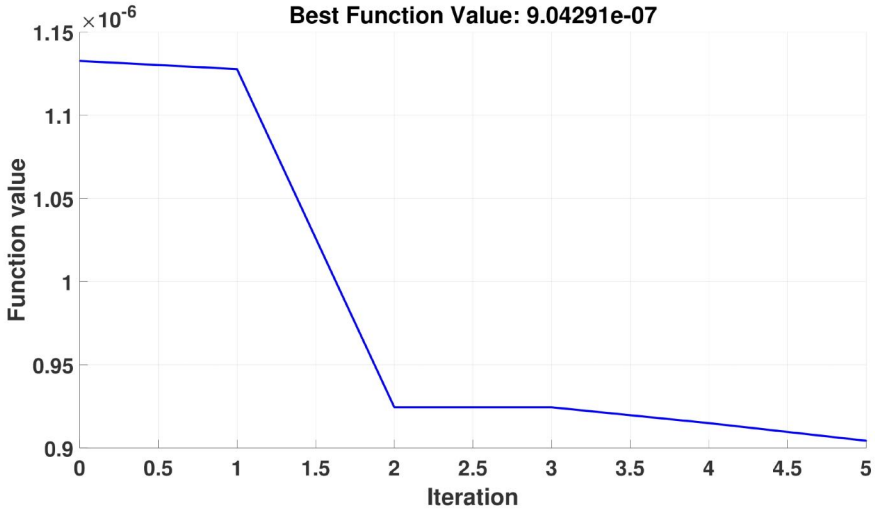

Figure 4.11: Finding the optimum value of ITSE

4.5 Summary

The research described in this chapter successfully implements PSO for finding the optimal parameters for the DC-DC Buck converter. Anti-wind up clamping method is also implemented in order for the best utilization of the integral controller. After the implementation of PSO for the optimization of PID controller parameters, the

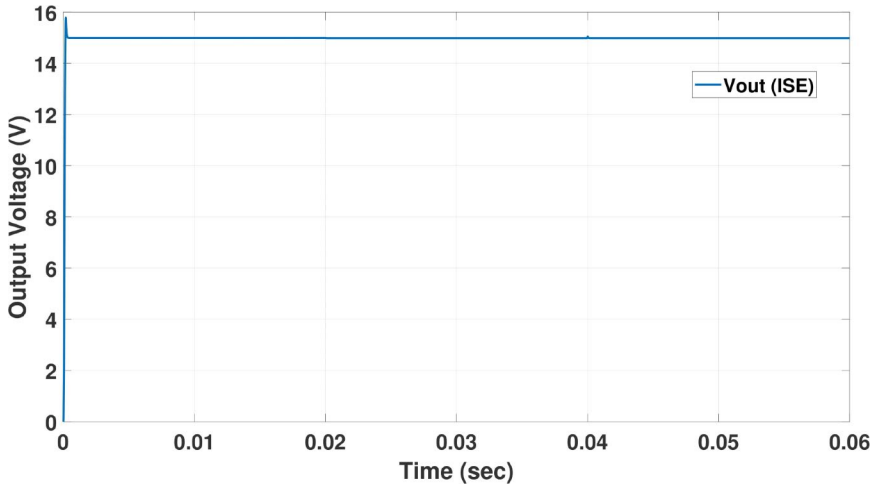

Figure 4.12: Output voltage using optimal parameters of ISE

Table 4.3: Performance and Robustness

	ISE	IAE	ISTSE	ITSE
t_r (sec)	6.1×10^{-6}	2.7×10^{-6}	2.2×10^{-6}	4.6×10^{-6}
t_s (sec)	6.8×10^{-5}	3.2×10^{-5}	3.1×10^{-5}	6.0×10^{-5}
δ	0.215	0.161	0.151	0.837
V_p (V)	15.26	15.16	15.51	15.08
Θ_m	51.2	54.3	23.7	64.7

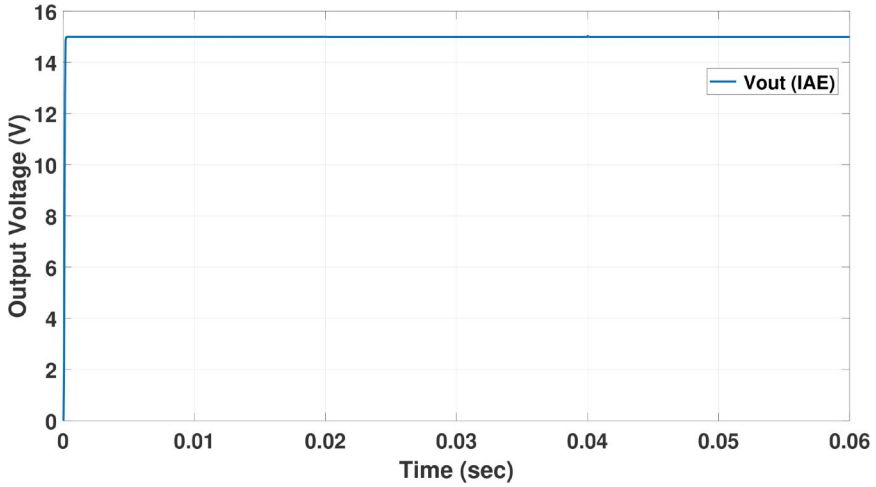

Figure 4.13: Output voltage using optimal parameters of IAE

results show promising results with very little oscillations and overshoots through the big step swing of input voltage from 48 V to 30 V at 0.02 seconds and load step

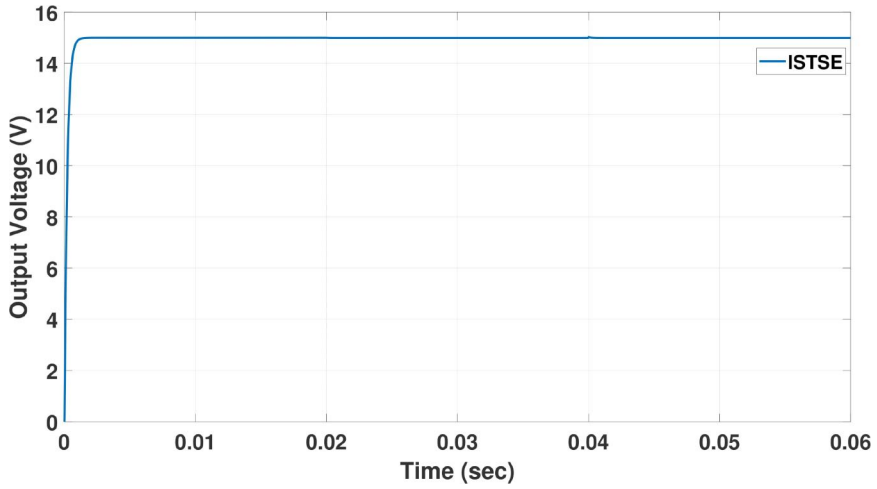

Figure 4.14: Output voltage using optimal parameters of ISTSE

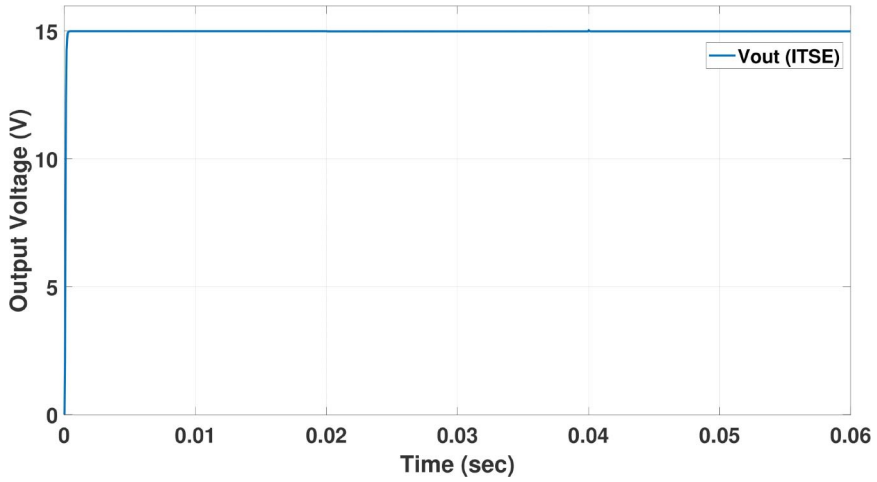

Figure 4.15: Output voltage using optimal parameters of ITSE

change from 3 ohms to 5 ohms at 0.04 seconds. The comparison of cost functions: ISE, IAE, ITSE, and ISTSE has been shown in the results; all the cost functions are minimized at their lowest possible values that confirms the robust determination of controller's parameters: K_p, K_i, and K_d. The output voltage vs time results obtained for all four different cost functions also resonate with better control parameters finding.

CHAPTER 5

VOLTAGE REGULATION AND BATTERY STRESS-REDUCTION STRATEGY FOR DC MICROGRID

This chapter proposes a PV-side controller which gets activated when the battery is fully charged to regulate the bus voltage within pre-defined limits. The proposed controller works coordinately with two other state-of-the-art MPPT and battery controllers to perform its duty. Section 6.1 describes the details about the proposed technology, section 5.2 provides the simulation results with detailed analysis, and section 9.3 summarizes the chapter.

5.1 Proposed Control Strategy

The proposed control strategy consists of three controllers which are: MPPT controller, battery controller, and PV-based voltage regulation controller. The control algorithm starts with measuring V_{bus} and SOC of the battery. The topology uses the measurement of the DC bus voltage to determine if the PV generates more energy than the load requirement and vice versa. For instance, if V_{bus} is higher than the V_{bus}^{ref}, then the PV is generating more power than the load, however when V_{bus} is less than the reference V_{bus}^{ref}, then the PV is generating less power than the load requires.

The algorithm checks if V_{bus} is higher than V_{bus}^{ref}, if the answer is YES, it checks whether V_{bus} is higher than V_{bus}^{max}, then it checks whether the SOC of the battery is higher than SOC^{max}. If the answer is YES, the control algorithm disconnects the battery since it's fully charged, then the PV-side voltage regulation controller kicks in to regulate the DC grid voltage. If the SOC of the battery is less than SOC^{max} then the battery is set to charging mode by the battery controller. If V_{bus} is less than V_{bus}^{ref}, the algorithm checks then whether V_{bus} is less than V_{bus}^{min} and also checks if

SOC is less than SOC^{min}. If the answer is YES, then it means the PV is generating less power than the load required and the battery is not capable of compensating for the deficit. In that scenario, the controller curtails some portion of loads to maintain system stability. However, if the SOC of the battery remains higher than SOC^{min}, then the battery controller sets the logic to discharge the battery in order for maintaining the DC bus voltage at the desired level. The complete flowchart of the control algorithm is shown in Fig. 5.1. The working principle of the controllers are described in **??-??**

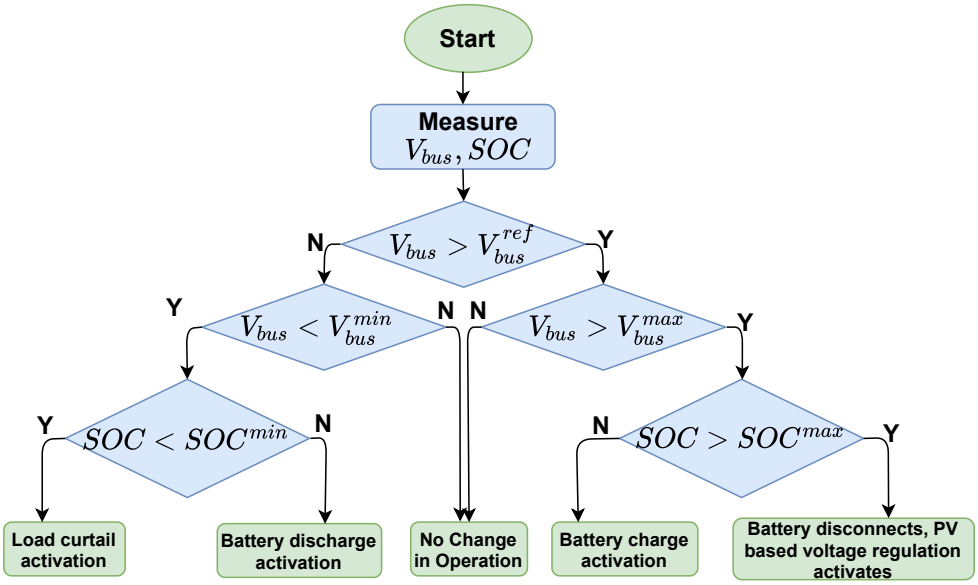

Figure 5.1: Flowchart of the Control Algorithm

5.1.1 MPPT controller for PV Boost converter

The P&O algorithm starts with an initial duty ration value that corresponds to a particular operating point on the P-V curve as shown in Fig. 5.3 [94]. After that, if the perturbation happens to be towards the right side, then ΔV should be positive, and ΔP should be positive as well. If the perturbation occurs towards the left

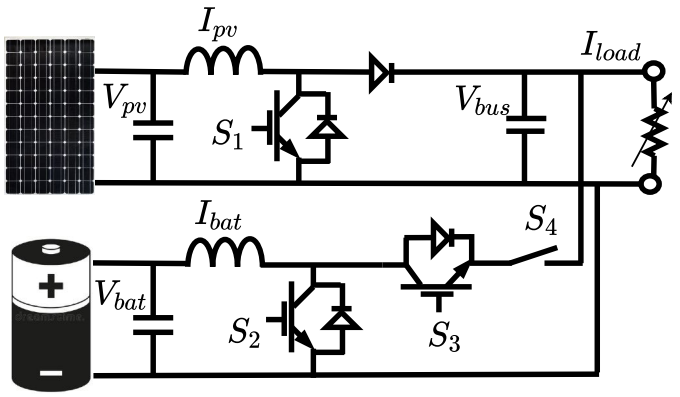

Figure 5.2: System architecture for the proposed DC microgrid

side then ΔV and ΔP are both negative. For the above-mentioned two cases, the algorithm perceives that the operating point lies at the left side of the maximum power point (MPP), it then drags the operating point towards the MPP. However, if the operating point lies at the left side of the MPP, then ΔV and ΔP generate opposite signs. The algorithm then drags the operating point towards MPP from the left side. The process is illustrated in Fig. 5.3.

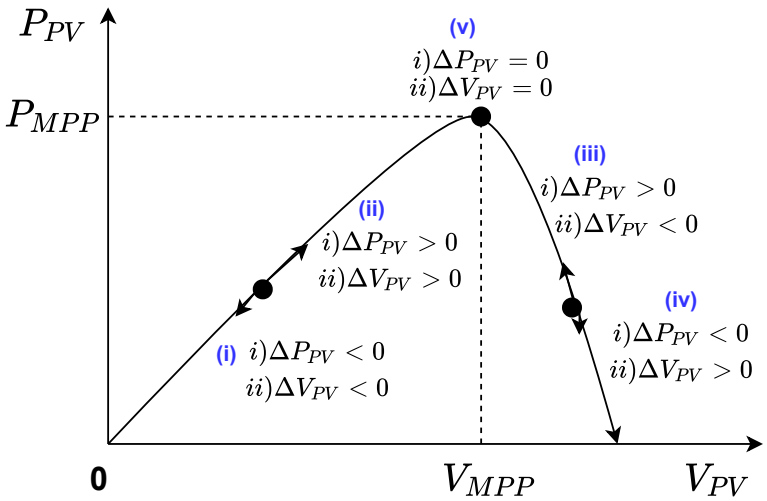

Figure 5.3: Concept behind P&O MPPT algorithm

The algorithm generates the desired reference signal, V_{MPP}, and compares it with the V_{pv}. The error signal is sent to a PI controller in order to generate the

desired PWM signal to drive the MOSFET of the PV-side boost converter. Fig. 5.4 shows the controller based on the modeling equation as expressed in (5.1).

$$c(t) = K_p^v(V_{MPP} - V_{pv}) + K_i^v \int_0^t (V_{MPP} - V_{pv})dt \tag{5.1}$$

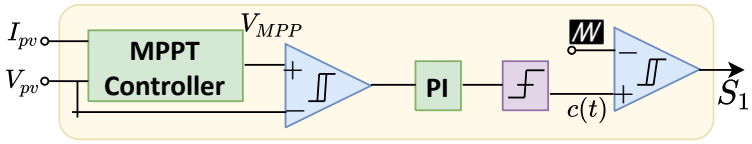

Figure 5.4: MPPT Controller

5.1.2 Voltage regulation controller for PV Boost Converter

The PV-based Voltage regulation controller gets activated by the controller whenever the battery is fully charged and PV is generating more power than the load is required. The controller is designed based on the following equations:

$$P_{pv}^{ref} = P_{bus} + P_{load} \tag{5.2}$$

where

$$P_{bus} = V_{bus}(K_p^v(V_{bus}^{ref} - V_{bus}) + K_i^v \int_0^t (V_{bus}^{ref} - V_{bus})dt)$$

$$P_{load} = V_{bus} I_{load}$$

During that period, the PV-based controller is the only controller for regulating the DC bus voltage. The controller does so by curtailing the power from PV modules in order for adjusting load demand, thereby regulating the bus voltage to a narrow range. Based on (5.2), the controller generates the reference power that eventually drags the operating point of PV modules towards the reference point. The detailed model of the controller is shown in Fig. 5.5.

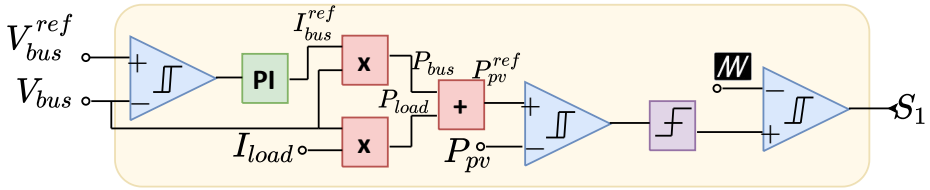

Figure 5.5: PV-based controller

5.1.3 Battery Controller for Buck-Boost Converter

The bi-directional buck-boost converter is designed to charge and discharge the battery in order to regulate the voltage across the DC bus. The power flow from $V_{bus} = 60V$ to $V_{bat} = 24V$ is maintained through the buck topology of the converter and V_{bat} to V_{bus} power flow is maintained by the boost topology. The battery controller as shown in Fig. 5.6 sends the appropriate signals to drive S_2 and S_3 IGBTs and maintains the coordination between them in switching from buck mode to boost mode and vice-versa. The buck mode is activated by the controller when the S_3 switch is ON and S_2 is OFF, the boost mode gets activated by switching ON S_2 and switching OFF S_3. In order to implement the above operation, the battery controller utilizes two cascaded PI controllers as shown in Fig. 5.6.

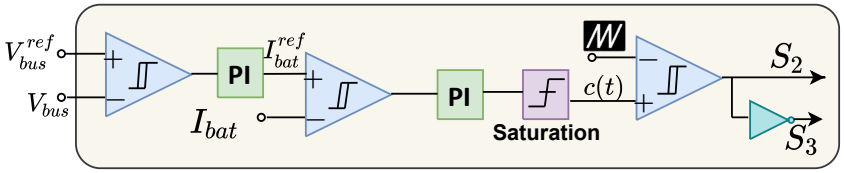

Figure 5.6: Battery Controller

The outer voltage control loop is used to regulate the V_{bus} to V_{bus}^{ref} and generates the reference signal for the inner current control loop. The inner current control loop then regulates the battery current towards the reference signal. The modeling of the voltage and current controller dynamics is as expressed as (6.6) and (6.7) respectively.

$$I_{bat}^{ref} = K_p^v(V_{bus}^{ref} - V_{bus}) + K_i^v \int_0^t (V_{bus}^{ref} - V_{bus})dt \tag{5.3}$$

$$u(t) = K_p^i(I_{bus}^{ref} - I_{bus}) + K_i^i \int_0^t (I_{bus}^{ref} - I_{bus})dt \tag{5.4}$$

5.1.4 DC Microgrid mode switching mechanism

The various DC microgrid modes of operation are as shown in the flowchart shown in Fig. 5.1. Each of these modes triggers the operation of one of battery Control, MPPT control, PV-based Voltage Control, or load curtailment. The mode switching mechanism uses three parameters of the microgrid to V_{bus}, SoC, I_{pv} to determine the appropriate mode of operation based on Fig. 5.1. The current parameter I_{pv} is taken as input to the mode-switching mechanism in order to detect the night mode option ($I_{pv} = 0$) where the battery will be solely responsible for supplying power to the load.

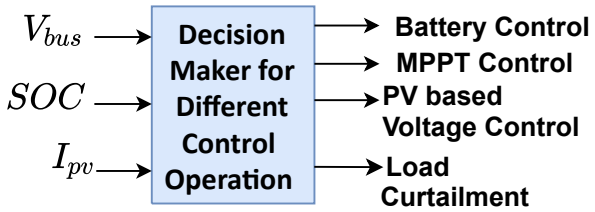

Figure 5.7: Supervisory Controller for decision making of different modes

5.2 Simulation Results and Discussion

In this section, the simulation results are discussed in three different cases which are depicted below:

CASE I: In the first investigated scenario, a step change in irradiance as shown in Fig. 5.8 is applied at 0.5 sec from 300 W/m^2 to 800 W/m^2 and The battery SoC has

been maintained well below SoC_{max} in order to check the controller's performance. In this mode, PV is supplying maximum power, and the battery is either charged or discharged based on the load power in order for regulating the bus voltage. Fig. 5.9 and Fig. 5.10 show that the DC bus voltage is well regulated at 60 V despite the irradiance changes and the load current remains mostly constant at 5 A for 12 Ω resistance. Fig. 5.11 shows that the maximum power is extracted from the PV array by the MPPT controller. Fig. 5.12 shows that the battery starts getting charged at 0.5 sec to regulate the dc bus voltage while the irradiance starts increasing from 300 W/m^2 to 800 W/m^2 and Fig. 5.13 shows that the battery current goes negative after 0.5 sec which confirms that the battery is in charging mode.

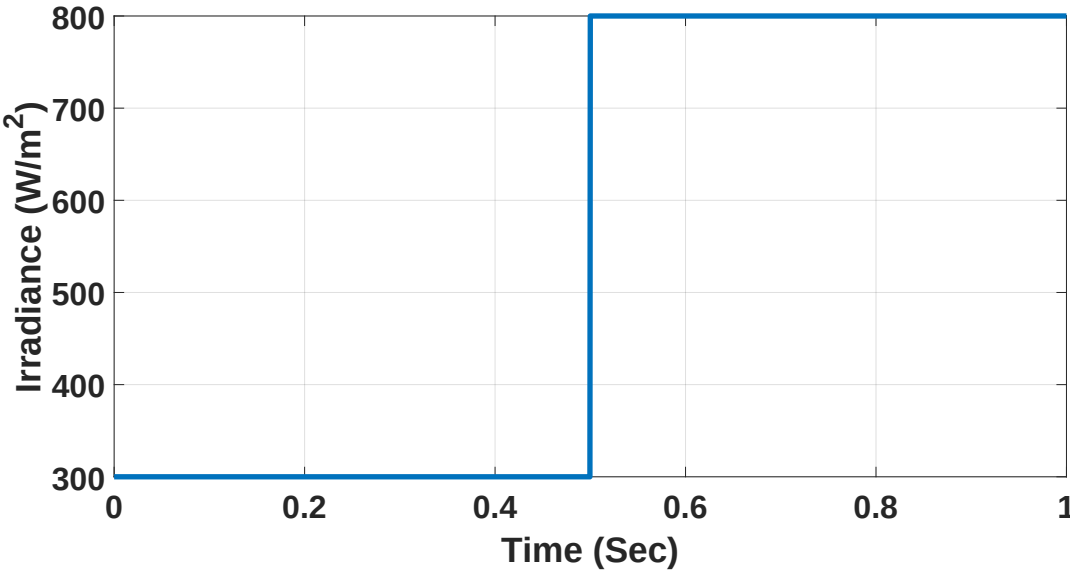

Figure 5.8: Step change in irradiance

CASE II: In this part of the simulation, battery SoC has been maintained above the maximum state of charge SoC^{max} to get the battery completely disconnected from the system and check whether PV based controller is capable of regulating the DC bus voltage on its own by curtailing PV power. The results are shown in Fig. 5.14 to Fig. 5.17. Fig. 5.14 and Fig. 5.15 show that DC bus voltage is regulated

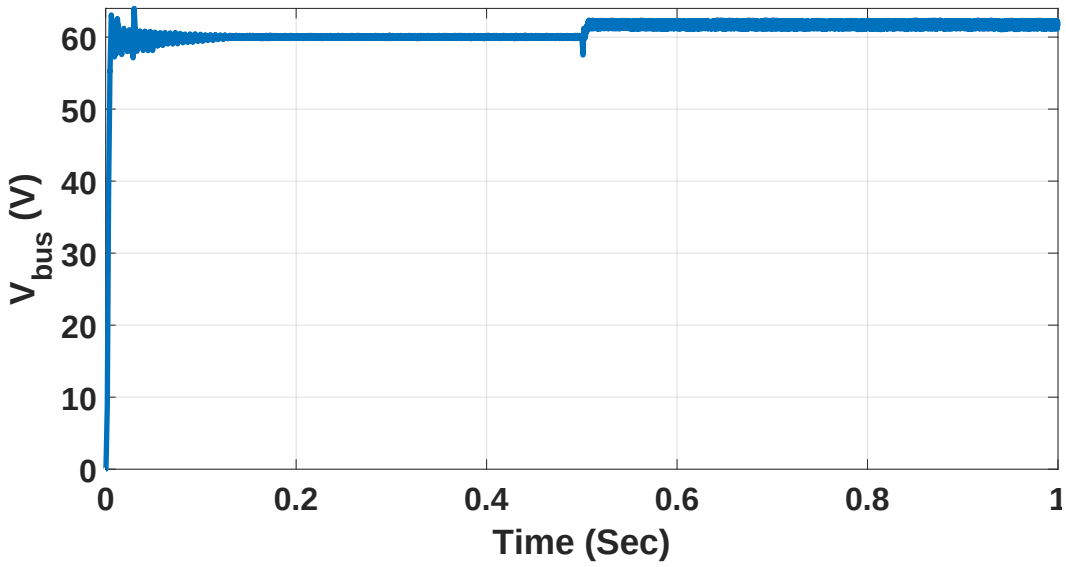

Figure 5.9: Regulation of bus voltage by both PV and battery controller for dynamic irradiance change

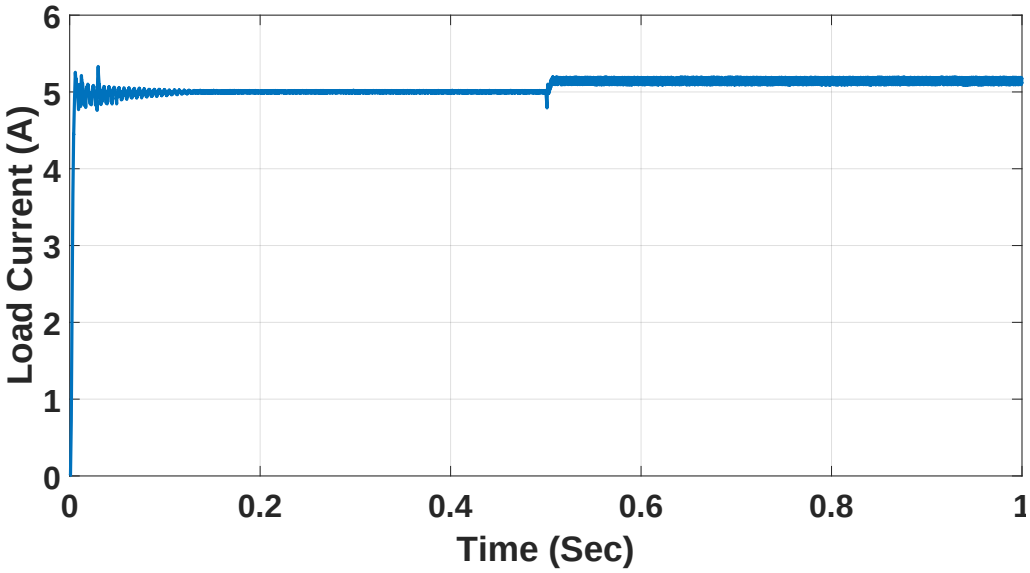

Figure 5.10: Constant load current for dynamic irradiance change

at 60 V and load current being constant at 5 A despite the irradiance changing at 0.5 sec. Fig. 5.16 demonstrates that the pv-based controller is well capable of regulating the DC bus voltage in the absence of a battery by curtailing the PV power and making it constant around the load requirement. Fig. 5.17 illustrates

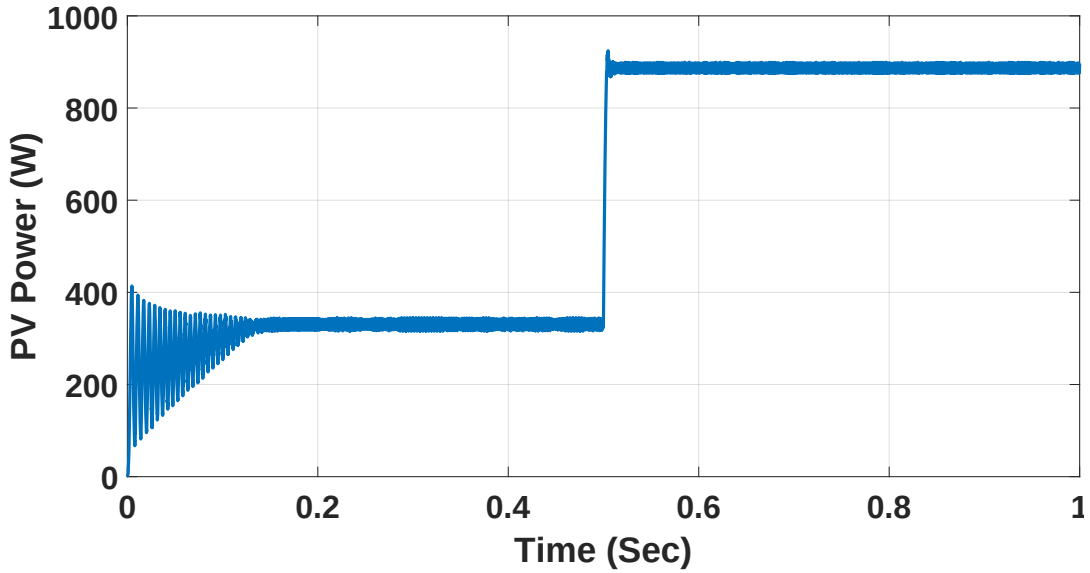

Figure 5.11: Maximum power extraction by PV-controller for dynamic irradiance

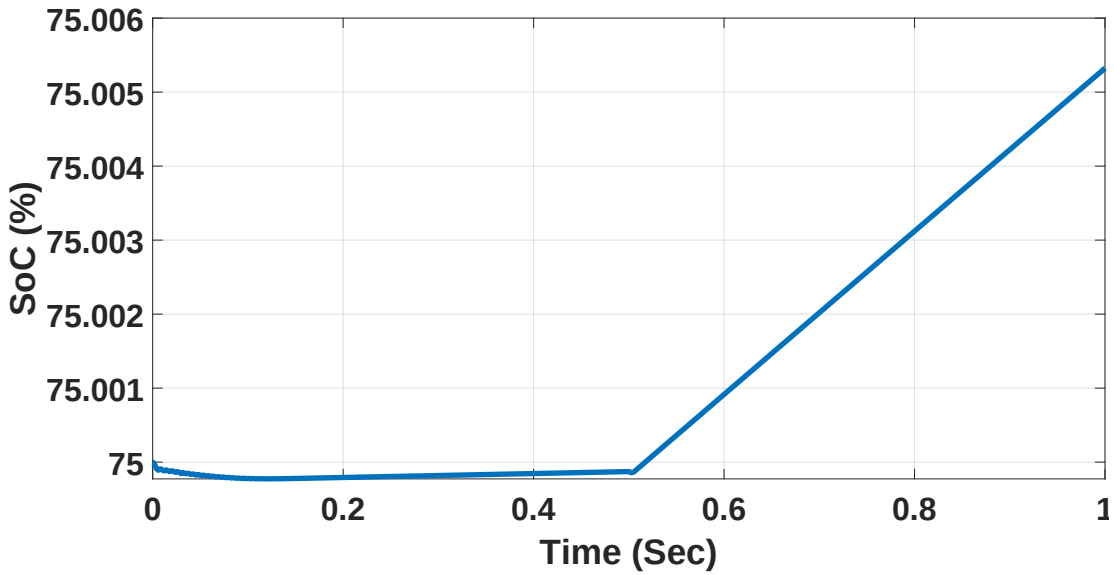

Figure 5.12: Battery state of charge (SoC) for dynamic irradiance change

that the battery current remains at zero during that entire period which confirms the effectiveness of the PV-based controller.

CASE III: In this scenario, a step load change is applied in addition to the step irradiance change in order to test the robustness of the PV-based controller. Fig. 5.18 shows the step change of load from 12 Ω to 20 Ω at 0.3 sec and the results are

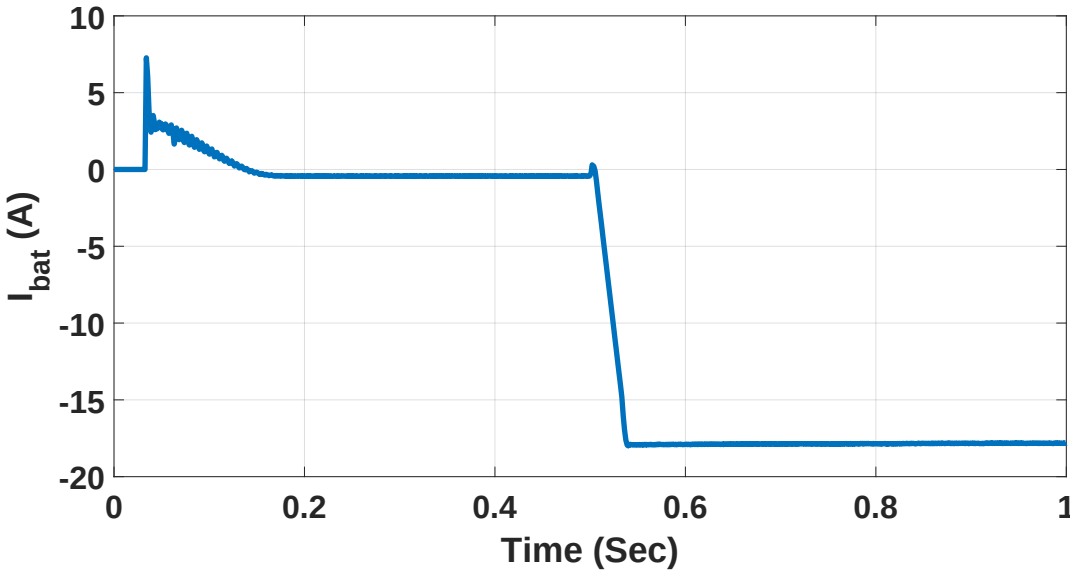

Figure 5.13: Battery charging and discharging current for dynamic irradiance change

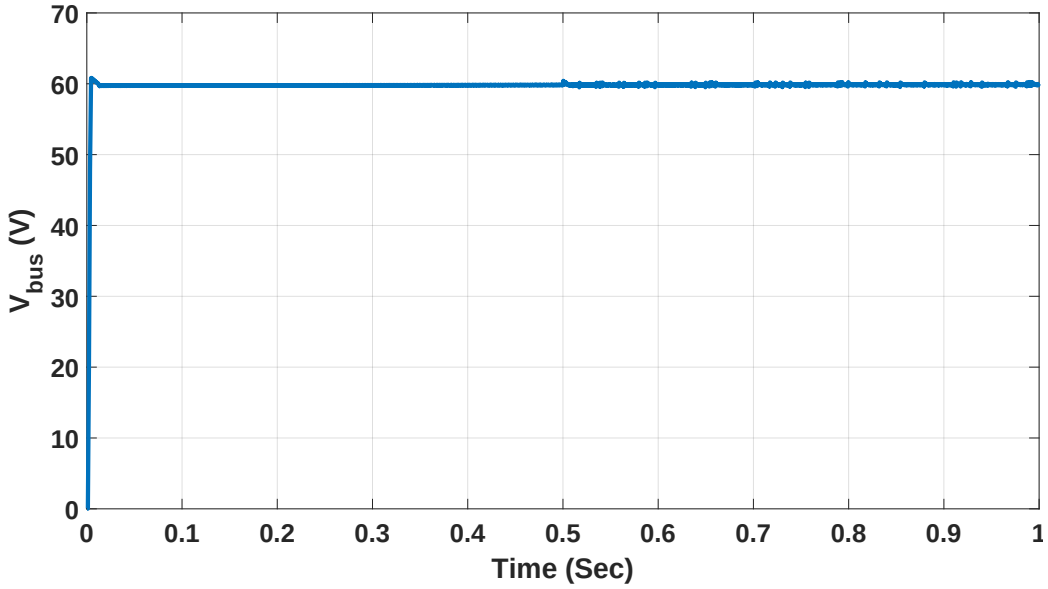

Figure 5.14: Bus voltage regulation PV-based controller

shown in Fig. 5.19 and Fig. 5.20. As it can be seen from those figures, the DC bus voltage remains mostly constant at 60 V and the load current remains constant at 5 A for 12 Ω resistor until 0.3 sec and changes to 3 A when the load resistance changes to 20 Ω.

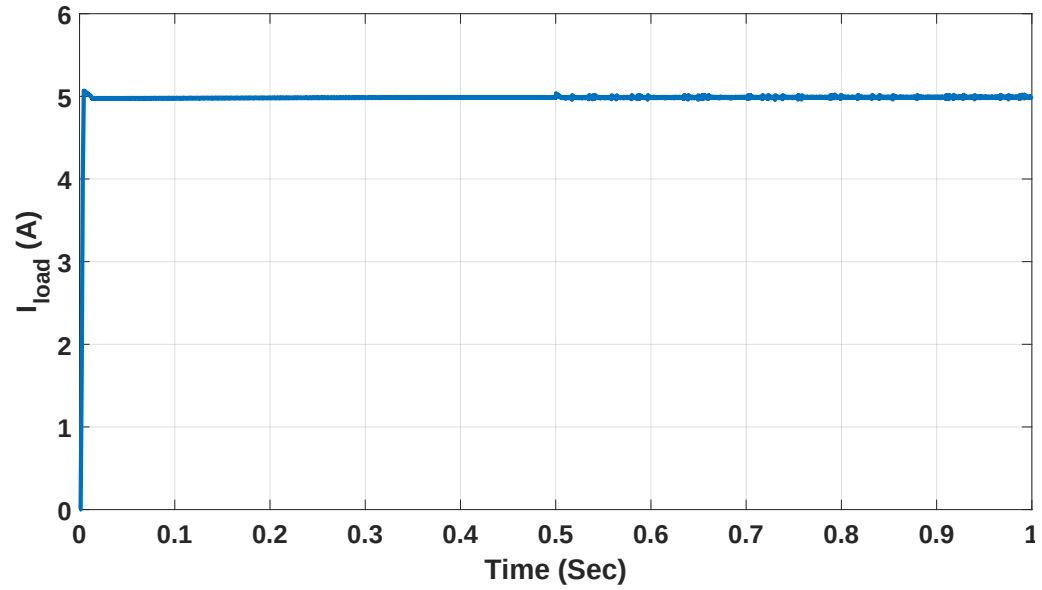

Figure 5.15: Load current using PV-based controller

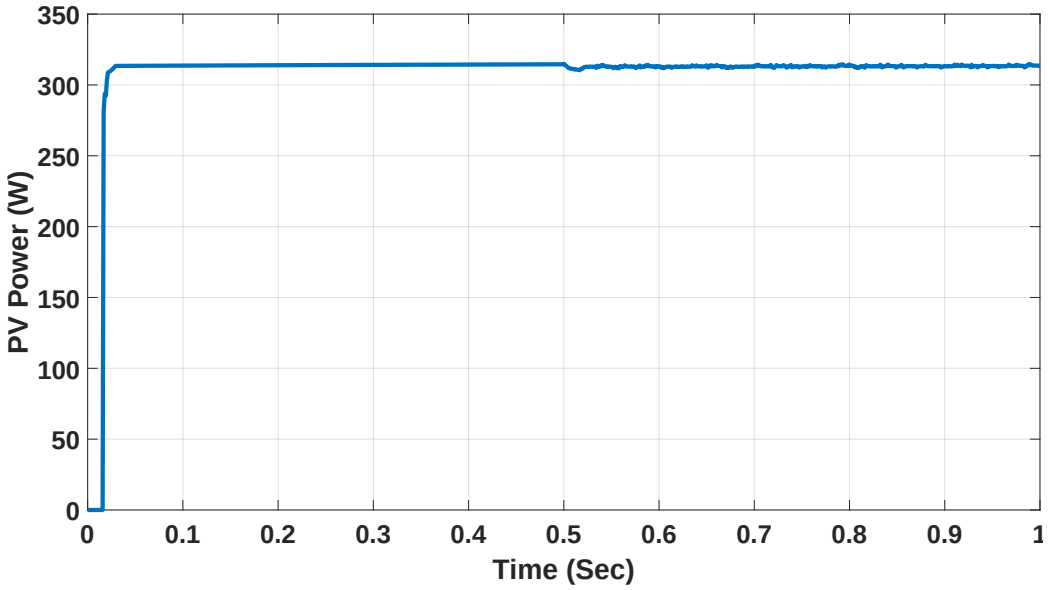

Figure 5.16: PV power regulation by PV-based controller

5.3 Summary

An islanded DC microgrid where the PV and battery are incorporated, is studied in this chapter. Three different controllers: the maximum power point controller, the battery energy source controller, and the proposed PV-based voltage regulation con-

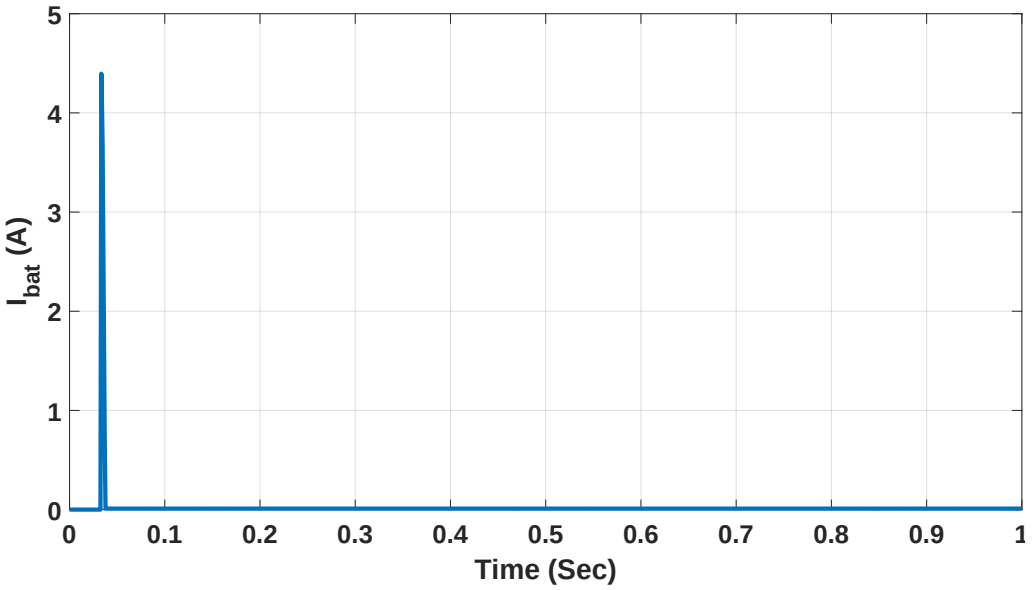

Figure 5.17: Zero current injection by battery because of PV-based controller

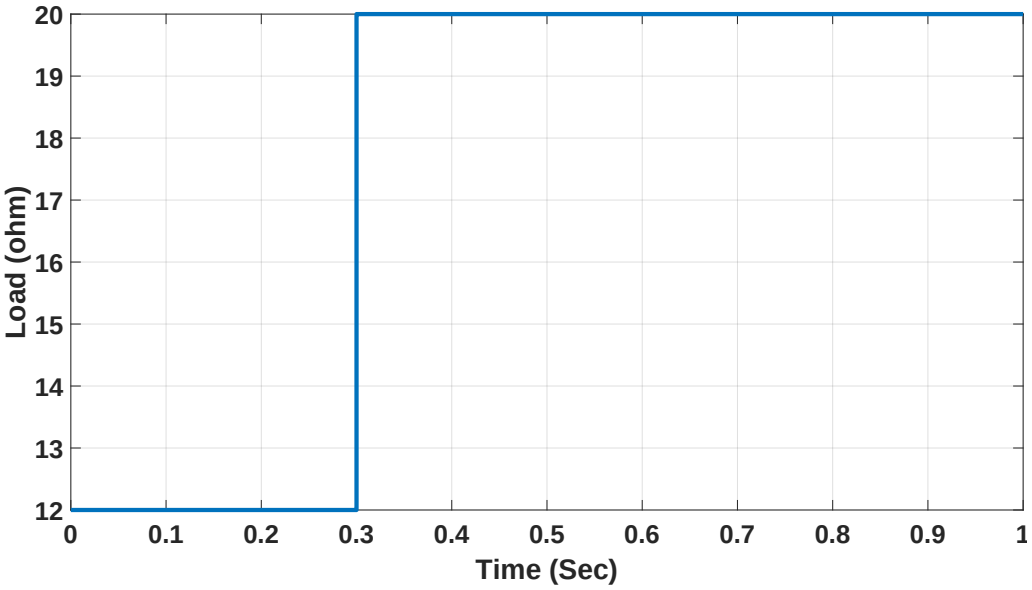

Figure 5.18: Step change of load from 12 ohm to 20 ohm at 0.3 sec

troller are used to check whether they can regulate the DC bus voltage at the desired value. Dynamic irradiance and load step change are adopted in order to examine the proposed PV-based controller's ability to regulate the DC bus voltage when PV power goes higher than load power in the absence of a battery - that reduces the

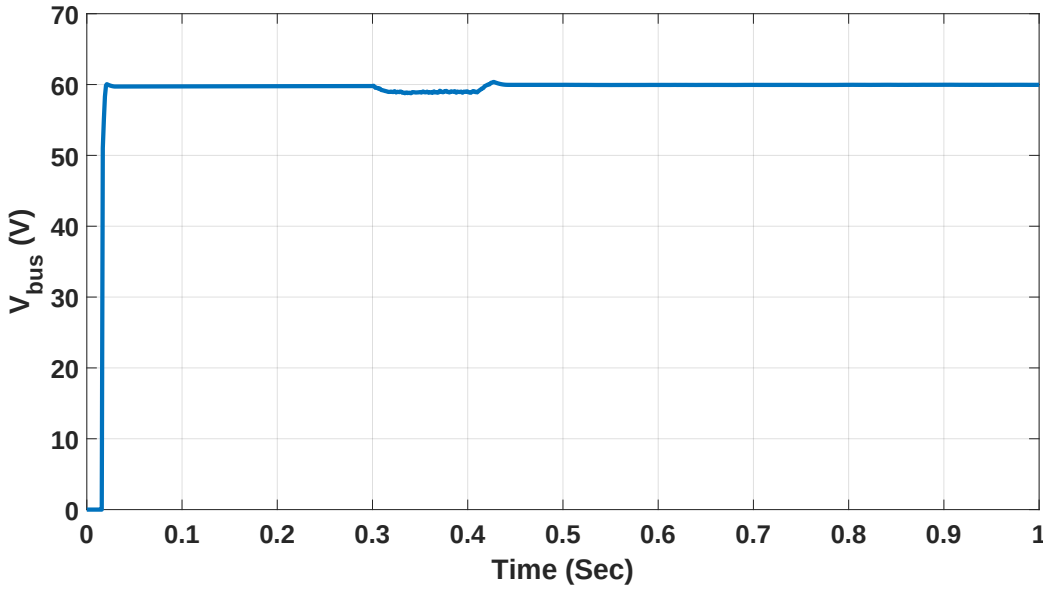

Figure 5.19: Voltage regulation by PV-based controller with step load change and step irradiance change

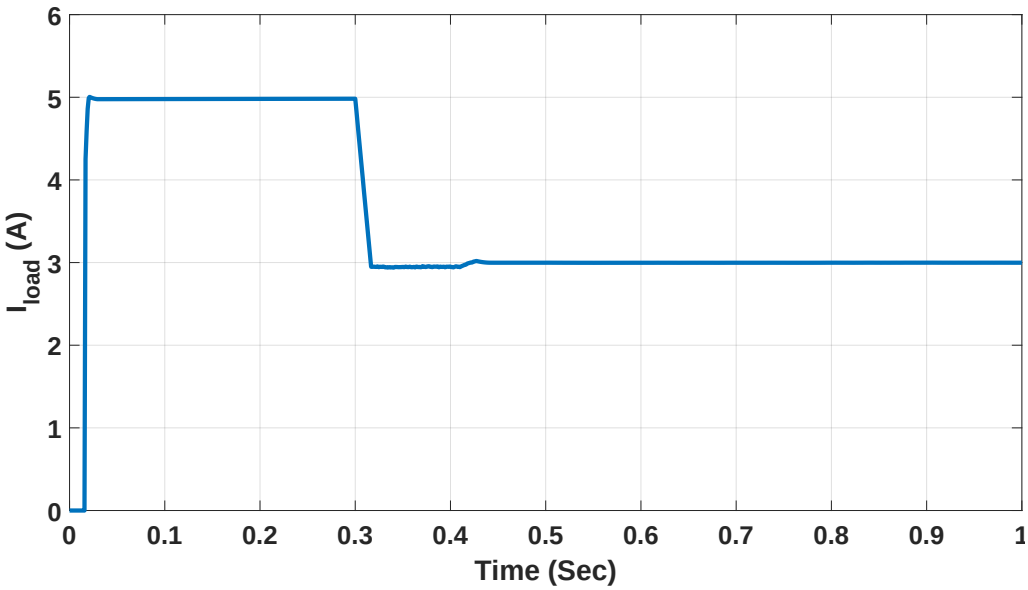

Figure 5.20: Change of current because of step change of load

over-charging stress on the battery. Simulation results verify the effectiveness and robustness of the controllers.

CHAPTER 6

A UNIFIED CONTROLLER FOR HYBRID PV-BATTERY SYSTEM WITH DC MICROGRID VOLTAGE REGULATION IN GRID-CONNECTED AND ISLANDING-MODE

This chapter proposes a unified controller to combine the maximum power point (MPP) tracking and voltage regulation (VR) by using a single control signal. It utilizes an ANN-based predictor to predict the voltage corresponding to MPP to perform the unification. The chapter is structured as follows: Section 6.1 illustrates the complete control configuration with proposed control strategy, section 7.2 describes the simulation results with detailed analysis and verification of the proposed controller and section 7.3 provides the summary of the chapter.

6.1 Proposed Control Strategy

The control strategy can be divided into two main parts: i) PV-side control with the boost converter for injecting maximum power during grid-connected and battery-connected mode and, voltage regulation during islanding mode or load-following mode, ii) Voltage regulation by Battery Energy Storage System (BESS). A detailed description of these two modes is provided below:

6.1.1 PV controller with the Boost Converter

The conceptual development of the controller is illustrated in Fig. 6.2. The controller starts by taking the difference between desired reference voltage which is considered 48 V (there are different dc voltage levels are generally considered, here 48 V is taken for this research because most of the LV dc distribution systems and telecommunication industries use 48 V.), and the bus voltage from the DC-link ca-

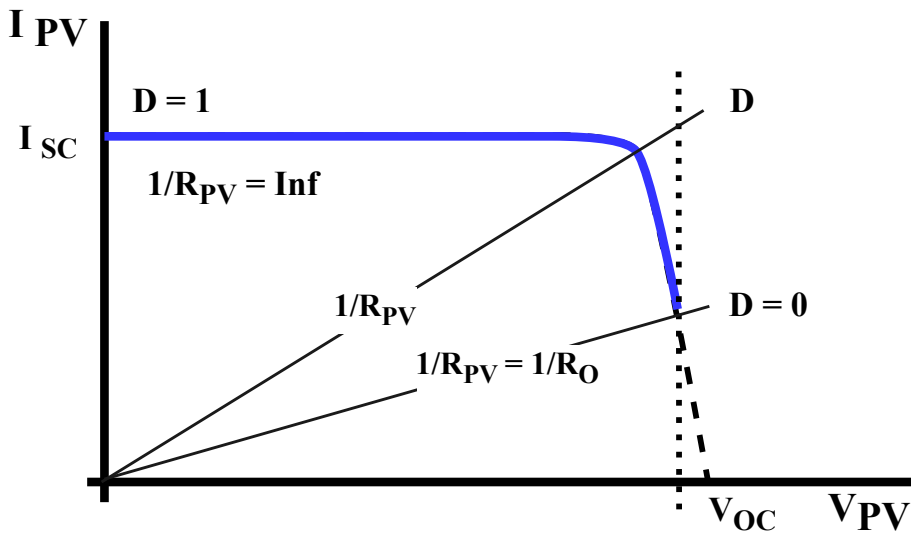

Figure 6.1: Load access region by Boost Converter

pacitor. This difference is the error which could be either positive if the V_{ref} is higher than V_{BUS} or negative when V_{ref} is lower than V_{BUS}. The error is then fed into the 'Error to Voltage' block, where it generates a control signal, V_C. The minimum value of V_C is zero, and the maximum value is $(V_{OC} - V_{MPP})$, where V_{OC} is the open-circuit voltage of the PV module and V_{MPP} is the voltage associated with MPP. The control signals V_C are then added to V_{MPP} to generate the desired reference signal, V_T. The error between the control signal, V_T, and V_{PV} is then fed into the control signal generator. The control signal generator then increases or decreases the duty signal based on the polarity of the error signal.

As we can see, if the duty cycle increases V_{PV} decreases. Therefore, if the error is positive, the control algorithm increases the duty signal, which will increase the PV voltage,i.e., shift the operating point towards the right side - which will reduce the error. However, if the error is negative, the algorithm decreases the duty signal to drag the operating point toward the reference control signal.

It is important to realize that load resistance, R_o can vary only for a particular region on the I – V curve of the PV module when a boost converter is being used.

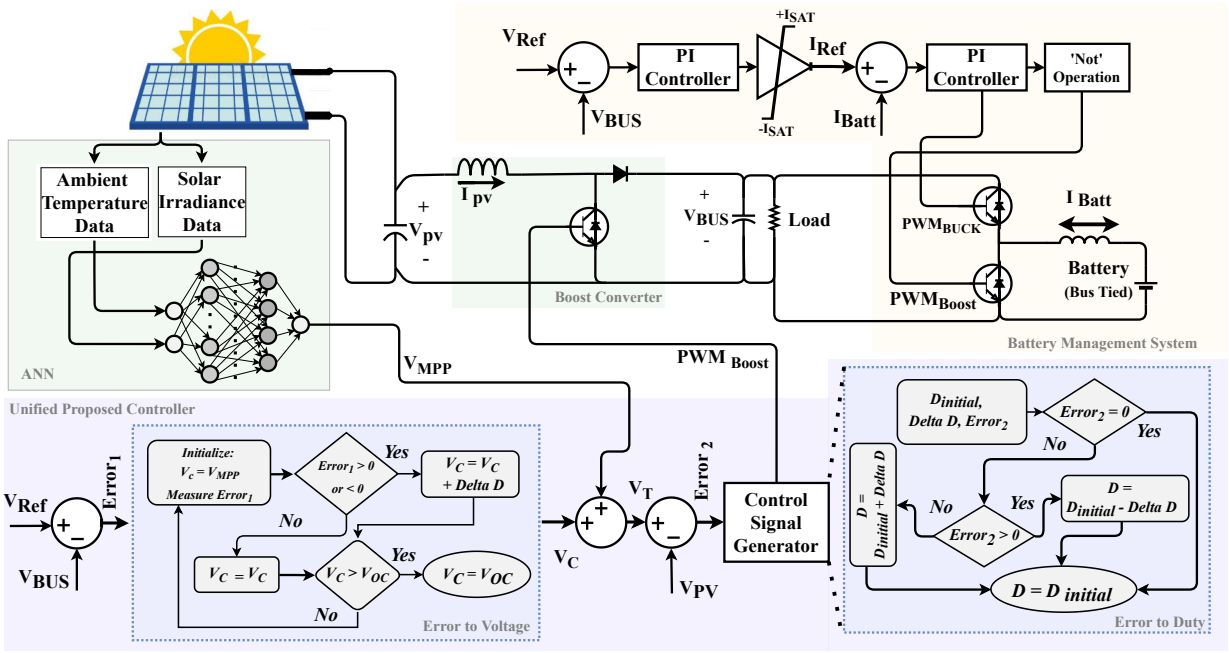

Figure 6.2: Proposed unified control strategy

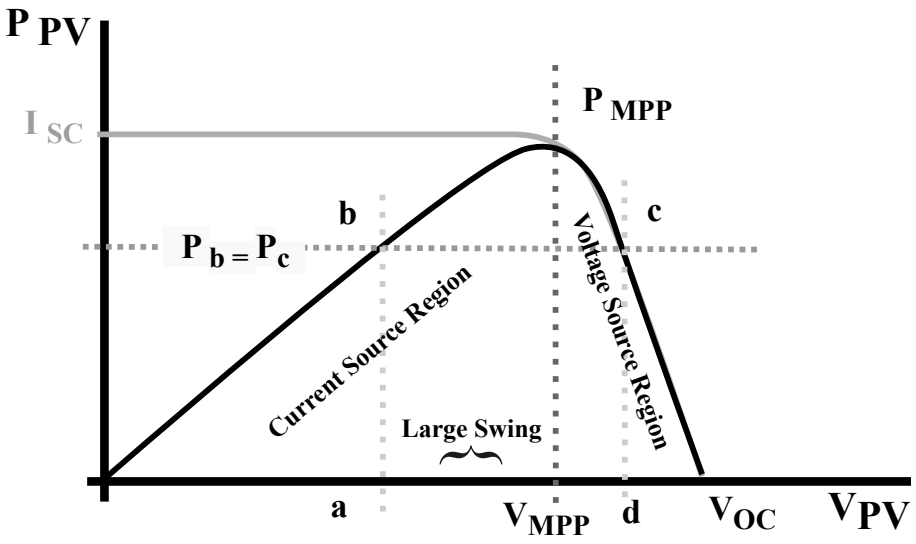

Figure 6.3: Equal power at Left side and Right side of MPP

As illustrated in Fig. 6.1, the load only can be varied only for the blue portion on the $I-V$ curve while varying the full swing of duty signal. The $eq(1)$ to $eq(5)$ supports the claim mentioned above.

$$V_o = V_{PV} * \frac{1}{1-D} \tag{6.1}$$

$$V_{PV} = V_o - V_o * D \tag{6.2}$$

$$I_o = I_{PV} * (1-D) \tag{6.3}$$

$$R_o = \frac{V_o}{I_o} = \frac{R_{PV}}{(1-D)^2} \tag{6.4}$$

$$R_{PV} = R_o * (1-D)^2 \tag{6.5}$$

During the grid-connected mode, the bulk grid controllers will generate the set-points for the DC-link voltage at the desired level; therefore, the error between V_{Ref} and V_{BUS} will be almost zero - that will make the value of the control signal,V_C to be very close to zero, subsequently V_T will be very close to V_{MPP} - which will ensure maximum power injection to the grid during the grid-connected mode. However, when the grid is not present during the islanding mode, PV and BESS- controllers are solely responsible for regulating the DC bus voltage around the desired voltage reference. So, when the PV is operating at the MPP, and the load is required less than MP generated from PV, and the battery state of charge is close to SoC^{max}, then the operating point of PV is required to be shifted from MPP to the right or left side of MPP in order to curtail the extra power-that will ensure demand side

and generation side equalization. The left-hand side of MPP can be considered as a current source of the P vs. V curve, and the right-hand side of MPP can be considered as a voltage source as shown in Fig. 6.3 because the current remains almost constant on the left side, and voltage changes very narrowly on the right side of MPP. Because of that reason, if the operating point is shifted to the left side, there will be oscillations due to voltage variations. That is why the minimum value of V_C is intentionally made zero to prevent the operating point from going towards the left region of MPP. So, V_C could be either zero for grid-connected mode or BESS-charging mode and only positive for voltage regulation mode. The inaccessibility of the left side of the MPP region does not reduce any degrees of freedom since the power delivery at any operating point on the right side of MPP is exactly equal to power at the left side operating points, as shown in Fig. 6.3. The shifting of the operating point towards the right side of MPP benefits from fewer oscillations. The V_{MPP} voltage is generated from an artificial neural network (ANN) based MPPT based on weather parameters: irradiance and temperature. The description of the ANN-based controller is out of the scope of this paper. It is important to emphasize that control signal V_C and V_{MPP} are combined together to generate a unified control signal V_T as shown in Fig. 6.2. If V_{Ref} and V_{BUS} are equal, then V_C will generate zero, which will eventually make V_T equal to V_{MPP} and MPP will be generated by the controller. V_{Ref} and V_{BUS} will get closer to each one if the system works in either grid-connected or battery-connected charging mode. However, during the islanding mode, when PV power is greater than load power and the battery is fully charged, V_T will be only higher than V_{MPP}-that will ensure power curtailment of PV to run the system in stable mode.

6.1.2 Battery Controller for Buck-Boost Converter

The bi-directional buck-boost converter is designed to charge and discharge the battery in order to regulate the voltage across the DC bus. The power flow from $V_{bus} = 48V$ to $V_{bat} = 24V$ is maintained through the buck topology of the converter, and V_{bat} to V_{bus} power flow is supported by the boost topology. The Battery Management System is shown in Fig. 6.2, sends the appropriate signals to drive the MOSFETs named as PWM_{BUCK}, PWM_{BOOST} and maintains the coordination between them in switching from buck mode to boost mode and vice-versa [95]. In order to implement the above operation, the battery controller utilizes two cascaded PI controllers, as shown in Fig. 6.2.

The outer voltage control loop is used to regulate the V_{BUS} to V_{Ref} and generates the reference signal for the inner current control loop. There is also a saturation block to prevent the battery-current reference from going beyond the battery's rated charging and discharging current. The inner current control loop then regulates the battery current towards the reference signal. The modeling of the voltage and current controller dynamics is expressed in (6.6) and (6.7) respectively.

$$I_{Ref} = K_p^v(V_{Ref} - V_{BUS}) + K_i^v \int_0^t (V_{Ref} - V_{BUS})dt \tag{6.6}$$

$$u(t) = K_p^i(I_{Ref} - I_{Batt}) + K_i^i \int_0^t (I_{Ref} - I_{Batt})dt \tag{6.7}$$

Here, K_p^v and K_i^v are the proportional and integral control parameters for the voltage controller whereas K_p^i and K_i^i are the proportional and integral control parameters for the current controller and $u(t)$ is the desired control signal.

The control parameters for the cascaded PI controllers are then optimized using the following objective function, and constraints using particle swarm optimization technique [96].

$$ISTSE = \int_0^\infty t^2 e^2(t) dt \tag{6.8}$$

Where: $e(t) = V_{ref} - V_{out}$

The integral of Square Time-weighted Squared Error (ISTSE) will help reduce the settling time and steady-state errors since it squares the time.

Objective Function:

$$J = min \left| \int_0^\infty t^2 e^2(t) dt) \right| \tag{6.9}$$

Subject to:

$$\begin{cases} K_p^{min} \leq K_p \leq K_p^{max} \\ K_i^{min} \leq K_i \leq K_i^{max} \end{cases} \tag{6.10}$$

6.2 Results and Discussion

In this section, the simulation graphs are generated to validate the overall system's performance. Three cases are discussed on the basis of the following electrical parameters of the PV panel:

Number of Series-connected modules per string = 1

Number of Parallel strings = 5

Maximum Power, P_{MPP} = 214.963 W

Open Circuit Voltage, V_{OC} = 36.0 V

Short-Circuit Current, I_{SC} = 7.73 A

Voltage at maximum power point, V_{MPP} = 28.7 V

Voltage at $200W/m^2$ irradiance = 28.25 V

Current at $200W/m^2$ irradiance = 7.44 A

Voltage at $500W/m^2$ irradiance = 28.86 V

Current at $500W/m^2$ irradiance = 18.76 A

Case-1: (Regulation only by PV): In the first case, the performance of the proposed controller is tested when the battery is fully charged while irradiance is kept at $500W/m^2$ and load resistance is kept at 24Ω. Fig. 6.4, Fig. 6.5 and Fig. 6.6 is associated with case-1 where the PV-side controller regulates the DC-bus voltage without taking help from the battery-side controller.

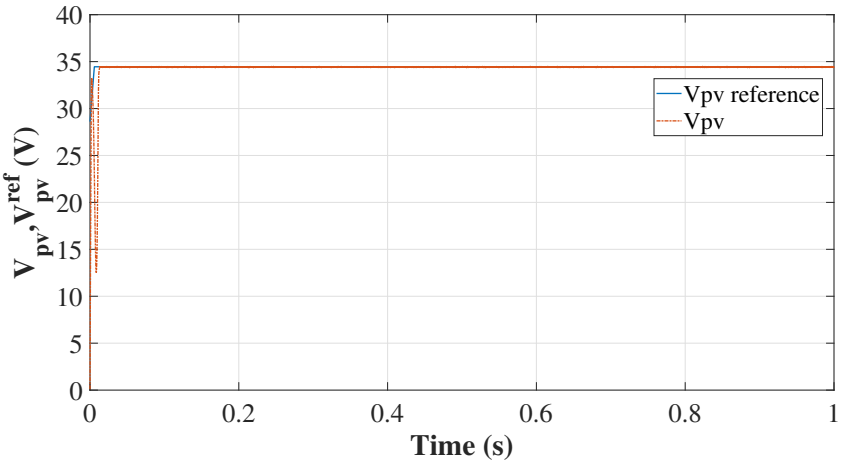

Figure 6.4: Reference generation and PV operating point

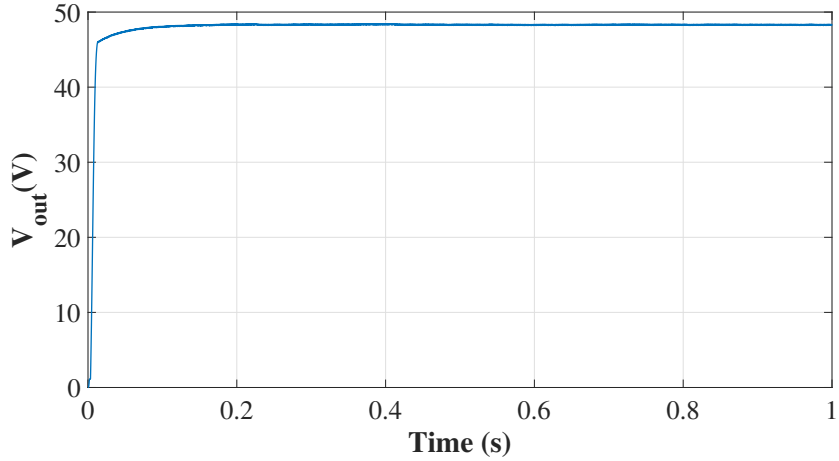

Figure 6.5: DC Bus voltage with PV-side controller

It can be seen from those figures that the output voltage is well regulated at 48 V through the irradiance of $500W/m^2$ would create much higher power than

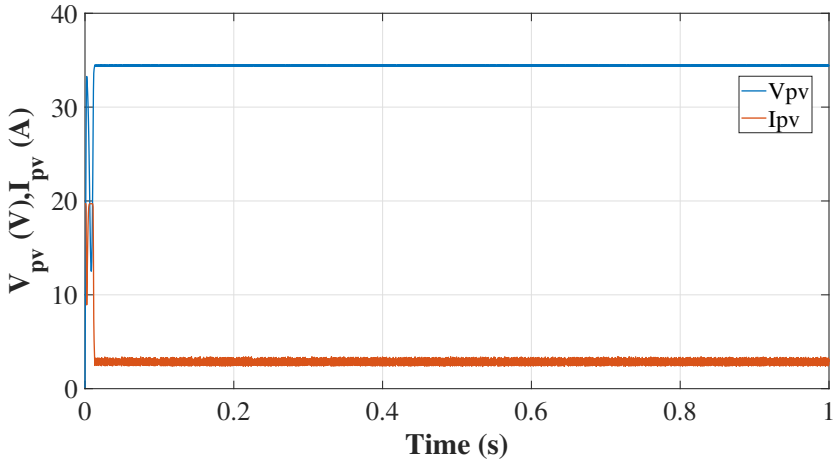

Figure 6.6: Operating point of PV array

the load required. The PV-side controller regulates the voltage by curtailing the PV power - it does so by drifting the operating point towards the right side of MPP, consequently extracting reduced power from PV. Fig. 6.6 verifies that - the operating point is moved a little below than 35 V; accordingly the PV current also moves to about 3 A. Referring to Fig. 6.2, the control signal V_C contains a positive value and gets added with V_{MPP} to generate V_T which is about 34 V corresponding to reduced power than MPP.

Case-2: (Regulation by PV and Battery with step change of irradiance): In this scenario, the performance of the proposed controller is tested with the battery connected while irradiance has a step change at $1sec$ from $500W/m^2$ to $200W/m^2$ and load resistance of 6Ω. A step-change irradiance of $500W/m^2$ to $200W/m^2$ is applied at 1 sec while the Battery is connected. As it can be seen from Fig. 6.7, the output voltage is regulated at 48 V despite the irradiance reduction occurring at 1 sec.

Before the step-change occurred, the Battery was being charged by the surplus of PV power. After 1 sec, however, the battery SOC starts decreasing, as shown in

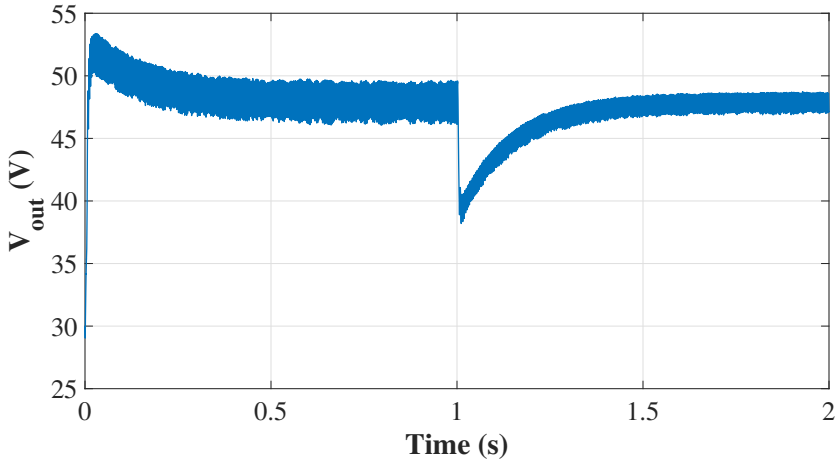

Figure 6.7: DC-link Bus voltage when step change of irradiance occurs

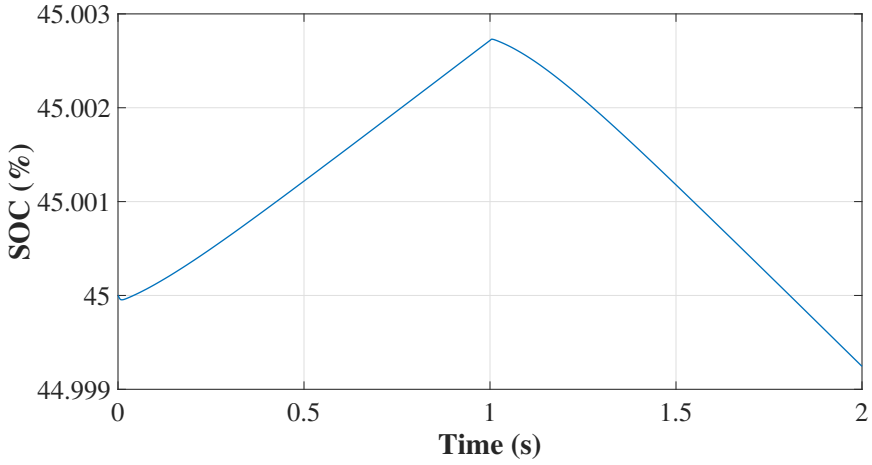

Figure 6.8: Battery State of Charge while irradiance has step change

Fig. 6.8, since PV power was not sufficient to drive the load at $200W/m^2$ irradiance. Similar behavior is observed from battery terminal voltage and current as depicted in Fig. 6.9 and Fig. 6.10 respectively.

It is important to notice that the PV operating point remains at the maximum power point at both irradiances: $500W/m^2$ and $200W/m^2$ as shown in Fig. 6.11 during the battery being operational - that confirms the control logic works properly. As mentioned, the battery is responsible for voltage regulation in this mode by

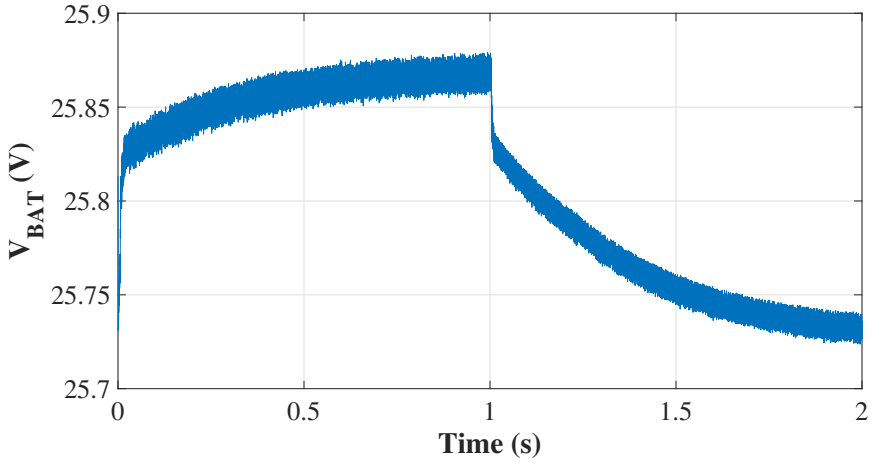

Figure 6.9: Battery voltage while irradiance has step change

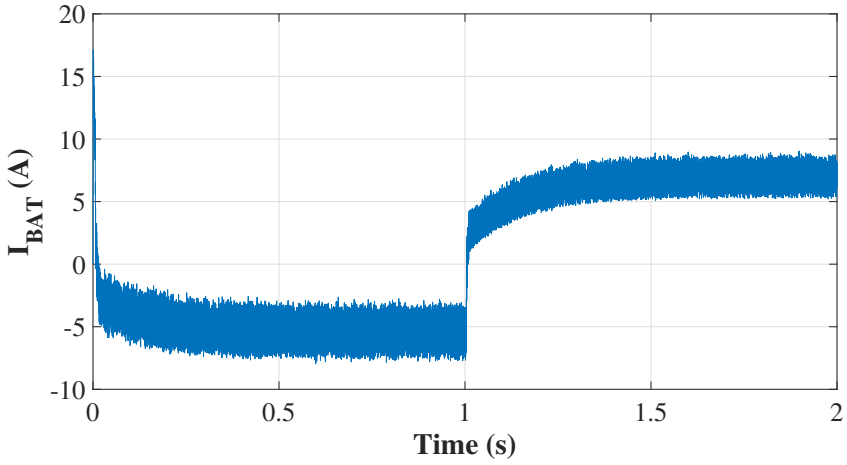

Figure 6.10: Charging and Discharging current of Battery when irradiance has step change

charging and discharging to maintain the generation-demand equalization while PV is operating in MPP mode.

Case-3: (Regulation by PV and Battery with step change of load) In this last scenario, the performance of the proposed controller is tested with the battery connected while irradiance is kept at $500W/m^2$ and step load resistance at $1sec$ from 24Ω to 12Ω. A step load change is applied while the irradiance is kept constant at $500W/m^2$. As it can be seen from Fig. 6.13, the DC bus voltage is regulated at 48

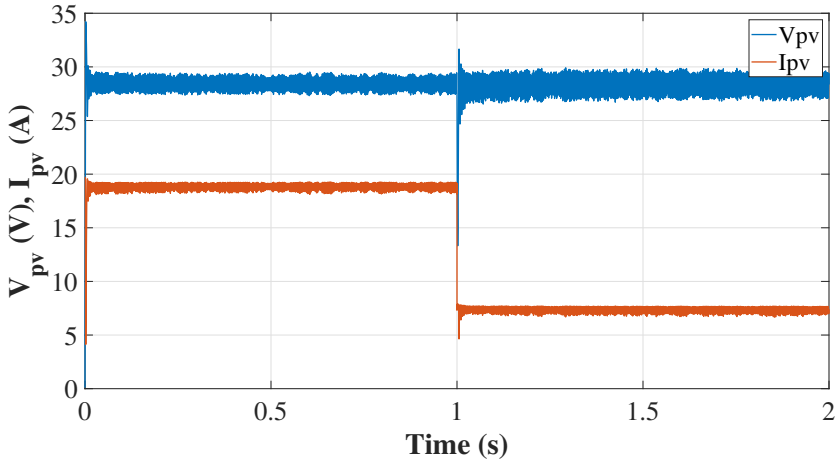

Figure 6.11: Voltage and current operating points of PV array for step change occurs in irradiance

V with little transients while the current changes accordingly. Fig. 6.12 illustrates the response of SOC while the step load change occurs at 1 sec. Since the load requires more current, changing from 24Ω to 12Ω, the SOC of the battery changes after 1 sec - accordingly, the voltage and charging-discharging current of the battery follows the same logic as depicted in Fig. 6.15 and Fig. 6.14.

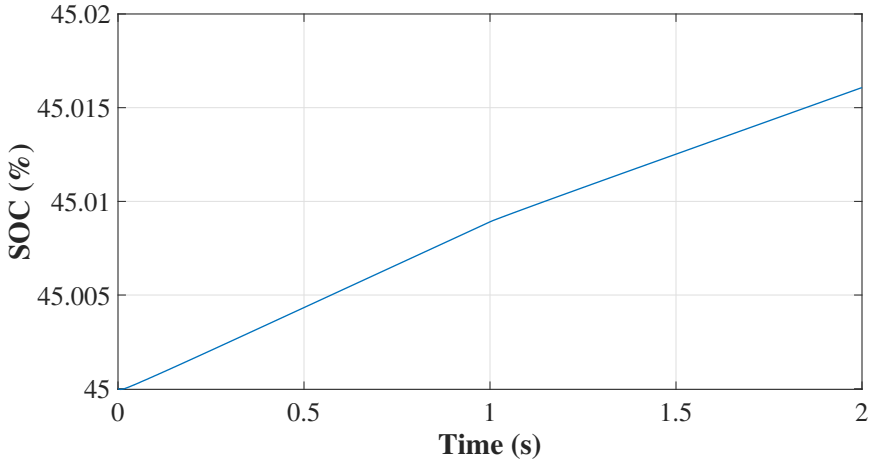

Figure 6.12: Change of State of Charge when step change of load occurs

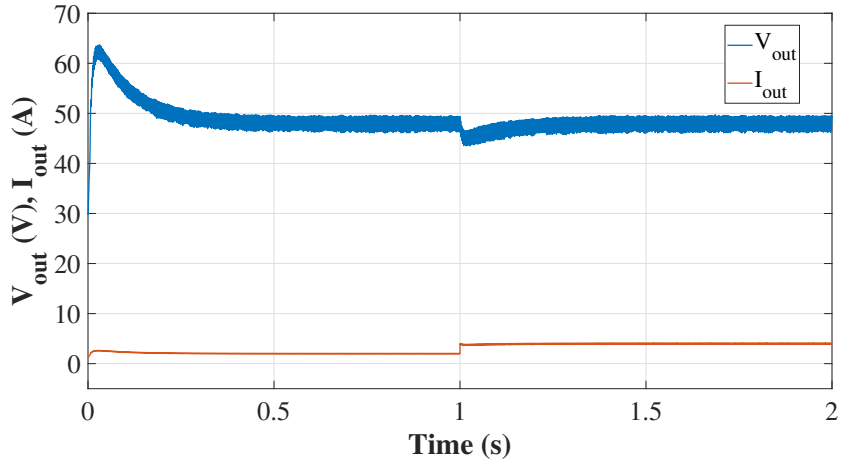

Figure 6.13: Output voltage and current when step change of load occurs

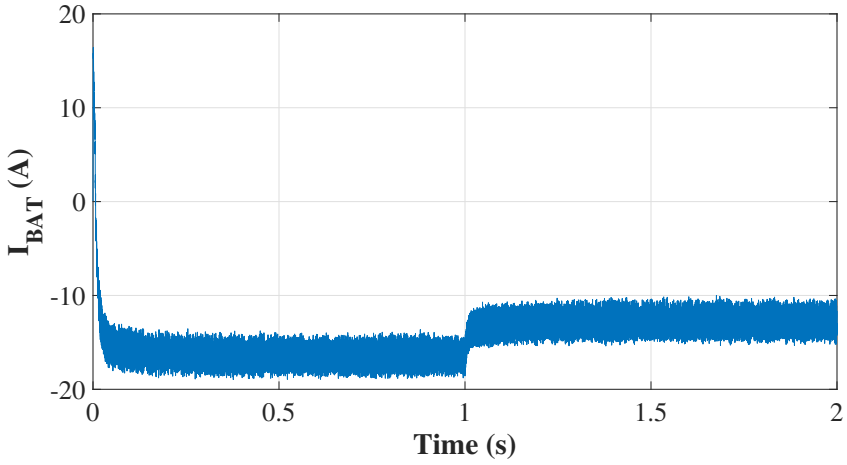

Figure 6.14: Battery current while step change of load occurs

6.3 Summary

This chapter discussed developing a simple unified controller which regulates the DC-link capacitor voltage at the desired voltage level of 48 V regardless of input side variations due to irradiance and output side variations due to load changes. The controller injects MPP during battery charging mode by making the total control reference signal to be equal to MPP voltage and curtails PV power by dragging the operating point towards the right side of MPP during the islanding mode if the load

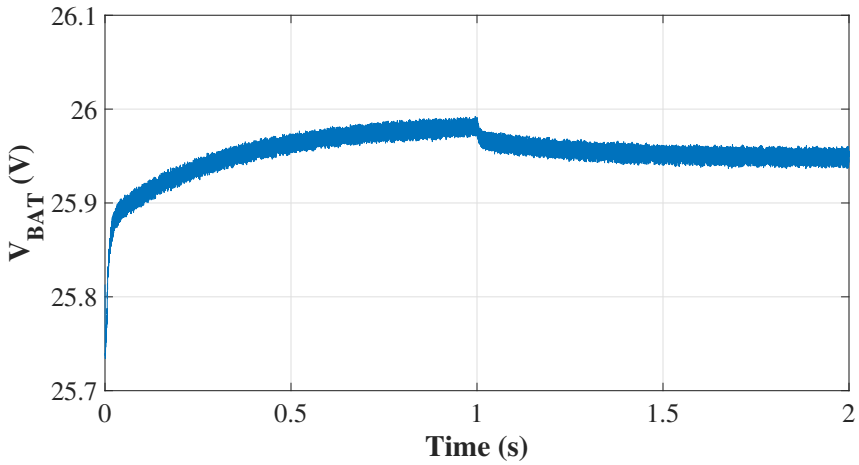

Figure 6.15: Battery voltage while step change of load occurs

power requirement is less than PV power. Thus, the unified control signal decides which mode: MPPT or voltage regulation- will be carried out. If the collective control signal reference is higher than the voltage associated with MP, the controller works in voltage regulation mode, and if the control signal generates voltage reference close to MPP voltage, then the controller works in MPPT mode - simulation results also justified that logic.

CHAPTER 7

ANN-BASED DYNAMIC FREQUENCY REGULATION OF PV-BASED HYBRID MICROGRID SYSTEM

This chapter proposes a virtual inertia (VI) and artificial neural network (ANN) based control strategy to provide faster frequency regulation for a PV-Synchronous Generator based microgrid. The chapter is organized as follows: Section 9.1 provides the detailed control structure and methodology of the proposed control algorithm with the microgrid system, section 7.2 illustrates the simulation results for the verification of the proposed control strategy and section 7.3 provides the summary of the chapter.

7.1 Proposed VI-ANN controller in Microgrid

The combination of VI for reference power generation and the use of ANN to determine the operating point of the PV is subsequently called the VI-ANN controller in this paper. The proposed VI-ANN controller is implemented in a microgrid setup that consists of PV and a synchronous generator connected at the Point of Common Coupling (PCC). The whole system is as shown in Fig. 7.1. The PV is coupled with the synchronous generator through a two-stage 'buck converter-inverter' power conditioning system. Unlike most of the state-of-the-art research where attempts have been made to inject active power at the inverter side, the proposed VI-ANN controller is implemented at the buck-converter side which helps reduce the complexity of the whole system's control. The implementation of the VI-ANN controller at the converter side also allows the inverter to only regulate the DC bus voltage and the reactive power.

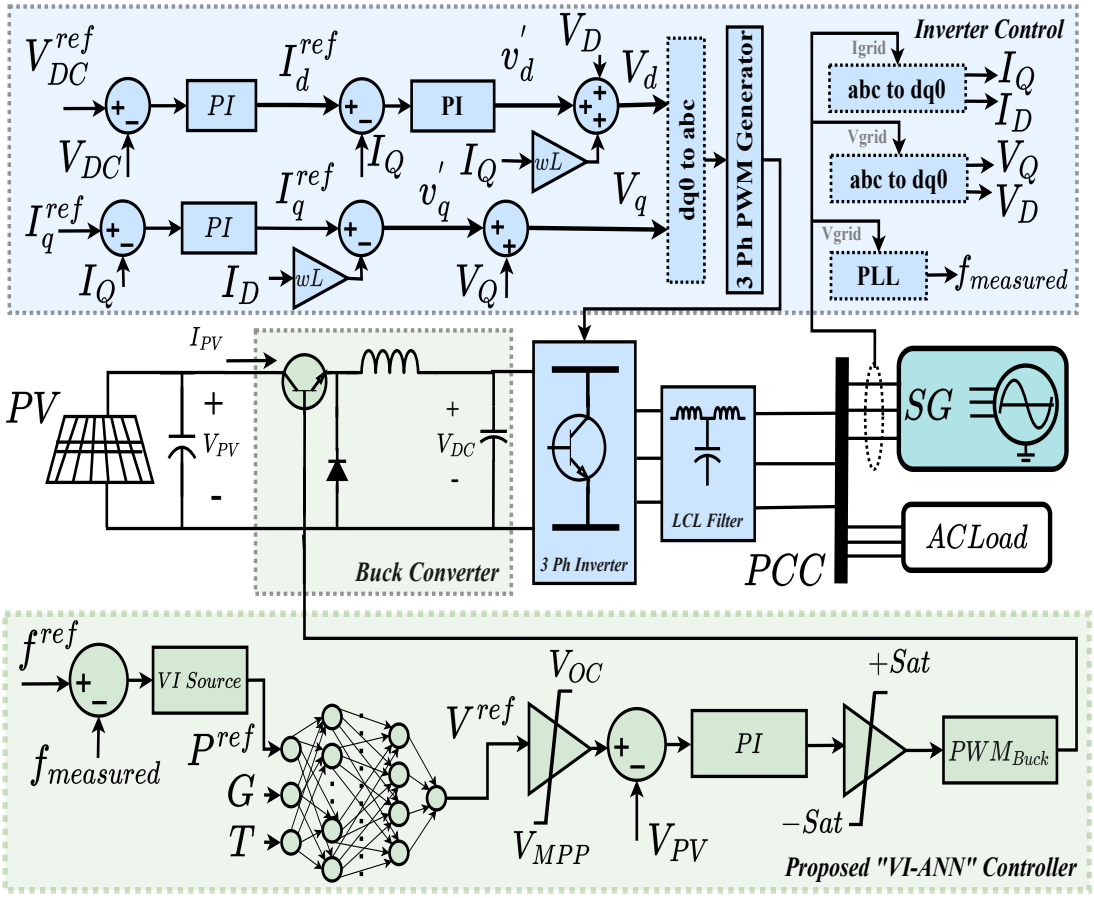

Figure 7.1: Implementation of proposed ANN-Controller in Microgrid set-up

7.1.1 VI-based P^{ref} estimation and ANN-based V^{ref} model

Based on the proposed approach, the VI is emulated by controlling the active power reference on the PV-side buck converter.

The VI power reference, P^{ref}, is generated and fed to the ANN's $P^{ref} \rightarrow V^{ref}$ model based on Eq. (7.1): [97]

$$P^{ref} = P_o + K_I \frac{d(\Delta f)}{dt} + K_D(\Delta f) \tag{7.1}$$

Here, P_o denotes the primary power from PV-array, Δf denotes the error between nominal frequency and measured frequency ,$\frac{d\Delta f}{dt}$ denotes the Rate Of Change Of Frequency (ROCOF) measured at the PCC, K_I denotes the VI coefficient. K_I

along with ROCOF signifies that power will increase or decrease by shifting the operating point by the VI source (in this case the PV) according to a positive or negative ROCOF. This second term will be non-zero during transient disturbance periods of power exchange, after which this term will be zero. K_D denotes the virtual damping coefficient, which suppresses frequency oscillations. The third term of Eq. (7.1) represents frequency droop, which is added to maintain the system frequency closer to the nominal frequency value. The steady-state frequency error will be taken care of by a secondary controller, or the Automatic Generation Controller (AGC) of the synchronous generator, however is not within the scope of this research study which focuses on primary frequency support.

As mentioned above, the VI source block, as depicted in Fig. 7.1, generates the P^{ref} based on the error calculated between the nominal system frequency and the measured frequency by a Phase-Locked-Loop (PLL) at the PCC. The generated P^{ref} is then given as an input, along with irradiance (G) and temperature (T), to the ANN model to generate the desired voltage reference, V^{ref}. A PI controller whose parameters are optimized with the process described in [96] is then used to drive the operating point of PV towards the generated V^{ref} by the ANN controller. This is accomplished by the PI controller generating a desired duty cycle value which is converted to a high-frequency Pulse Width Modulation (PWM) switching signal to control the Insulated-Gate Bipolar Transistor (IGBT) of the buck converter. This IGBT in turn controls the PV terminal voltage thereby adjusting active power injection.

7.1.2 Description of the ANN model

The utilized ANN model is a standard feed-forward, fully connected (dense) neural network used for regression. The network is comprised of a single input, hidden, and output layer where the hidden layer consists of 100 processing elements (and a bias) whose outputs are passed through a Rectified Linear (ReLu) activation function. The ANN model predicts a V^{ref} value based on 3 standardized input parameters which are irradiance, temperature, and the VI source-generated P^{ref} value governed by Eq. (7.1).

7.1.3 Control mechanism of Inverter

The conventional inverter control in direct-quadrature (DQ) reference frame as shown in Fig. 7.1 can be described by the following Eqs. (2)-(5) [98]:

$$\begin{aligned}\begin{bmatrix} V_D \\ V_Q \end{bmatrix} =& R_f \begin{bmatrix} I_D \\ I_Q \end{bmatrix} + L_f \frac{d}{dt} \begin{bmatrix} I_D \\ I_Q \end{bmatrix} \\ &+\omega L_f \begin{bmatrix} -I_Q \\ I_D \end{bmatrix} + \begin{bmatrix} V_D \\ V_Q \end{bmatrix}\end{aligned} \tag{7.2}$$

$$\begin{bmatrix} I_D \\ I_Q \end{bmatrix} = \begin{bmatrix} I_D \\ I_Q \end{bmatrix} + C \frac{d}{dt} \begin{bmatrix} V_D \\ V_Q \end{bmatrix} + \omega C \begin{bmatrix} -V_Q \\ V_D \end{bmatrix} \tag{7.3}$$

$$V_{DQ} = R_f I_{DQ} + j\omega L_f I_{DQ} + V_{DQ} \tag{7.4}$$

$$I_{DQ} = I_{DQ} + j\omega C \cdot V_{DQ} \tag{7.5}$$

Here, V_D, V_Q, I_D, V_Q denote voltage and current along D and Q axis, R_f, L_f and C denote filter parameters and ω denote angular frequency of microgrid.

7.2 Results and Discussion

The simulation results are divided into 4 sections. The first section discusses the training part of the ANN model, the second section discusses the frequency regulation comparison with and without PV by the proposed controller. The third and forth section discusses about frequency regulation of the proposed system where a step change in load and a step change in irradiance is applied.

7.2.1 Training of ANN Model

The data was used to train the ANN which was produced by incremental irradiance with a step size of 10 from $800W/m^2$ to $1000W/m^2$ while keeping temperature constant at $25°C$. Each incrementation of irradiance produced a unique P-V curve which was sampled while linearly increasing voltage from the MPP voltage to an ordinary maximum operating voltage. Therefore, this process produced a 4-variable training and validation data set (3 features, irradiance, temperature, and P^{ref}, and 1 target: V^{ref}) for each irradiance step which were then concatenated and shuffled before training. The ANN was trained and tested using k-fold cross validation (where k=5) and produced the following performance metrics: Root-Mean-Square Error (RMSE) = 0.033, R-Squared = 0.99, Mean Squared Error (MSE) = 0.00109, and Mean Absolute Error (MAE) = 0.018872. Fig. 9.7 shows the ANN's predictions plot against the true values which further buttresses the performance metrics listed above.

The simulation results are generated by using the mathematical model depicted in Fig. 7.3 where the color combination of the blocks are similar to Fig. 7.1.

As mentioned earlier, the inverter-control mechanism allows the DC-bus voltage, the output of the buck-converter, to be regulated at the desired set-point which

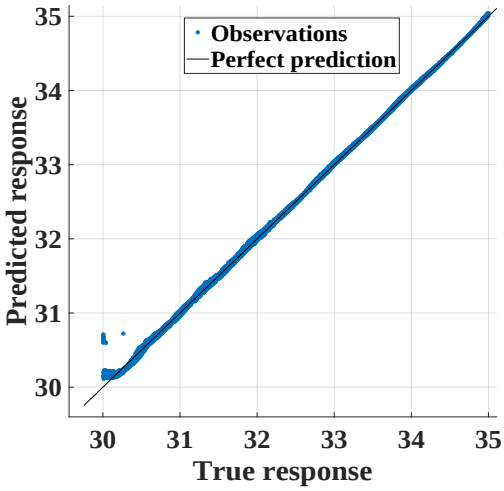

Figure 7.2: True Response vs Predicted Response

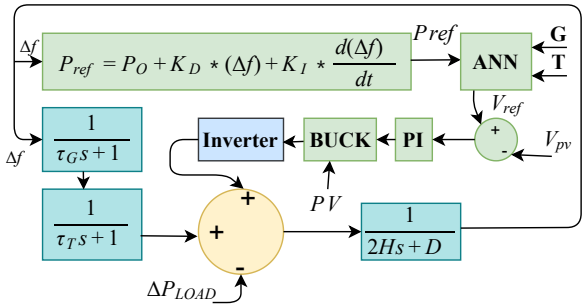

Figure 7.3: Mathematical Model of the system

allows the controlled active power to be injected into the microgrid besides reactive-power control by the inverter. In that regard, in simulation, a constant voltage-source is utilized at the output of the buck-converter that mimics the behaviour of DC-bus regulation aspect of the inverter-control mechanism. Not only that simplifies the overall detailed circuit-diagram by eliminating the high-frequency switching components as shown in Fig. 7.1 but also it expedites the whole simulation process without sacrificing the underlying system-dynamics.

7.2.2 Step Response of Proposed VI-ANN Controller

The PV component of the system is initially disconnected to evaluate the baseline performance of frequency regulation by the synchronous generator only, after which the PV system is connected with the proposed control mechanism. An extra load is of $240W$ is added at the start of the simulation. The result before and after the integration of PV are depicted in Fig. 7.4.

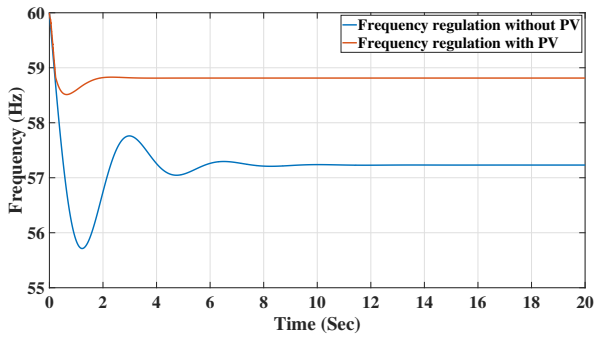

Figure 7.4: Step Response of the System with and without PV

As it can be seen, the frequency nadir reaches about 55.7 Hz when the synchronous generator was solely responsible for frequency regulation. In contrast, the frequency nadir improves to 58.4 Hz while the PV is participating in regulation with the proposed control. The settling time to reach a steady state frequency value is also reduced from 10s to 2s.

7.2.3 Fast Frequency Regulation for Step Change in Load

In this part, a step change in load is applied to the system during steady-state operation. The load is changed from 240W to 250W at 10s where the PV is both connected and disconnected (to the control diagram in Fig. 7.3) to compare the frequency regulation of the system by the generator alone and the PV-generator combination. The results are depicted in Fig. 7.5a. The simulation results verify

that the frequency nadir once again is reduced when the proposed VI-ANN controller participated in frequency regulation. The extra load is well compensated by the proposed $P^{ref} \rightarrow V^{ref}$ model as can be seen in Fig. 7.5b and Fig. 7.5c.

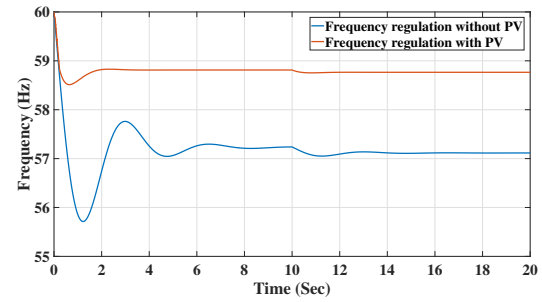

(a)

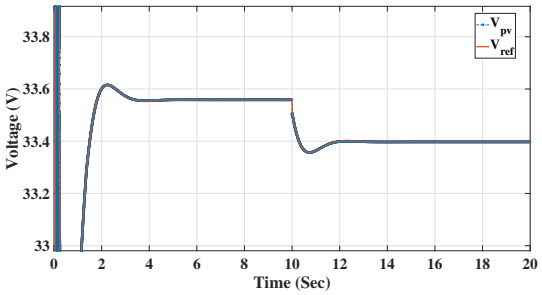

(b)

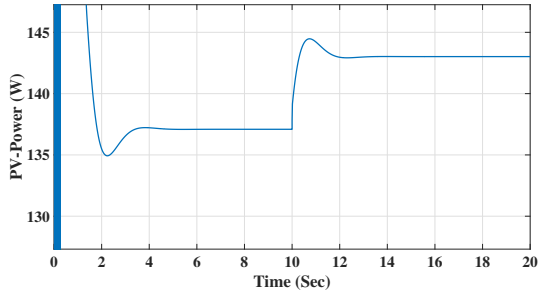

(c)

Figure 7.5: (a) FR with and without PV with step change in Load (b) Tracking of PV-Controller to Reference Voltage for step-change in Load (c) Power compensation by PV-Controller at 10 s for extra Load.

Fig. 7.5b illustrates that the reference voltage has decreased from 33.58V to 33.40V and the PI voltage controller for PV drives the operating point towards that reference point. The small decrease in voltage reference signifies that the proposed

ANN $P^{ref} \rightarrow V^{ref}$ model is working properly. Since the load increases from 240W to 250W at 10s, the operating point of the PV needs to shift towards the left after 10s to provide the increase in power. In this research, the operating point of PV is always maintained in the right side of MPP - as mentioned in Fig. 7.1 by the saturation block where the lower saturation point is V_{MPP} and upper saturation point is V_{OC}. The location of operating point always in the right side of MPP makes the system more stable since the V_{PV} varies very little between the above mentioned saturation limits. In this scenario, the only way to increase the power is to perturb the voltage towards the left with respect to its current position. The decrement of the voltage reference results in an increment of power which is also reflected in Fig. 7.5c.

7.2.4 Frequency Regulation with Step Change in Irradiance

In this section, the irradiance is changed from 1000 W/m^2 to 900 W/m^2 at 10s while the load is kept constant at 240W. The results are shown in Fig. 7.6. As can be seen from Fig. 7.6a, the frequency regulation is well maintained before and after the irradiance changes. The frequency nadir is small and, after the step change in irradiance, the frequency quickly settles to a steady-state value. Fig. 7.6b shows that the reference voltage is decreased before and after 10s by the ANN $P^{ref} \rightarrow V_{ref}$ model. As mentioned, the irradiance is decreased from 1000 W/m^2 to 900 W/m^2, graphically it means the P-V curve at 900 W/m^2 will be seen below the 1000 W/m^2 curve. Therefore, in order to provide the same power, the voltage reference must decrease when the irradiance is at 900 W/m^2. Also, the power provided by the PV is expected to be same regardless of the irradiance as the load has not changed. Though the power extraction from PV has not remain exactly same as depicted in

Fig. 7.6c, it does not have a major impact on the frequency regulation performance of the system.

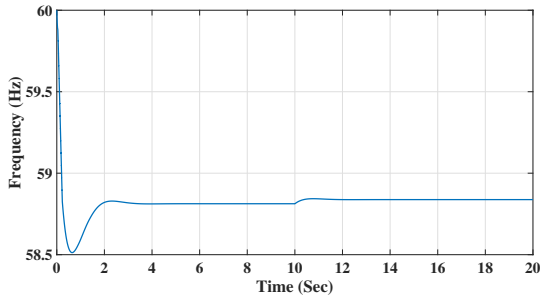

(a)

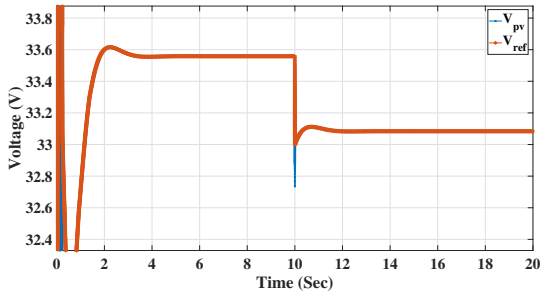

(b)

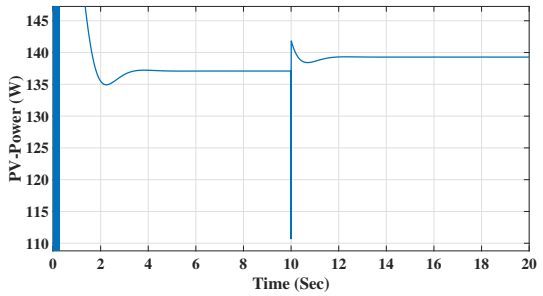

(c)

Figure 7.6: (a) FR by VI-ANN controller while step change of irradiance occurs (b) Tracking of VI-ANN controller to Reference Voltage for step-change in Irradiance (c) PV-power operating point for step change in irradiance

7.3 Summary

This chapter studies frequency stability in a hybrid microgrid system consisting of PV and a synchronous generator where the PV has participated in frequency regulation. The participation of PV in injecting active power has been conducted by an ANN-based V^{ref} generator where the inputs of the ANN controller are irradiance, temperature, and a generated power reference, P^{ref}. This P^{ref} is adaptive towards load changes and is generated by VI for supporting frequency stability. Several cases such as a step change in load and step change in irradiance are conducted to verify the efficacy of the proposed system. Simulation results showed that the proposed controller performed very well in regulating frequency in comparison to a baseline case of SG based frequency regulation system. The proposed controller not only improved the frequency nadir significantly but also reaches the steady state much faster. System frequency regulation could have been further improved if more accurate machine-learning models were utilized. The small prediction error introduced by the ANN block in predicting the V^{ref} causes moderate variation in active power generation. This will be investigated in more detail in future work, and other machine-learning models will be also explored to find out the best RMSE to train the VI-ANN controller. In addition, the proposed controller is aimed to be embedded into a physical microcontroller in Control-Hardware-In-The-Loop (CHIL) validation.

CHAPTER 8

DYNAMIC FREQUENCY REGULATION BASED ON HIERARCHICAL CONTROL OF DERS IN MICROGRID

This chapter is the extension of the previous chapter where frequency regulation is performed in a PV-Battery-Synchronous Generator-based hybrid microgrid system. The proposed control strategy fully utilizes the operating region of the P vs V -the curve of PV-array before it triggers the Battery to operate to provide further frequency regulation. The proposed control method deploys PV as the primary controller and battery as a secondary controller for desired frequency regulation. The structure of this chapter is as follows: Section 9.1 describes the proposed control methodology, section 9.2 provides detailed analysis for different test case scenarios to verify the efficacy of the proposed control algorithm and section 9.3 summarizes the chapter.

8.1 Proposed Methodology

The proposed method utilizes two controllers, a PV-side controller and a battery-side controller which perform desired control actions for regulating frequency. In this work, the PV-side output is considered the main frequency support source. Once the PV is no longer capable of providing the required frequency support, the battery will provide additional support to manage any frequency disturbances. Fig. 8.1 shows the implemented system with the proposed controllers where the PV-side controller is shown in green, and the battery-side controller is in yellow. The following subsections provide a detailed description of each of the controllers.

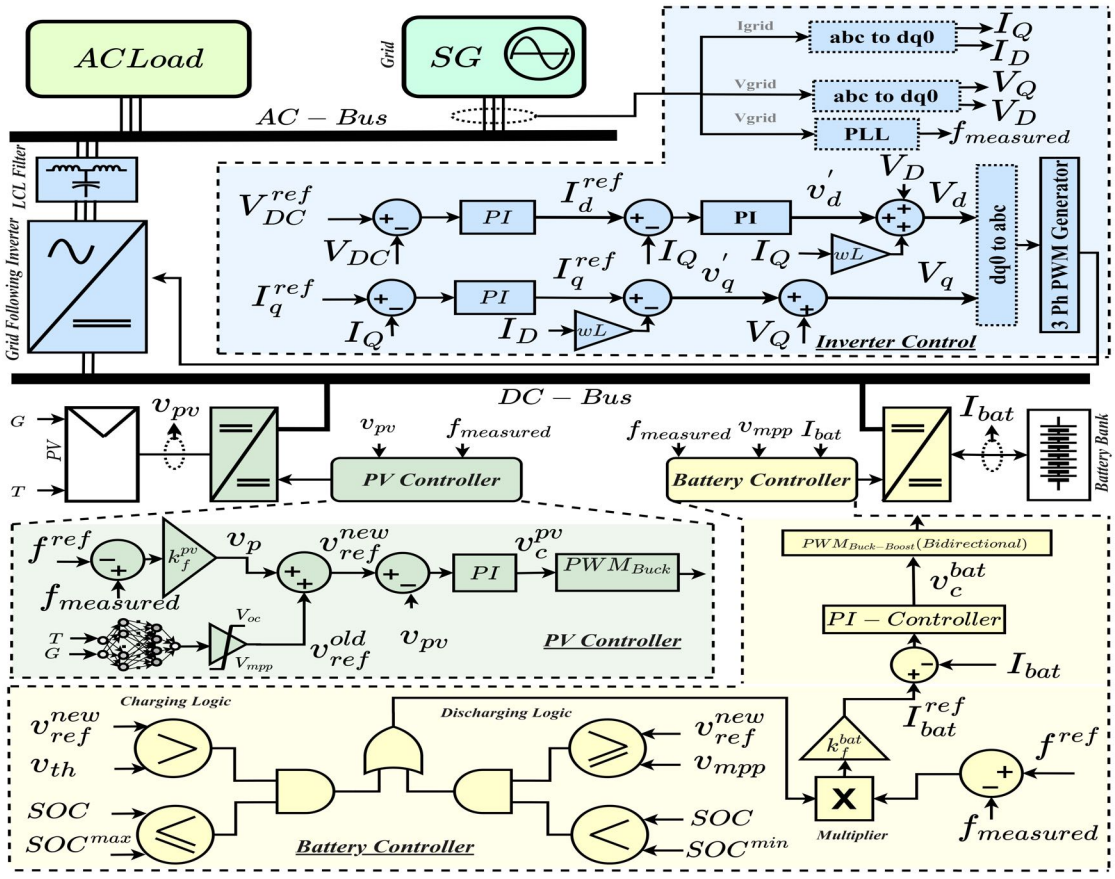

Figure 8.1: Proposed controllers in DERs based Microgrid

8.1.1 PV-side Controller

The PV-side controller first compares the measured frequency, f_{measured}, with the reference frequency, f^{ref}, of 60 Hz. The difference, or error, is amplified by a proportional gain, k_f^{pv}, which allows the mapping from the frequency region to the voltage region directly. The voltage reference, v_c^{pv}, from the PI controller, is calculated as follows in Eq. 1.

$$v_c^{pv} = k_p^{pv}\left(v_{\text{ref}}^{\text{new}} - v_{pv}\right) + k_i^{pv}\int\left(v_{\text{ref}}^{\text{new}} - v_{pv}\right)dt \tag{8.1}$$

k_p^{pv} and k_i^{pv} are the proportional and integral gains of the PI controller, v_{pv} is the operating voltage of the PV, and v_{ref}^{new} is the desired reference voltage based on

Eq. 2.

$$v_{\text{ref}}^{\text{new}} = v_{\text{ref}}^{\text{old}} + v_p \tag{8.2}$$

In Eq. 2, v_{ref}^{old} is the previous time-step voltage reference, and v_p is the linearly mapped value from frequency deviation to voltage, shown in Eq. 3.

$$v_p = k_f^{pv} \left(f_{\text{measured}} - f^{\text{ref}} \right) \tag{8.3}$$

This mapped voltage is added to v_{ref}^{old} to generate the new operating point v_{ref}^{new}, before being passed to a PI controller which will attempt to change the existing operating point of the PV to that new operating point. v_{ref}^{new} can shift up or down along the P-V curve according to the load increment or decrement for delivering desired frequency support. However, v_{ref}^{new} will always remain on the right side of the PV's characteristic P-V curve and a saturation constraint will limit the actual PV operating point (v_{pv}) from going below v_{mpp} (the voltage associated with the maximum power point) and beyond v_{th}. If v_{ref}^{new} is above v_{th}, rather than curtailing PV, the battery will begin to charge, thus allowing v_{th} to be maintained if adequate storage for power is available. Furthermore, an Artificial Neural Network (ANN) model is used to predict v_{mpp} at any particular irradiance (G) and temperature (T). The optimal parameters of the PI controller are chosen according to [96].

One of the benefits of the proposed PV-side controller is that the mapping of frequency difference to voltage reduces the need for an extra power reference generator thereby simplifying the control algorithm. Moreover, implementing a VI-based power reference generator would require a derivative component. This would make it vulnerable to instabilities introduced by rapidly changing frequency measurements.

8.1.2 Battery-side Controller

The battery-side controller will provide supplementary frequency support only when the PV-side controller and source are unable to provide the required frequency regulation. This operation is based on V_{ref}^{new}, V_{th}, V_{mpp}, the current SOC of the battery, and the threshold values for maximum and minimum SOC, SOC^{max} and SOC^{min}. The voltage reference, v_c^{bat}, from the battery PI controller, is calculated in Eq. 4.

$$v_c^{\text{bat}} = k_p^{bat} \left(I_{\text{bat}}^{\text{ref}} - I_{\text{bat}} \right) + k_i^{bat} \int \left(I_{\text{bat}}^{\text{ref}} - I_{\text{bat}} \right) dt \tag{8.4}$$

k_p^{bat} and k_i^{bat} are the proportional and integral gains of the battery PI controller, and I_{bat} is the previous time-step current reference. The battery-side controller will generate the new reference current, $I_{\text{bat}}^{\text{ref}}$, for the battery using Eq. 5.

$$I_{\text{bat}}^{\text{ref}} = k_f^{\text{bat}} \left(f^{\text{ref}} - f_{\text{measured}} \right) * \text{ L} \tag{8.5}$$

Frequency difference (error) is amplified by a proportional gain, k_f^{bat}, and L which contains a logical value of either 0 or 1 depending on SOC. The discharging of the battery is activated when v_{ref}^{new} is less than v_{mpp} and $SOC(t)$ is greater than SOC^{min}. The voltage v_{mpp} is the point at which PV reaches its maximum power and since the discharging logic of the battery will only be activated if v_{ref}^{new} is less than v_{mpp}, the battery will act as a supplemental frequency-support controller. This is because if the load requires more power than can be provided by the PV operating at v_{mpp}, PV loses its ability to provide proper frequency support and battery power is required. The battery-side controller logic will not let the battery discharge before reaching the maximum power point of the PV, assuring maximum PV output utilization.

The charging of the battery is activated only when v_{ref}^{new} is greater than v_{th} and $SOC(t)$ is less than SOC^{max}. When the PV operating point (v_{pv}) lies between v_{mpp} and v_{th}, PV is performing frequency regulation without taking any assistance from the battery. However, if v_{ref}^{new} becomes greater than v_{th}, the battery-side controller will activate the battery to start charging in order to provide further frequency support. This charging mechanism not only requires a smaller battery size, which reduces the overall system cost, but it also lowers the current throughput of the battery, thus prolonging battery life.

8.2 Results and Discussions

In the first part of this section, the simulation results are demonstrated to verify the proposed controller by providing different load scenarios. In the second part, hardware simulation results are shown to validate the proposed controller.

8.2.1 Simulation results for different load steps

The starting load is kept constant at 150 W until 5 sec where a step increment to 200 W is introduced. Then at 10 sec, the load steps decreased to 20 W. Fig. 8.2 demonstrates that the proposed controllers are capable of regulating frequency very close to the reference frequency of 60 Hz despite the step changes.

The power output of the PV can be seen in Fig. 8.3a. The maximum power of the PV used is 140 W and can be seen being generated until 10 sec when the load is reduced to 20 W. The total output remains higher after 10 sec due to the charging of the battery. Fig. 8.3b depicts how the PV-operating point increases along the right side of the P-V Curve to support the load, in other words, to regulate the frequency. Maximum power is reached at a v_{mpp} of 50 V and thus, the PV is operating at v_{mpp}

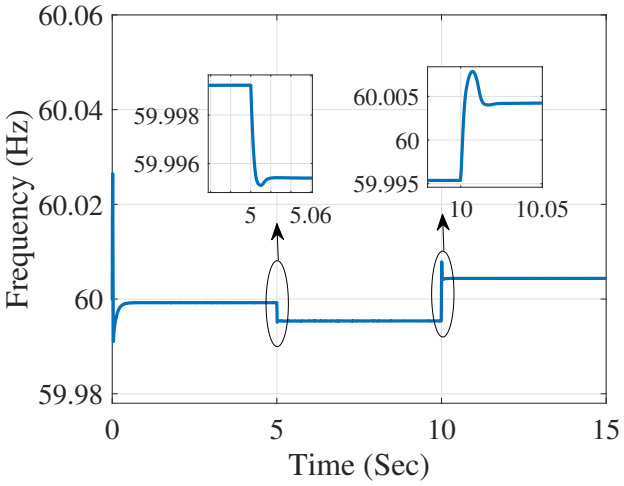

Figure 8.2: Frequency response by the proposed control algorithm.

from 0 sec to 10 sec. At 10 sec, the PV-operating point increases, away from v_{mpp} towards v_{th}, to regulate frequency in response to a reduction in load.

Since the load requires 150 W during 0 to 5 sec, the PV operates at v_{mpp} resulting in the maximum power output, P_{mpp}, of 140 W to utilize the maximum PV power. The irradiance is kept constant during that time. Since PV output is not sufficient to provide frequency support for this condition, the battery-side controller enables the discharging logic of the battery in order to compensate for the remaining power deficit.

Fig. 8.4a illustrates that the controller generates a positive current reference (I_{bat}^{ref}) and that the battery current follows the reference current closely. Between 5 sec and 10 sec, the load demand is 200 W. Since PV has already reached P_{mpp} (140 W) in the previous scenario, the controller does not permit the operating point to go beyond 50 V. Thus, the battery discharging logic allows for the generation of more power to provide the necessary frequency support.

Between 10 sec and 15 sec, the load demand is decreased to 20 W. Since PV was previously operating at 140 W with the corresponding v_{mpp} voltage of 50 V,

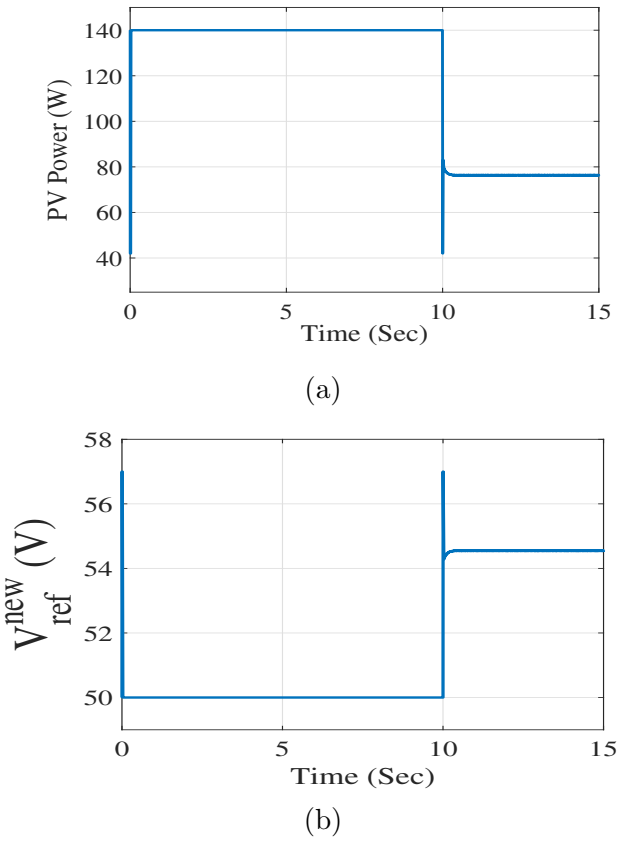

Figure 8.3: (a) PV power and (b) voltage operating points from 0 sec to 15 sec.

the controller now drags the PV operating point to the right by increasing v_{ref}^{new}, consequently reducing the PV power output. In this paper, v_{th} is chosen to be 54.5 V, so when v_{ref}^{new} is greater than v_{th}, the controller enables the battery charging logic to store extra PV power output, thus regulating the frequency. This is seen in Fig. 8.4a where the battery-side controller generates a negative (charging) current and the battery current closely follows. Fig. 8.4b also confirms that the battery discharges for the first 5 sec, increasing discharge between 5 sec and 10 sec, and charges between 10 sec and 15 to provide the best frequency support.

The change in SOC of the battery over time can be seen in Fig. 8.4c. The SOC of the battery decreases between 0 sec to 5 sec, and even steeper for 5 sec to 10 sec

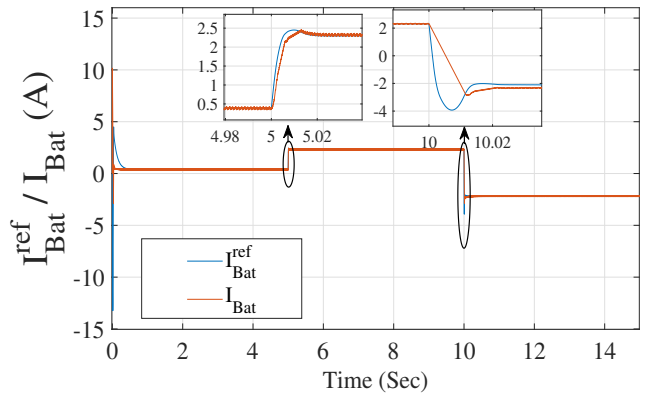

(a)

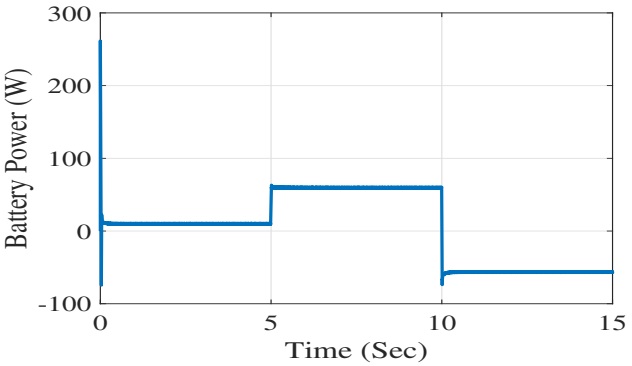

(b)

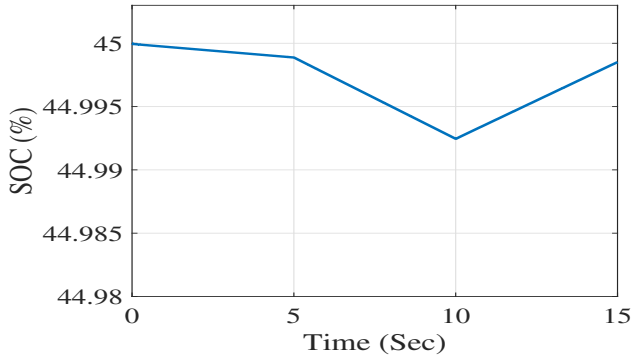

(c)

Figure 8.4: (a) Actual battery current and reference current generated by the controller, (b) Battery power output for varying load, and (c) SOC of the battery while charging and discharging.

since the battery is progressively increasing its discharging to perform supplementary frequency regulation. SOC increases between 10 sec to 15 sec as the battery charges

due to v_{ref}^{new} being greater than v_{th}. The following control parameters are used for the simulation: $k_p^{pv} = 3$, $k_i^{pv} = 5$, $k_f^{pv} = 1500$, $k_p^{bat} = 1$, $k_i^{bat} = 10$.

It is worth mentioning that, most of the existing PV-Battery-based frequency regulation systems used MPPT for extracting maximum power from PV and used the battery as a primary regulator. The problem with this strategy is that the battery size has to be bigger to consume the surplus PV power since PV is always working in MPPT mode. In addition, the battery will lose its regulation capacity, if fully charged. The proposed system has the inherent capability of addressing those issues because of its load-adaptive way of changing the operating point - which can be seen from Fig. 8.3b that shows PV-side controller increases V_{ref}^{new}, thus reduces the PV-power to support the load reduction at 10 s, acting as a primary controller. The battery controller, acting as a secondary controller, then starts charging to compensate for the remaining load reduction - depicted in Fig. 8.4b and 8.4c.

8.2.2 Hardware Simulation of the proposed system

In order to experimentally validate the proposed controllers, a real-time simulator platform is used to perform a hardware simulation. Fig. 8.5 shows the dynamic shifting of battery power, frequency, the operating voltage of PV, and the power output of PV shown in yellow, pink, blue, and green respectively during the load change from 20 W to 200 W. A gain of 0.1 is used to constraint all the aforementioned parameters within the simulator output limits of $+/-16$ V. It is clear that the system frequency remains unaltered around 60 Hz despite the drastic load change occurrence which validates the efficacy of the proposed controllers.

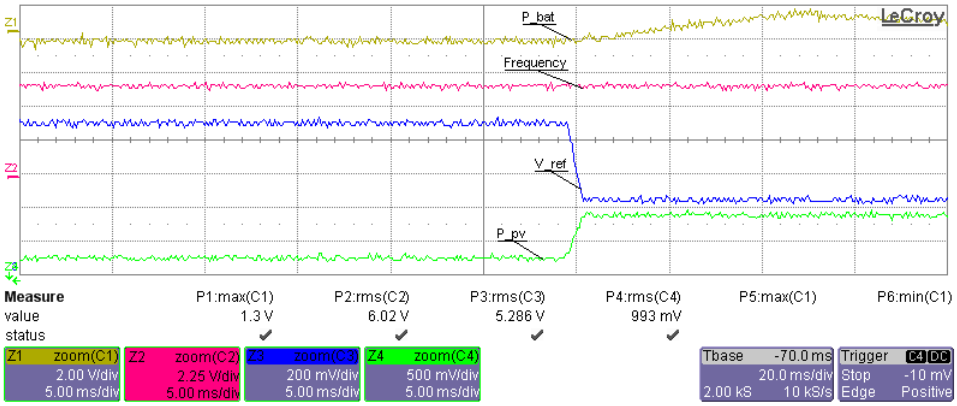

Figure 8.5: Dynamic shifting of operating points when load changes from 20 W to 200 W.

8.3 Summary

The research conducted in this chapter studies frequency regulation in a hybrid microgrid system consisting of PV, battery, and synchronous generator. PV has participated in frequency regulation as the primary source with the battery as the secondary source. The participation of PV in injecting active power has been conducted by a PV-side controller for frequency-to-voltage reference generation. The proposed controller generates the reference voltage directly from frequency deviation without the use of any VI power reference generator. This reference voltage generation is adaptive toward load changes and uses battery charging and discharging to stabilize system frequency when the generated voltage reference goes beyond a predefined range on the P-V curve. A scenario is generated where multiple load step changes are applied to verify the efficacy of the proposed control algorithm. Simulation and real-time hardware simulation results show that the proposed controller performs very well in regulating the frequency of the system as well as quickly reaching a steady state.

CHAPTER 9

A UNIFIED CONTROL STRATEGY FOR VOLTAGE REGULATION IN A MICROGRID SYSTEM

This chapter proposes a unified controller to regulate the bus voltage for the microgrid in islanding mode using only PV-source. The unified control mechanism drives the PV in voltage-source control mode to execute the desired voltage regulation, in addition, it has the capability to drive the operating point near MPP according to load demand. The chapter structure is arranged as follows: Section 9.1 provides the details of the proposed control technique with AC-DC microgrid scheme, section 9.2 depicts the results with different test case scenarios such as step load change, step irradiance change, irradiance ramping up and down in addition to real-time hardware simulation and section 9.3 provides the summary of the chapter.

9.1 Proposed Control Strategy

The proposed control strategy with a 2-stage power electronic conditioning framework is shown in Fig. 9.1. The control strategy is used to determine the desired PWM signal to be applied to the DC-DC buck converter for effective DC bus voltage regulation. The working principle of the controller can be summarized under three main as shown in Fig. 9.1.

An outer control loop generates the desired reference voltage, v_{ref}^{new} (PV operating voltage set point). In the outer control, the proposed controller generates a control signal by taking the difference between the reference DC bus voltage, v_{bus}^{ref}, of 800 V and the DC bus voltage, v_{bus}, and multiplies the error by a negative proportional constant to generate the control signal v_c, as shown by (9.1).

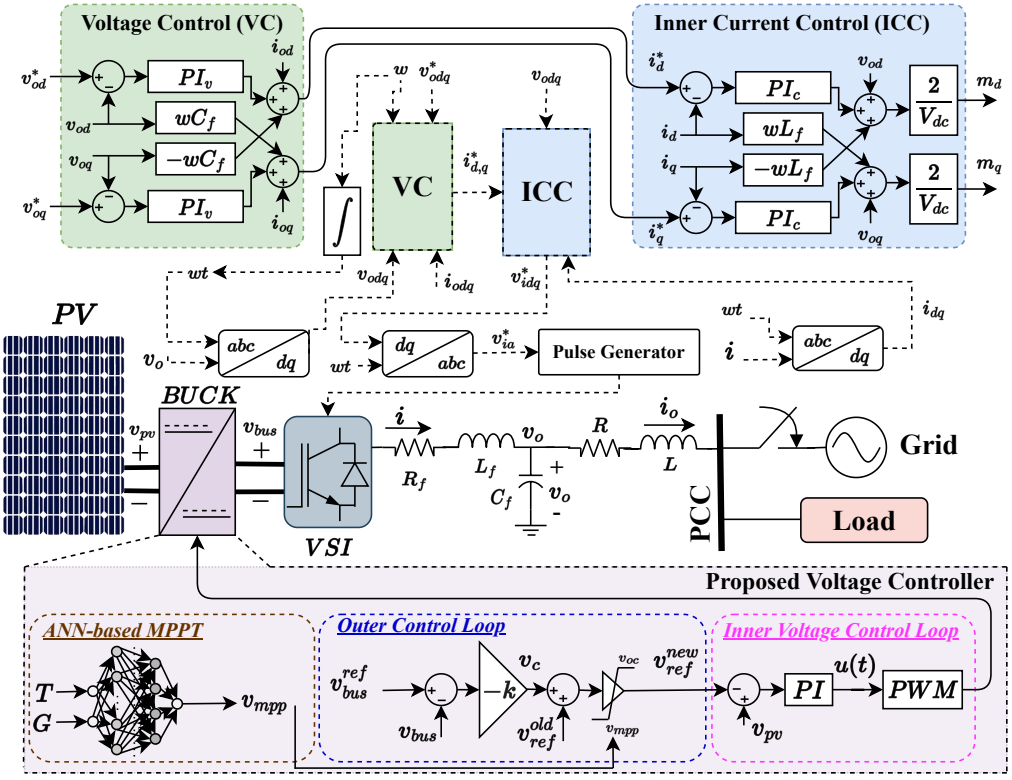

Figure 9.1: Proposed controller in a PV-based microgird

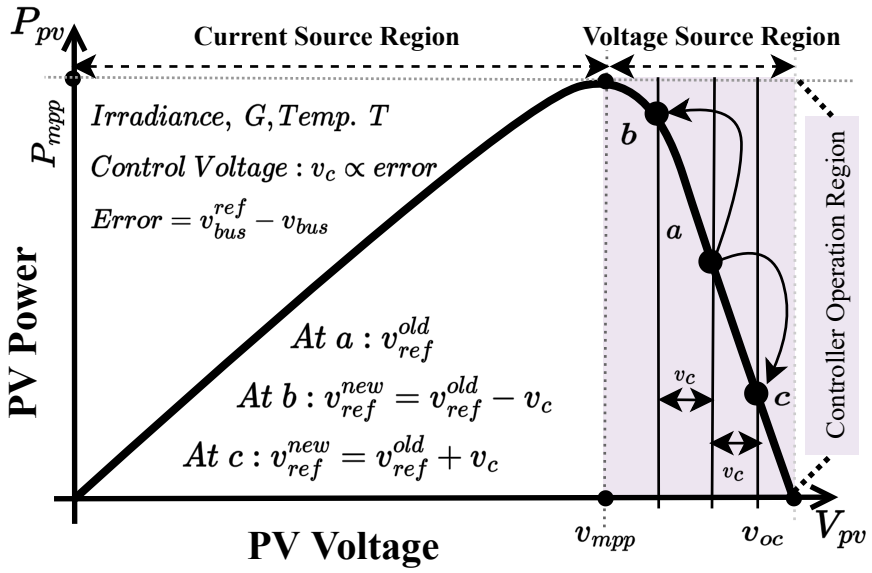

Figure 9.2: PV operating points and mode of operations

$$\begin{aligned} v_c &= -k \times (v_{bus}^{ref} - v_{bus}) \\ error &= v_{bus}^{ref} - v_{bus} \end{aligned} \tag{9.1}$$

If the error is positive, it means the PV power output is less than the required load power. In this case, v_c will be negative, thus shifting the operating point closer to the MPP to balance the load. However, if the error is negative (PV output is greater than the load), v_c will be positive and the operating point will shift away from the MPP to curtail PV power. This relationship is described in (9.2):

$$v_{ref}^{new} = v_{ref}^{old} + v_c \tag{9.2}$$

Fig. 9.2 demonstrates the conceptual operating range for the proposed controller. The initial operating point is shown at point a from which it can be shifted towards the MPP (v_{mpp}) to point b when v_c is negative, or away from the MPP to point c when v_c is positive according to (9.1).

An inner voltage control loop follows the reference signal generated by the outer control loop. In the inner loop control, a PI controller is utilized which generates $u(t)$, as shown in (9.3), in order to drive the PV terminal voltage, V_{pv}, to follow outer loop-generated v_{ref}^{new} value. The control parameters for the PI controller, K_p^i and K_i^i, are optimized with the following objective function, and constraints using the Particle Swarm Optimization (PSO) algorithm found in [96].

$$u(t) = K_p^i(v_{ref}^{new} - V_{pv}) + K_i^i \int_0^t (v_{ref}^{new} - V_{pv})dt \tag{9.3}$$

$$ISTSE = \int_0^\infty t^2 e^2(t)dt \tag{9.4}$$

Where: $e(t) = V_{ref} - V_{out}$

By choosing The Integral of Square Time-weighted Squared Error (ISTSE), the settling time and steady-state errors will be reduced.

Objective Function:

$$J = min|ISTSE| \tag{9.5}$$

Subject to:

$$\begin{cases} K_p^{min} \leq K_p \leq K_p^{max} \\ K_i^{min} \leq K_i \leq K_i^{max} \end{cases} \tag{9.6}$$

An ANN-based MPPT predicts the v_{mpp} corresponding to the unique P vs. V curve for each varying irradiance and temperature. The saturation block following v_{ref}^{new} ensures that the generated operating point always remains within v_{mpp} and v_{oc} on the right side of the MPP. When the grid is not present during the islanded mode, the PV controller is solely responsible for regulating the DC bus voltage around the desired voltage reference. When the PV is operating at the MPP, and

the load is required less than the power generated from PV, the operating point of PV is required to be shifted from MPP to either the right or left in order to curtail generation. The left-hand side (with respect to the MPP) of the P vs. V curve can be considered as a current source region, and the right-hand side can be considered as a voltage source region as shown in Fig. 9.2. This is due to the fact the current remains almost constant in the left side region and voltage changes very narrowly in the right side region. Thus, if the operating point is shifted to the left side, there will be oscillations due to voltage variations. A detailed description of voltage-source and current-source regions by small-signal analysis is provided in the next part of this section. The inaccessibility to the left side of the P vs. V region does not reduce any degrees of freedom since the power delivery at any operating point to the right of MPP is exactly equal to power on the left side, as shown in Fig. 9.2. The shifting of the operating point towards the right side of MPP benefits from fewer oscillations.

The v_{mpp} voltage is generated from the ANN-based Maximum Power Point Tracker (MPPT) using irradiance and temperature values. The description of the ANN-based controller is provided in the subsequent section.

It is important to emphasize that both MPP and PV curtailment operation can be reached by the proposed unified controller according to load variations at the output side and weather parameter variations at the input side. This dynamic swing of the operating point between v_{mpp} and v_{oc} regardless of irradiance and load variations ensures very stable voltage regulation of the DC bus which assists the Voltage Source Inverter (VSI) to regulate the AC bus voltage and current at the desired level during the islanded mode of operation.

9.1.1 Small signal analysis of PV-buck linear model

The PV I-V curve can be modeled using the following equations:

$$i_{pv} = I_{pv} - I_o \left[\mathrm{e}^{\left(\frac{v_{pv}+R_S \cdot i_{pv}}{V_t \cdot N_S \cdot a}\right)} - 1 \right] - \frac{v_{pv} + R_S \cdot i_{pv}}{R_p} \tag{9.7}$$

By differentiating (9.7), the derivative can be found at any point (V, I) on the I-V curve. This derivative then can be used to find the slope for three regions. The current source region, the MPP region, and the voltage source region.

$$g(V,I) = \frac{-I_o \cdot e^{\left(\frac{V+I \cdot R_S}{N_S \cdot V_t \cdot a}\right)} - \frac{1}{R_p}}{1 + \frac{R_S}{R_p} + I_o \cdot e^{\left(\frac{V+I \cdot R_S}{N_S \cdot V_t \cdot a}\right)} \cdot \frac{R_S}{N_S \cdot V_t \cdot a}} \tag{9.8}$$

where I_{pv} and I_o are the PV and saturation currents of the array, V_t is the thermal voltage of the array with cells connected in series, Ns and Np are the equivalent series and parallel resistances of the array, and a is the diode ideality constant.

The non-linear I-V characteristics of the PV module are linearized into 3 regions for the ananlysis. For small signal analysis, Fig. 9.3 is used for PV-Buck system linearization whereas linearized PV voltage, v_{pv} can be expressed as a Thevenin equivalent circuit by a voltage source, V_{Th} and a resistor, R_{Th} in series and transfer function of linearized PV-Buck system can be expressed as follows [99]:

$$G_p = \frac{\tilde{v}_{pv}}{\tilde{d}} = \frac{sLI_L R_{Th} + DV_{PV} R_{Th}}{s^2 LCR_{Th} + sL + D^2 R_{Th}} \tag{9.9}$$

The current source region (AB), The MPP region (BC), and the voltage source region (CD). are shown in Fig. 9.4. The PV array, having the following characteristics at those corresponding regions, is also shown as $m_{AB} = -0.0104$, $m_{BC} = -0.2889$ and $m_{CD} = -1.1127$.

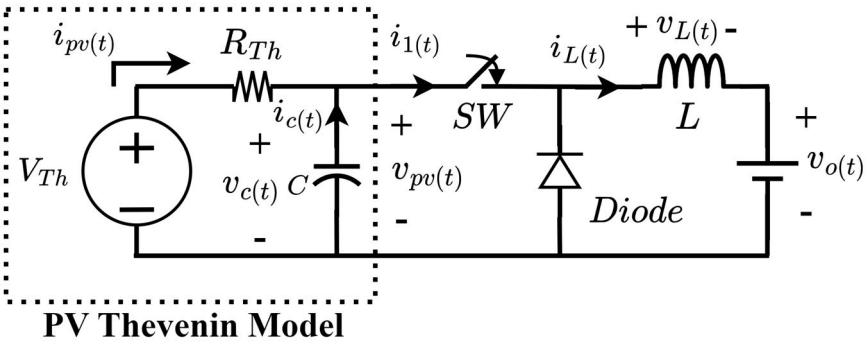

Figure 9.3: PV-Buck equivalent model

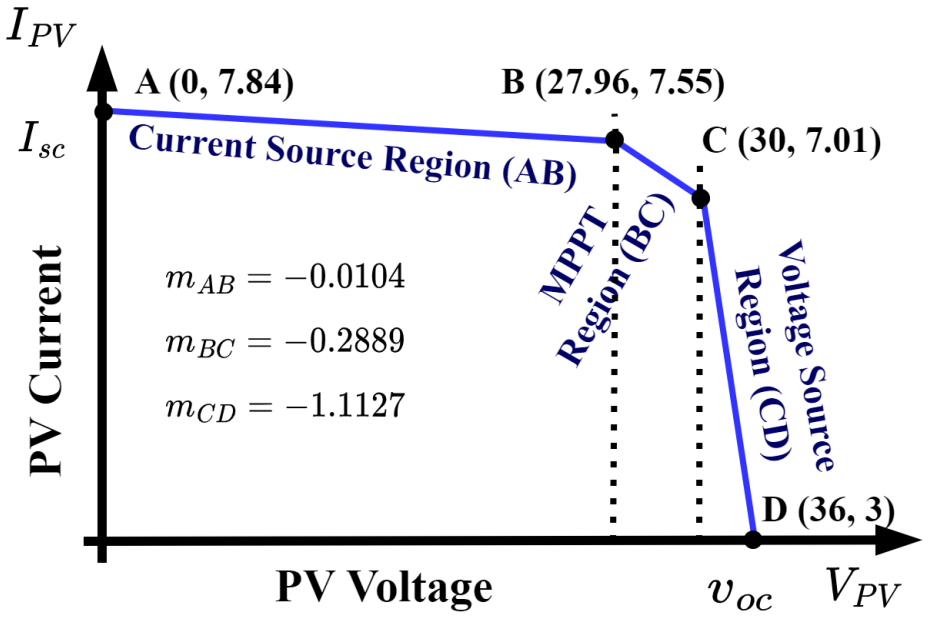

Figure 9.4: Linear approximation of PV

The steady-state parameters are given in the following expressions:

$$V_o = D \times V_{PV},$$
$$I_o = I_L = \frac{V_{Th} - V_{PV}}{R_{Th} \times D},$$

After plugging the respected values in (9.9), the following expression is utilized for making the frequency response analysis.

$$G_p = \frac{0.01892s + 10.78}{1.797 \times 10^{-6}s^2 + 0.002s + 0.1298} \tag{9.10}$$

Fig. 9.5 shows the open-loop gain comparisons of G_p at different frequencies of the voltage and current source regions. The comparison is made by setting $L = 2mH$, $C = 1uF$, $D = 0.38$ (for voltage source region), and $D = 0.75$ (for current source region). As can be seen from the figure, the dc-gain of the voltage source region is much better than the current source region which confirms a much smaller steady-state error in the voltage source region. Moreover, the addition of a PI-compensating block will further increase the dc-gain. Though the cross-over frequency in the voltage-source region is slightly below in comparison to the current-source region, it should provide a faster response for a step change.

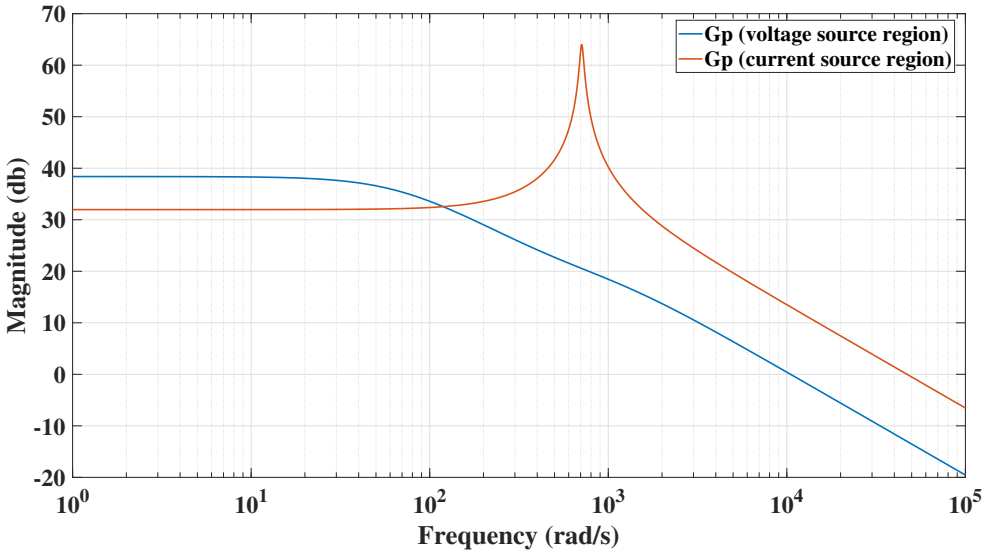

Figure 9.5: Open-loop gain characteristic comparison between voltage and current source regions

Fig. 9.6 also confirms that the voltage source region would be the best and easiest option for designing the compensation network. The choice of buck-converter rather than boost-converter also provides the benefit of having a good phase margin which

is closely related to stability and transients. Considering all the advantages of the voltage-source region, the compensation network has been designed with respect to that region which will provide a faster transient response.

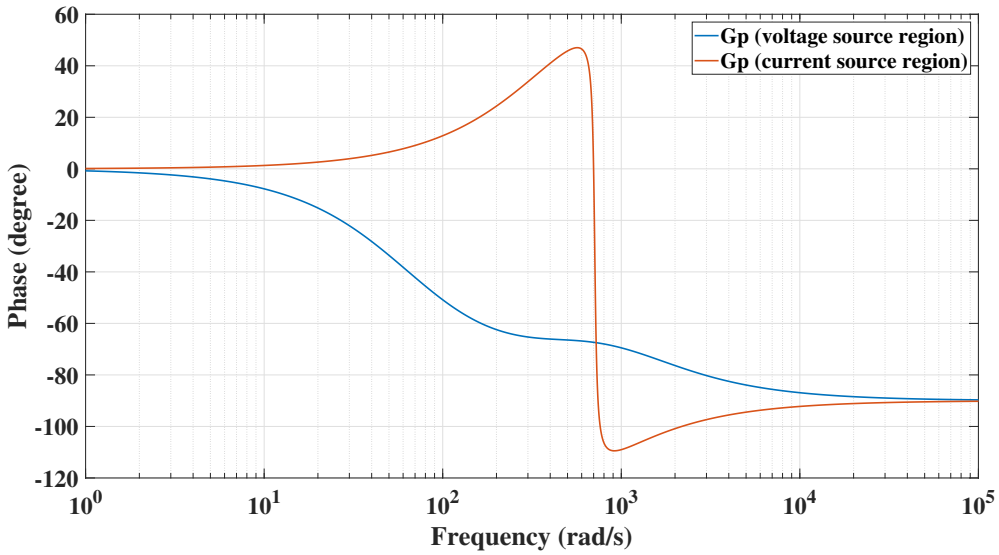

Figure 9.6: Open-loop angle characteristic comparison between voltage and current source regions

9.1.2 Description of the ANN model

The utilized ANN model is a standard feed-forward, fully-connected (dense) neural network used for regression. The network is comprised of a single input, hidden, and output layer where the hidden layer consists of 100 processing elements (and a bias) whose outputs are passed through a Rectified Linear (ReLu) activation function. The ANN model predicts a V_{mpp} value based on 2 standardized input parameters which are irradiance and temperature.

The data used to train the ANN was produced by incrementing irradiance with a step size of 10 from $700W/m^2$ to $1000W/m^2$ while keeping the temperature constant at $25°C$. Each increment of irradiance produced a unique P vs. V curve which was

sampled while linearly increasing voltage from the MPP voltage to an ordinary maximum operating voltage. Therefore, this process produced a 3-variable training and validation data set (2 features, irradiance and temperature, and 1 target, V_{mpp}) for each irradiance step which was then concatenated and shuffled before training. The ANN was trained and tested using k-fold cross-validation (where k=5) and produced the following performance metrics: Root-Mean-Square Error (RMSE) = 0.033, R-Squared = 0.99, Mean Squared Error (MSE) = 0.00109, and Mean Absolute Error (MAE) = 0.018872. Fig. 9.7 shows the ANN's predictions plotted against the true values which further buttresses the performance metrics listed above.

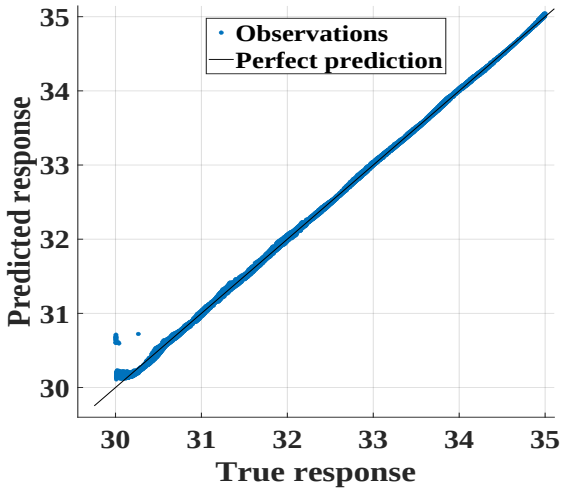

Figure 9.7: ANN true response vs predicted response

9.1.3 $v - f$ control mechanism of inverter

The output voltage at the AC bus can be regulated by controlling the output current (i) and voltage (V) of the inverter. The dynamics of the RL branch are used to determine the inner current control. It is possible to write the RL dynamic equation

from Fig. 9.1 as follows:

$$\begin{aligned} L_f \frac{di_d}{dt} &= -R_f i_d + w_o L_f i_q + v_{id} - v_{od} \\ L_f \frac{di_q}{dt} &= -R_f i_q - w_o L_f i_d + v_{iq} - v_{oq} \end{aligned} \tag{9.11}$$

The outer voltage control is derived from the dynamics of the filter capacitor (C_f). The capacitor dynamic equation can be written in dq-axis form as follows:

$$\begin{aligned} C_f \frac{d(v_{od})}{dt} &= i_d - i_{od} + C_f w_o v_{oq} \\ C_f \frac{d(v_{oq})}{dt} &= i_q - i_{oq} - C_f w_o v_{od} \end{aligned} \tag{9.12}$$

The control parameters for outer loop voltage control and inner loop current control are designed based on [100]. Equations (9.12) are simplified and solved using pole placement for pole-zero cancellation to obtain the PI control (Gc(s)) proportional (k_{pc}) and integral (k_{ic}) gains as shown in (9.13).

$$\begin{aligned} k_{pc} &= \frac{L_f}{\tau_c} \\ k_{ic} &= \frac{R_f}{\tau_c} \end{aligned} \tag{9.13}$$

where τ_c is a current control closed-loop time constant, which is typically selected to be 5 to 10 times that of the switching time ($\frac{1}{2\pi f_c}$).

Equations (9.11) are simplified, and using both phase margin and gain margin analysis, PI gains are selected such that the system is stable and robust against uncertainties in system parameters. The outer voltage PI control ($G_v(s)$) proportional (k_{pv}) and integral (k_{iv}) gains are selected using (9.14), whereas the phase margin is selected as 50^o:

$$\begin{aligned} k_{pv} &= C_f w_{gc} \\ k_{iv} &= \frac{k_{pv}}{\tau_v} \end{aligned} \tag{9.14}$$

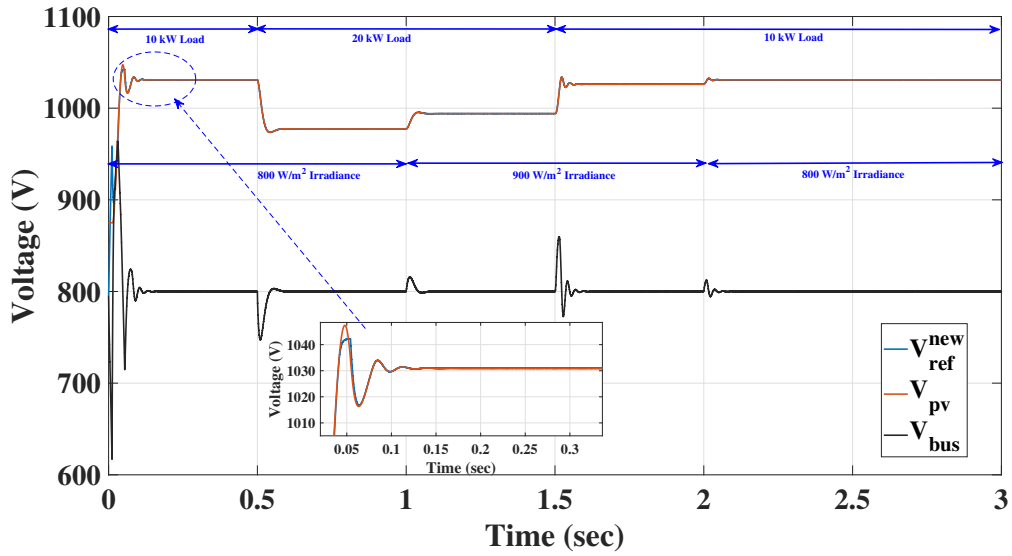

Figure 9.8: Dynamic operating point shifting by PV-side controller for voltage regulation during irradiance and load variations

9.2 Results and Discussion

In this section, several cases have been studied to verify the efficacy of the proposed controller, and a real-time hardware simulation is performed to validate the proposed controller. In the first part, a step irradiance change is imposed as well as a load step change. In the second part, ramping up and down irradiance is applied during which step load changes occur.

9.2.1 Step change in irradiance and load

Here, the initial load is constant at 10 kW until 0.5 s where it is increased to 20 kW and remains constant until 1.5 s. Then at 1.5 s the load is decreased to 10 kW and remains constant for the rest of the simulation. Similarly, the irradiance remains constant at 800 W/m^2 until 1 s where it is increased to 900 W/m^2 until 2 s. At 2 s, the irradiance is then decreased back to 800 W/m^2 and remains constant until the simulation ends.

As can be seen from Fig. 9.8, the controller is driving the system towards the operating point, v_{ref}^{new}, along the right side region of the P-V curve to regulate the DC bus voltage around 800 V. It is important to mention here that as long as the operating point lies to the right of the MPP, any increment in PV operating voltage reduces PV power output, and any decrement in PV operating voltage increases PV power output.

In order to cover the initial load of 10 kW with an irradiance of 800 W/m^2, the operating point experiences initial oscillations and then becomes steady. When the load increases to 20 kW at 0.5 s, v_{ref}^{new} reduces in order to increase PV power output to compensate, which is reflected on the v_{bus} curve. When the irradiance changes at 1 s from 800 W/m^2 to 900 W/m^2, the controller adjusts the operating point accordingly in order to curtail the PV power to compensate. The increment of irradiance from 800 W/m^2 to 900 W/m^2 automatically increases the power generation since PV power is proportional to irradiance. Thus the proposed controller properly drives the PV voltage with v_{ref}^{new} which subsequently reduces the PV power to compensate for the PV power increment that occurred. When the load drops to 10 kW again after 1.5 s, the controller further increases the operating point to balance generation and load.

Fig. 9.9 shows the AC-side 3-phase sinusoidal voltage signals regulated at 311 V with little disturbance at 0.5 s when the load increases from 10 kW to 20 kW. Similarly at 1.5 s when the load is decreased, as shown in the zoomed-in portions of Fig. 9.9. Fig. 9.10 also demonstrates and reflects the load change which results in current increment and decrement at 0.5 s and 1.5 s.

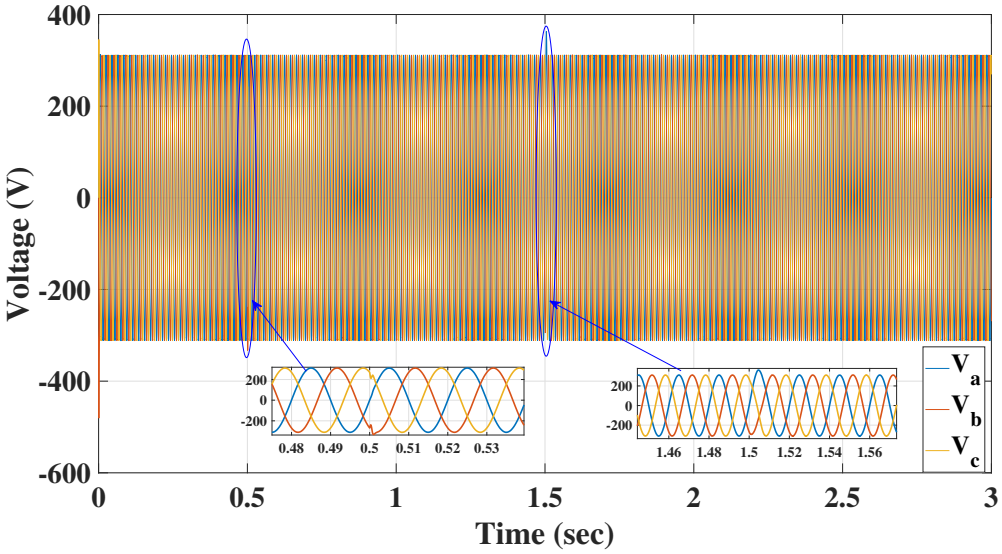

Figure 9.9: AC-side voltage regulation during irradiance and load variations

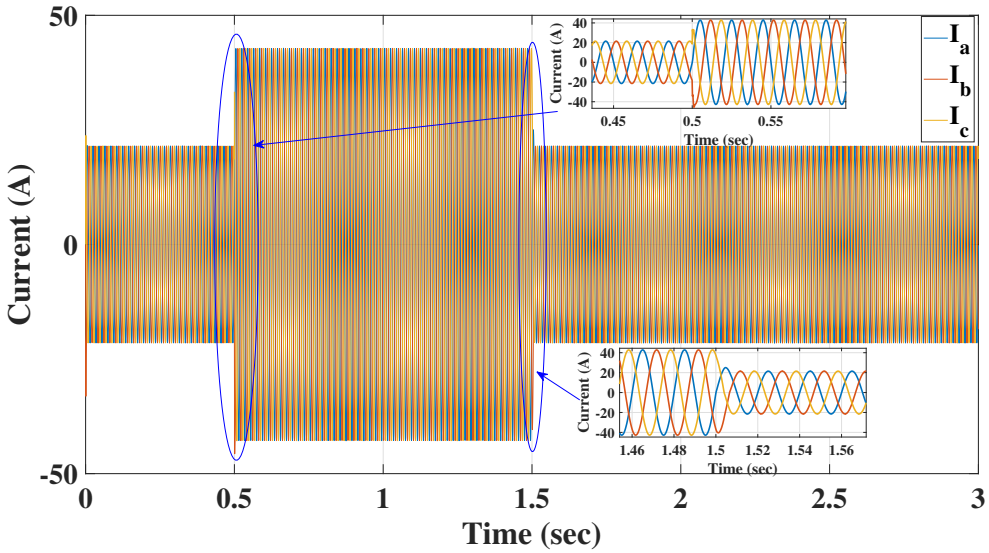

Figure 9.10: AC-side current change during irradiance and load variations

9.2.2 Ramping up and down of irradiance and step-change of load

In this part of the simulation, a ramping irradiance profile is applied to verify the efficacy of the proposed controller. The irradiance ramps up from 700 W/m^2 to 900 W/m^2 between 0 s to 1.5 s. A step load change is also applied at 0.5 s and 1 s,

shown in Fig. 9.11. Since the load remains constant at 10 kW between 0 s and 0.5 s, during which the irradiance is ramping up, the controller is gradually increasing the operating point, to compensate for the PV power output increase due to the gradual increase in irradiance. The correct control action is reflected on the v_{bus} signal which remains steady and well regulated at 800 V. When the load increases at 0.5 s to 20 kW, the controller reduces the operating point in order to increase the PV power output to compensate for the extra load. The controller then continues to gradually increase the operating point due to the irradiance also increasing during that time. At 1 s, the load reduces back to 10 kW, and because the irradiance is still ramping up, the controller drives the operating point gradually downward to compensate for the effect until 1.5 s. At 1.5 s, irradiance starts ramping down until 3 s from 900 W/m^2 to 700 W/m^2. The load experiences a step change at 2 s where it is increased to 20 kW. In order to compensate for the extra load, the operating point is lowered by the controller which results in a power increase. Afterward, the operating point gradually trends further downward to compensate for the gradual downward drifting of irradiance. Lastly, when the load drops to 10 kW at 2.5 s, the operating also changes accordingly to regulate the DC bus voltage around the desired nominal voltage level.

Fig. 9.12 depicts the regulated AC-side 3-phase sinusoidal voltage. There is little disturbance when the load increases from 10 kW to 20 kW at 0.5 s and 2 s. Similarly, when the load is decreased at 1 s and 2.5 s, the disturbance is minimal, as shown in the zoomed-in portions of Fig. 9.12. Fig. 9.13 also demonstrates the load step-change which is reflected as current increments and decrements at 0.5 s, 1 s, 2 s, and 2.5 s.

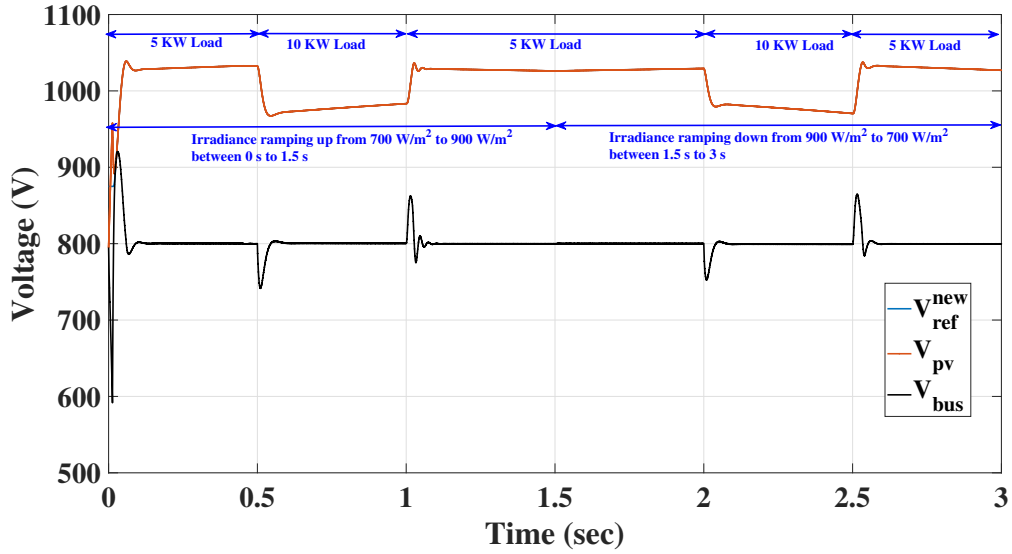

Figure 9.11: Dynamic operating point shifting by PV-side controller for voltage regulation during irradiance ramping and step load change

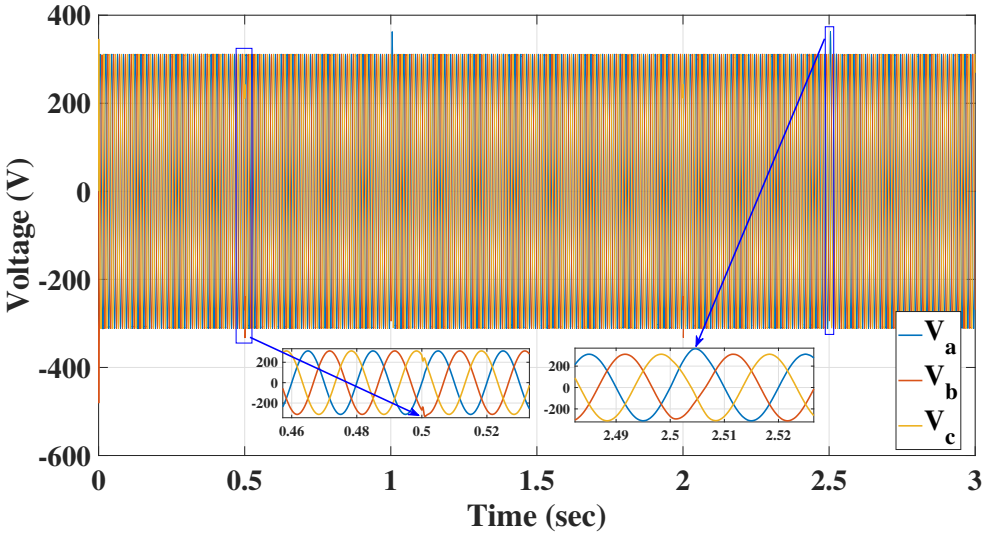

Figure 9.12: AC-side voltage regulation during irradiance ramping and step-load variations

9.2.3 Real-time hardware simulation

In order to experimentally validate the proposed controller, a real-time simulation platform is used to perform real-time Control Hardware-in-The-Loop (CHIL) sim-

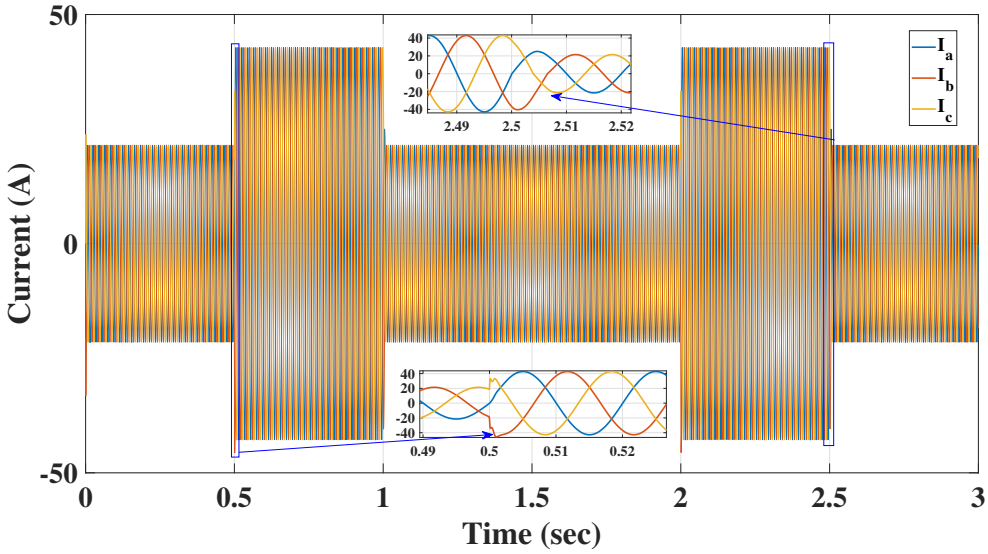

Figure 9.13: AC-side Current change during irradiance-ramping and step-load variations

ulations. Fig. 9.14 and Fig. 9.15 show the AC-side voltage, AC-side current, v_{ref}^{new}, and v_{bus} in yellow, pink, blue, and green respectively during the load change from 20 kW to 10 kW and 10 kW to 20 kW. The dynamic shifting of the operating point by the proposed controller during load step change is imposed.

A gain of 0.1 is used to constraint all the aforementioned parameters within the simulator output limits of $+/-16$ V. It is clear that the system DC bus voltage remains unaltered around 800 V despite the drastic load change occurrence which validates the efficacy of the proposed controllers.

9.3 Summary

The work of this chapter proposes a unified controller which regulates the DC-link capacitor (DC bus) voltage at the desired voltage level regardless of input side variations due to irradiance as well as output side variations due to load changes. It does so by following the load based solely on DC bus voltage information and ac-

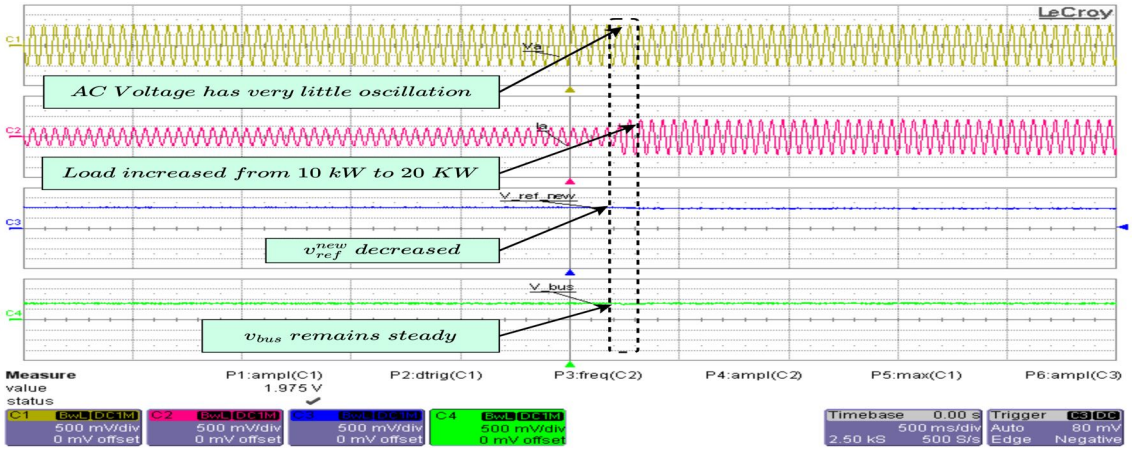

Figure 9.14: Dynamic shifting of the operating point when the load changes from 10 kW to 20 kW

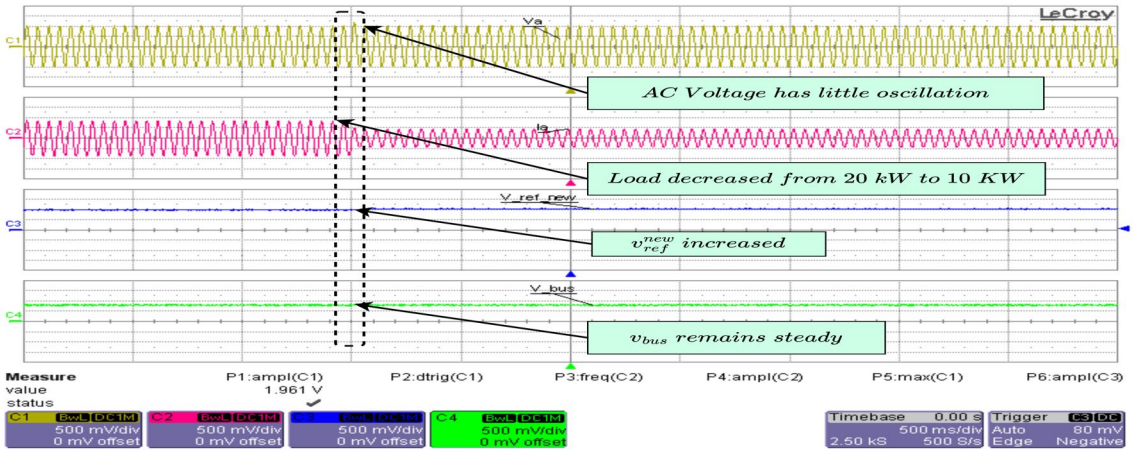

Figure 9.15: Dynamic shifting of the operating point when the load changes from 20 kW to 10 kW

cordingly shifts the PV operating point to balance the system with little oscillations, quickly reaching a steady state. The DC-side capacitor link voltage regulation is the mandatory condition for the VSI to perform its AC-side voltage regulation despite load-side variations. Simulation results and real-time hardware simulations demonstrated that the proposed controller can successfully regulate the DC bus voltage by dynamically adjusting its operating point within the right side region of the PV's P vs. V curve with respect to the MPP.

CHAPTER 10

CONCLUSION AND FUTURE WORK

This chapter provides a concise recap of the preceding chapters and emphasizes potential directions for future research.

10.1 Conclusion

The primary goals of this dissertation have been to design a maximum power point tracking (MPPT) algorithm with step size optimization and optimal sizing of PV and Energy storage system, voltage regulation of microgrid, and controller parameter-optimization of converters and design and implementation of Unified controller for voltage and frequency regulation of microgrid. To achieve these goals, the dissertation proposed, designed, and implemented a fast maximum power point tracking algorithm to procure more energy from PV-array with high efficiency for rapid-changing weather conditions, the optimal choice of control parameters for the converters to improve the transients, i.e., reduce overshoot, undershoot with faster responses, unification of MPPT controller and voltage regulation controller for hybrid microgrid by a single controller using an artificial neural network-based estimator, voltage regulation of microgrid by utilizing PV as voltage-source-control without using any energy storage devices and frequency restoration of a microgrid by the participation of PV with machine-learning based controller for faster settling time and fewer oscillations.

Chapter 3 introduces a binary search algorithm for the offline optimization of photovoltaic (PV) and battery systems. The algorithm aims to minimize costs by efficiently determining the optimal number of PV modules and batteries. Practical one-year irradiance and load data are used in the algorithm, which ensures accurate results. The objective function is based on the assumption that the total system

cost depends linearly on the number of batteries and PV modules. Simulation results demonstrate that the proposed algorithm maintains the state of charge (SOC) within predefined limits throughout the year, resulting in zero load deficit. This leads to improved battery health and increased longevity. Additionally, the algorithm can be applied with constraints on the number of PV modules and batteries, accommodating the available space at specific locations.

Chapter 4 presents the successful implementation of the Particle Swarm Optimization (PSO) algorithm for determining the optimal parameters of the DC-DC Buck converter. The integration of an anti-wind-up clamping method enhances the utilization of the integral controller. By applying PSO to optimize the parameters of the PID controller, the results demonstrate promising outcomes with minimal oscillations and overshoots during significant input voltage and load step changes. The evaluation of various cost functions (ISE, IAE, ITSE, and ISTSE) reveals that all are minimized to their lowest values, affirming the robustness of the controller's parameters (K_p, K_i, and K_d). The obtained output voltage vs. time results align with the improved control parameter determination across all four cost functions.

Chapter 5 investigates an islanded DC microgrid that integrates photovoltaic (PV) and battery systems. Three controllers, namely the maximum power point controller, the battery energy source controller, and the proposed PV-based voltage regulation controller are examined to determine their ability to regulate the DC bus voltage to the desired value. The performance of the PV-based controller is evaluated under dynamic irradiance and load step changes, specifically when PV power exceeds load power in the absence of a battery. This scenario helps reduce over-charging stress on the battery. Simulation results confirm the effectiveness and robustness of the controllers in regulating the DC bus voltage.

Chapter 6 focuses on the development of a unified controller that maintains the DC-link capacitor voltage at a desired level of 48 V, regardless of input variations caused by irradiance and output variations caused by load changes. The controller ensures maximum power point (MPP) tracking during battery charging mode by setting the total control reference signal equal to the MPP voltage. In islanding mode, if the load power requirement is lower than the PV power, the controller adjusts the operating point towards the right side of the MPP, effectively reducing PV power. The unified control signal determines whether the system operates in MPPT or voltage regulation mode. If the collective control signal reference exceeds the voltage associated with MPP, the controller operates in voltage regulation mode. Conversely, if the control signal generates a voltage reference close to the MPP voltage, the controller operates in MPPT mode.

Chapter 7 examines frequency stability in a hybrid microgrid system consisting of a photovoltaic (PV) and a synchronous generator (SG), with a focus on PV's role in frequency regulation. An artificial neural network (ANN)-based V^{ref} generator is used to enable PV's participation in injecting active power. The ANN controller takes inputs such as irradiance, temperature, and a generated power reference, P^{ref}, which is adaptively adjusted to support frequency stability using a voltage-inverter (VI) method. Simulation results verified that the proposed controller significantly improves the frequency nadir along with faster settling time compared to the base-case scenario.

Chapter 8 focuses on frequency regulation in a hybrid microgrid system comprising photovoltaic (PV), battery, and synchronous generator components. The primary source for frequency regulation is the PV system, with the battery acting as a secondary source. A PV-side controller is employed to facilitate PV's participation in injecting active power for frequency regulation. Unlike traditional methods,

the proposed controller directly generates the voltage reference based on frequency deviation without using a power reference generator. The reference voltage generation adapts to load changes and utilizes battery charging and discharging to stabilize system frequency when the generated voltage reference exceeds a predefined range on the P-V curve. A scenario involving multiple load step changes is simulated to assess the effectiveness of the control algorithm. The simulation and real-time hardware simulation results demonstrate that the proposed controller effectively regulates the system frequency and rapidly reaches a steady state.

Chapter 9 presents a unified controller designed to regulate the DC-link capacitor (DC bus) voltage at the desired level, regardless of input variations caused by irradiance and output variations due to load changes. The controller achieves this by monitoring the DC bus voltage and adjusting the PV operating point to maintain system balance with minimal oscillations, leading to rapid attainment of a steady state. Proper regulation of the DC-side capacitor voltage is crucial for the AC-side voltage regulation performance of the voltage source inverter (VSI), especially in the presence of load variations. Simulation and real-time hardware simulations confirm that the proposed controller effectively regulates the DC bus voltage by dynamically adjusting the PV operating point within the appropriate region on the PV's power versus voltage curve, relative to the maximum power point (MPP).

10.2 Recommendations for Future Work

The main goals of this thesis offer substantial prospects for further investigation. The following are the identified research challenges that remain open:

1. To explore and examine of Unified Controller strategy on the development of an adaptive Droop-based control strategy for a microgrid with multiple PVs and Energy Storage Systems and extend it to multiple microgrids.
2. To apply VI-ANN-based controller to IEEE bus systems for Frequency Regulation.
3. To examine the capability of the proposed controllers for extreme conditions like zero-inertia scenarios, all the synchronous generators of the IEEE bus system will be replaced by inverter-based resources only governed by proposed controllers.
4. To explore how the proposed low-level primary controllers respond to the reference signals or set points which would be generated from deep neural network-based AC optimum power flow (OPF) for different load conditions in large IEEE bus systems.

BIBLIOGRAPHY

[1] T. O. Olowu, A. Sundararajan, M. Moghaddami, and A. I. Sarwat, "Future challenges and mitigation methods for high photovoltaic penetration: A survey," *Energies*, vol. 11, no. 7, p. 1782, 2018.

[2] K. Yan, Y. Du, and Z. Ren, "Mppt perturbation optimization of photovoltaic power systems based on solar irradiance data classification," *IEEE transactions on sustainable energy*, vol. 10, no. 2, pp. 514–521, 2018.

[3] S. K. Kollimalla and M. K. Mishra, "A novel adaptive p&o mppt algorithm considering sudden changes in the irradiance," *IEEE Transactions on Energy conversion*, vol. 29, no. 3, pp. 602–610, 2014.

[4] A. Loukriz, S. Messalti, and A. Harrag, "Design, simulation, and hardware implementation of novel optimum operating point tracker of pv system using adaptive step size," *The International Journal of Advanced Manufacturing Technology*, vol. 101, no. 5-8, pp. 1671–1680, 2019.

[5] D. Jiandong, X. Ma, and S. Tuo, "A variable step size p o mppt algorithm for three-phase grid-connected pv systems," in *2018 China International Conference on Electricity Distribution (CICED)*, pp. 1997–2001, 2018.

[6] F. A. O. Aashoor and F. V. P. Robinson, "A variable step size perturb and observe algorithm for photovoltaic maximum power point tracking," in *2012 47th International Universities Power Engineering Conference (UPEC)*, pp. 1–6, 2012.

[7] K. Saidi, M. Maamoun, and M. Bounekhla, "Simulation and analysis of variable step size p o mppt algorithm for photovoltaic power control," in *2017 In-*

ternational Conference on Green Energy Conversion Systems (GECS), pp. 1–4, 2017.

[8] X. Serrano-Guerrero, J. González-Romero, X. Cárdenas-Carangui, and G. Escrivá-Escrivá, "Improved variable step size p o mppt algorithm for pv systems," in *2016 51st International Universities Power Engineering Conference (UPEC)*, pp. 1–6, 2016.

[9] R. John, S. S. Mohammed, and R. Zachariah, "Variable step size perturb and observe mppt algorithm for standalone solar photovoltaic system," in *2017 IEEE International Conference on Intelligent Techniques in Control, Optimization and Signal Processing (INCOS)*, pp. 1–6, 2017.

[10] M. S. Sheik, "Multiple step size perturb and observe maximum power point tracking algorithm with zero oscillation for solar pv applications," in *2018 International Conference on Current Trends towards Converging Technologies (ICCTCT)*, pp. 1–5, 2018.

[11] J. Mishra, S. Das, D. Kumar, and M. Pattnaik, "A novel auto-tuned adaptive frequency and adaptive step-size incremental conductance mppt algorithm for photovoltaic system," *International Transactions on Electrical Energy Systems*, p. e12813, 2021.

[12] L. Tang, W. Xu, and C. Mu, "Analysis for step-size optimisation on mppt algorithm for photovoltaic systems," *IET Power Electronics*, vol. 10, no. 13, pp. 1647–1654, 2017.

[13] A. A. Ovalle, H. R. Chamorro, and G. Ramos, "Step-size fuzzy control to maximum power point tracking algorithms for pv microgrid arrays," in *IX Latin*

American Robotics Symposium and IEEE Colombian Conference on Automatic Control, 2011 IEEE, pp. 1–6, 2011.

[14] G. Calvinho, J. Pombo, S. Mariano, and M. d. Rosario Calado, "Design and implementation of mppt system based on pso algorithm," in *2018 International Conference on Intelligent Systems (IS)*, pp. 733–738, 2018.

[15] Y. Triki, A. Bechouche, H. Seddiki, and D. O. Abdeslam, "Adaline based mppt with indirect control mode for photovoltaic systems," in *2019 IEEE 28th International Symposium on Industrial Electronics (ISIE)*, pp. 2183–2188, 2019.

[16] S. Padmanaban, N. Priyadarshi, J. B. Holm-Nielsen, M. S. Bhaskar, F. Azam, A. K. Sharma, and E. Hossain, "A novel modified sine-cosine optimized mppt algorithm for grid integrated pv system under real operating conditions," *Ieee Access*, vol. 7, pp. 10467–10477, 2019.

[17] H. Li, D. Yang, W. Su, J. Lü, and X. Yu, "An overall distribution particle swarm optimization mppt algorithm for photovoltaic system under partial shading," *IEEE Transactions on Industrial Electronics*, vol. 66, no. 1, pp. 265–275, 2018.

[18] A. Sundararajan, T. O. Olowu, L. Wei, S. Rahman, and A. I. Sarwat, "Case study on the effects of partial solar eclipse on distributed pv systems and management areas," *IET Smart Grid*, vol. 2, no. 3, pp. 477–490, 2019.

[19] T. Simpkins, K. Anderson, D. Cutler, and D. Olis, "Optimal sizing of a solar-plus-storage system for utility bill savings and resiliency benefits," in *2016 IEEE Power Energy Society Innovative Smart Grid Technologies Conference (ISGT)*, pp. 1–6, 2016.

[20] J. Kaldellis, D. Zafirakis, and E. Kondili, "Optimum sizing of photovoltaic-energy storage systems for autonomous small islands," *International Journal of Electrical Power & Energy Systems*, vol. 32, no. 1, pp. 24 – 36, 2010.

[21] J. Li, "Optimal sizing of grid-connected photovoltaic battery systems for residential houses in australia," *Renewable Energy*, vol. 136, pp. 1245 – 1254, 2019.

[22] Y. Gupta, R. Vaidya, H. S. V. S. Kumar Nunna, S. Kamalasadan, and S. Doolla, "Optimal pv – battery sizing for residential and commercial loads considering grid outages," in *2020 IEEE International Conference on Power Electronics, Smart Grid and Renewable Energy (PESGRE2020)*, pp. 1–5, 2020.

[23] G. Ahmad, "Photovoltaic-powered rural zone family house in egypt," *Renewable Energy*, vol. 26, no. 3, pp. 379 – 390, 2002.

[24] A. Chel, G. Tiwari, and A. Chandra, "Simplified method of sizing and life cycle cost assessment of building integrated photovoltaic system," *Energy and Buildings*, vol. 41, no. 11, pp. 1172–1180, 2009.

[25] M. Lee, D. Soto, and V. Modi, "Cost versus reliability sizing strategy for isolated photovoltaic micro-grids in the developing world," *Renewable Energy*, vol. 69, pp. 16–24, 2014.

[26] M. Bortolini, M. Gamberi, and A. Graziani, "Technical and economic design of photovoltaic and battery energy storage system," *Energy Conversion and Management*, vol. 86, pp. 81–92, 2014.

[27] A. Q. Jakhrani, A.-K. Othman, A. R. H. Rigit, S. R. Samo, and S. A. Kamboh, "A novel analytical model for optimal sizing of standalone photovoltaic systems," *Energy*, vol. 46, no. 1, pp. 675–682, 2012.

[28] S. Makhloufi, "Comparative study between classical methods and genetic algorithms for sizing remote pv systems," *International Journal of Energy and Environmental Engineering*, vol. 6, no. 3, pp. 221–231, 2015.

[29] A. Mellit, S. A. Kalogirou, and M. Drif, "Application of neural networks and genetic algorithms for sizing of photovoltaic systems," *Renewable Energy*, vol. 35, no. 12, pp. 2881–2893, 2010.

[30] N. I. Haque, M. H. Shahriar, M. G. Dastgir, A. Debnath, I. Parvez, A. Sarwat, and M. A. Rahman, "Machine learning in generation, detection, and mitigation of cyberattacks in smart grid: A survey," *arXiv preprint arXiv:2010.00661*, 2020.

[31] I. Parvez, A. Sarwat, A. Debnath, T. Olowu, M. G. Dastgir, and H. Riggs, "Multi-layer perceptron based photovoltaic forecasting for rooftop pv applications in smart grid," in *2020 SoutheastCon*, pp. 1–6, IEEE, 2020.

[32] A. Debnath, T. O. Olowu, I. Parvez, M. G. Dastgir, and A. Sarwat, "A novel module independent straight line-based fast maximum power point tracking algorithm for photovoltaic systems," *Energies*, vol. 13, no. 12, p. 3233, 2020.

[33] A. Debnath, M. N. Huda, C. Saha, and S. Roy, "Determining optimum generator for south-east coast of bangladesh: Hybrid, solar-only or wind-only?," in *2018 10th International Conference on Electrical and Computer Engineering (ICECE)*, pp. 165–168, IEEE, 2018.

[34] T. O. Olowu, A. Sundararajan, M. Moghaddami, and A. I. Sarwat, "Future challenges and mitigation methods for high photovoltaic penetration: A survey," *Energies*, vol. 11, no. 7, 2018.

[35] T. O. Olowu, H. Jafari, and A. Sarwat, "Voltage-controlled series resonant dc-dc converter for solid state transformer applications," in *2021 IEEE Transportation Electrification Conference Expo (ITEC)*, pp. 237–241, 2021.

[36] S. Chtita, A. Derouich, A. El Ghzizal, and S. Motahhir, "An improved control strategy for charging solar batteries in off-grid photovoltaic systems," *Solar Energy*, vol. 220, pp. 927–941, 2021.

[37] S. Saadatmand, P. Shamsi, and M. Ferdowsi, "The voltage regulation of a buck converter using a neural network predictive controller," in *2020 IEEE Texas Power and Energy Conference (TPEC)*, pp. 1–6, IEEE, 2020.

[38] S. Chonsatidjamroen, K. Areerak, and K. Areerak, "The optimal cascade pi controller design of buck converters," in *2012 9th International Conference on Electrical Engineering/Electronics, Computer, Telecommunications and Information Technology*, pp. 1–4, IEEE, 2012.

[39] E. Köse, A. Mühürcü, G. Mühürcü, and M. N. Temiz, "Optimal control of a buck converter by using pi controller based on hsa algorithm,"

[40] A. Oshaba, E. Ali, and S. Abd Elazim, "Pi controller design using abc algorithm for mppt of pv system supplying dc motor pump load," *Neural Computing and Applications*, vol. 28, no. 2, pp. 353–364, 2017.

[41] A. Debnath, I. Parvez, M. G. Dastgir, A. Nabi, T. O. Olowu, H. Riggs, and A. Sarwart, "Voltage regulation of photovoltaic system with varying loads," in *2020 SoutheastCon*, vol. 2, pp. 1–7, IEEE, 2020.

[42] W. M. Utomo, A. Bakar, M. Ahmad, T. Taufik, and R. Heriansyah, "Online learning neural network control of buck-boost converter," in *2011 Eighth International Conference on Information Technology: New Generations*, pp. 485–489, IEEE, 2011.

[43] M. Ahmad and R. R. Ismail, "A data-driven sigmoid-based pi controller for buck-converter powered dc motor," in *2017 IEEE Symposium on Computer Applications & Industrial Electronics (ISCAIE)*, pp. 81–86, IEEE, 2017.

[44] T.-L. Liao and N.-S. Huang, "Genetic algorithm-based self-learning fuzzy pi controller for buck converter," *European transactions on electrical power*, vol. 9, no. 4, pp. 233–239, 1999.

[45] A. Debnath, M. N. Huda, C. Saha, and S. Roy, "Determining optimum generator for south-east coast of bangladesh: Hybrid, solar-only or wind-only?," in *2018 10th International Conference on Electrical and Computer Engineering (ICECE)*, pp. 165–168, 2018.

[46] P. J. d. S. Neto, T. A. d. S. Barros, J. P. C. Silveira, E. R. Filho, J. C. Vasquez, and J. M. Guerrero, "Power management strategy based on virtual inertia for dc microgrids," *IEEE Transactions on Power Electronics*, vol. 35, no. 11, pp. 12472–12485, 2020.

[47] P. Prabhakaran and V. Agarwal, "Novel boost-sepic type interleaved dc–dc converter for mitigation of voltage imbalance in a low-voltage bipolar dc microgrid," *IEEE Transactions on Industrial Electronics*, vol. 67, no. 8, pp. 6494–6504, 2020.

[48] L. Zhang, T. Wu, Y. Xing, K. Sun, and J. M. Gurrero, "Power control of dc microgrid using dc bus signaling," in *2011 Twenty-Sixth Annual IEEE Applied*

Power Electronics Conference and Exposition (APEC), pp. 1926–1932, IEEE, 2011.

[49] F. Kazhamiaka, S. Keshav, and C. Rosenberg, "Adaptive battery control with neural networks," in *Proceedings of the Tenth ACM International Conference on Future Energy Systems*, pp. 536–543, 2019.

[50] J. Schonbergerschonberger, R. Duke, and S. D. Round, "Dc-bus signaling: A distributed control strategy for a hybrid renewable nanogrid," *IEEE Transactions on Industrial Electronics*, vol. 53, no. 5, pp. 1453–146 0, 2006.

[51] K. Ameur, A. Hadjaissa, A. Cheknane, and N. Essounbouli, "Dc-bus voltage control based on power flow management using direct sliding mode control for standalone photovoltaic systems," *Electric Power Components and Systems*, vol. 45, no. 10, pp. 1106–1117, 2017.

[52] F. R. Badal, S. K. Sarker, S. R. Fahim, S. K. Das, M. R. Islam, A. Z. Kouzani, and M. A. P. Mahmud, "Robust controller design for tracking enhancement of a grid-tied pv-battery microgrid under industrial loads," *IEEE Transactions on Applied Superconductivity*, vol. 31, no. 8, pp. 1–5, 2021.

[53] J. Mírez, "A modeling and simulation of optimized interconnection between dc microgrids with novel strategies of voltage, power and control," in *2017 IEEE Second International Conference on DC Microgrids (ICDCM)*, pp. 536–541, 2017.

[54] T. Haque, T. K. Roy, F. Faria, M. M. Khatun, T. Sarkar, and A. K. Hore, "Power flow control in dc microgrids using an integral sliding mode control approach," in *2021 International Conference on Automation, Control and Mechatronics for Industry 4.0 (ACMI)*, pp. 1–5, 2021.

[55] Y. Li, F. Tang, X. Wei, F. Qin, and T. Zhang, "An adaptive droop control scheme based on sliding mode control for parallel buck converters in low-voltage dc microgrids," in *2021 IEEE 4th International Electrical and Energy Conference (CIEEC)*, pp. 1–6, 2021.

[56] Y. C. C. Wong, C. S. Lim, H. H. Goh, A. Cruden, M. D. Rotaru, and X. Kong, "An optimal secondary multi-bus voltage and reactive power sharing control based on non-iterative decoupled linearized power flow for islanded microgrids," *IEEE Access*, vol. 9, pp. 105242–105254, 2021.

[57] H. Cai, J. Xiang, and W. Wei, "Decentralized coordination control of multiple photovoltaic sources for dc bus voltage regulating and power sharing," *IEEE Transactions on Industrial Electronics*, vol. 65, no. 7, pp. 5601–5610, 2017.

[58] W. Panbao, W. Wei, X. Dianguo, L. Guihua, and L. Ming, "An autonomous control scheme for dc micro-grid system," in *IECON 2013-39th Annual Conference of the IEEE Industrial Electronics Society*, pp. 1519–1523, IEEE, 2013.

[59] U. N. PATEL and H. H. PATEL, "Dynamic droop control method for islanded photovoltaic based microgrid for active and reactive power control with effective utilization of distributed generators," *International Journal of Renewable Energy Research (IJRER)*, vol. 9, no. 2, pp. 1077–1088, 2019.

[60] V. Nougain and B. K. Panigrahi, "An integrated power management strategy of grid-tied dc microgrid including distributed energy resources," *IEEE Transactions on Industrial Informatics*, vol. 16, no. 8, pp. 5180–5190, 2020.

[61] S. Chaturvedi, D. Fulwani, and D. Patel, "Dynamic virtual impedance-based second-order ripple regulation in dc microgrids," *IEEE Journal of Emerging and Selected Topics in Power Electronics*, vol. 10, no. 1, pp. 1075–1083, 2022.

[62] O. Husev, O. Matiushkin, D. Vinnikov, C. Roncero-Clemente, and S. Kouro, "Novel concept of solar converter with universal applicability for dc and ac microgrids," *IEEE Transactions on Industrial Electronics*, vol. 69, no. 5, pp. 4329–4341, 2022.

[63] B. M. Eid, J. M. Guerrero, A. M. Abusorrah, M. Islam, *et al.*, "A new voltage regulation strategy using developed power sharing techniques for solar photovoltaic generation-based microgrids," *Electrical Engineering*, vol. 103, no. 6, pp. 3023–3031, 2021.

[64] W. Dong, S. Li, and X. Fu, "Artificial neural network control of a standalone dc microgrid," in *2018 Clemson University Power Systems Conference (PSC)*, pp. 1–5, IEEE, 2018.

[65] M. E. Elkhatib, W. Du, and R. H. Lasseter, "Evaluation of inverter-based grid frequency support using frequency-watt and grid-forming pv inverters," in *2018 IEEE Power & Energy Society General Meeting (PESGM)*, pp. 1–5, IEEE, 2018.

[66] A. Hoke and D. Maksimović, "Active power control of photovoltaic power systems," in *2013 1st IEEE Conference on Technologies for Sustainability (SusTech)*, pp. 70–77, IEEE, 2013.

[67] L. D. Watson and J. W. Kimball, "Frequency regulation of a microgrid using solar power," in *2011 Twenty-Sixth Annual IEEE Applied Power Electronics Conference and Exposition (APEC)*, pp. 321–326, IEEE, 2011.

[68] T. O. Olowu, S. Dharmasena, A. Debnath, and A. Sarwat, "Smart inverters' functionalities and their impacts on distribution feeders at high photo-

voltaic penetration," in *2021 IEEE Green Technologies Conference (GreenTech)*, pp. 97–104, 2021.

[69] M. Datta, T. Senjyu, A. Yona, T. Funabashi, and C.-H. Kim, "A frequency-control approach by photovoltaic generator in a pv–diesel hybrid power system," *IEEE Transactions on Energy Conversion*, vol. 26, no. 2, pp. 559–571, 2010.

[70] C. Zhong, H. Li, Y. Zhou, Y. Lv, J. Chen, and Y. Li, "Virtual synchronous generator of pv generation without energy storage for frequency support in autonomous microgrid," *International Journal of Electrical Power & Energy Systems*, vol. 134, p. 107343, 2022.

[71] D.-W. Zhao, M.-H. Qian, J. Ma, D.-J. Jiang, M.-S. Ding, and L. Xiang, "A decentralized frequency regulation strategy of pv power plant based on droop control," in *2018 China International Conference on Electricity Distribution (CICED)*, pp. 1824–1828, IEEE, 2018.

[72] A. Vinayagam, A. A. Alqumsan, K. Swarna, S. Y. Khoo, and A. Stojcevski, "Intelligent control strategy in the islanded network of a solar pv microgrid," *Electric Power Systems Research*, vol. 155, pp. 93–103, 2018.

[73] X. Huang, K. Wang, and G. Li, "Virtual inertia based control of two-stage photovoltaic inverters for frequency regulation in islanded micro-grid," in *2018 IEEE Power & Energy Society General Meeting (PESGM)*, pp. 1–5, IEEE, 2018.

[74] C. Zhong, Y. Zhou, and G. Yan, "A novel frequency regulation strategy for a pv system based on the curtailment power-current curve tracking algorithm," *IEEE Access*, vol. 8, pp. 77701–77715, 2020.

[75] A. F. Hoke, M. Shirazi, S. Chakraborty, E. Muljadi, and D. Maksimovic, "Rapid active power control of photovoltaic systems for grid frequency support," *IEEE Journal of Emerging and Selected Topics in Power Electronics*, vol. 5, no. 3, pp. 1154–1163, 2017.

[76] F. Conte, S. Massucco, G.-P. Schiapparelli, and F. Silvestro, "Day-ahead and intra-day planning of integrated bess-pv systems providing frequency regulation," *IEEE Transactions on Sustainable Energy*, vol. 11, no. 3, pp. 1797–1806, 2020.

[77] J. Guo, T. Chen, B. Chaudhuri, and S. Y. R. Hui, "Stability of isolated microgrids with renewable generation and smart loads," *IEEE Transactions on Sustainable Energy*, vol. 11, no. 4, pp. 2845–2854, 2020.

[78] R. Al Badwawi, W. R. Issa, T. K. Mallick, and M. Abusara, "Supervisory control for power management of an islanded ac microgrid using a frequency signalling-based fuzzy logic controller," *IEEE Transactions on Sustainable Energy*, vol. 10, no. 1, pp. 94–104, 2019.

[79] R. Zhang and B. Hredzak, "Nonlinear sliding mode and distributed control of battery energy storage and photovoltaic systems in ac microgrids with communication delays," *IEEE Transactions on Industrial Informatics*, vol. 15, no. 9, pp. 5149–5160, 2019.

[80] A. Khalid, A. Stevenson, and A. I. Sarwat, "Overview of technical specifications for grid-connected microgrid battery energy storage systems," *IEEE Access*, vol. 9, pp. 163554–163593, 2021.

[81] S. Roy, A. Debnath, M. Tariq, M. Behnamfar, and A. Sarwat, "Characterizing current thd's dependency on solar irradiance and supraharmonics profiling for

a grid-tied photovoltaic power plant," *Sustainability*, vol. 15, no. 2, p. 1214, 2023.

[82] M. Kumar and B. Tyagi, "A robust adaptive decentralized inverter voltage control approach for solar pv and storage-based islanded microgrid," *IEEE Transactions on Industry Applications*, vol. 57, no. 5, pp. 5356–5371, 2021.

[83] H.-S. Lee and J.-J. Yun, "Advanced mppt algorithm for distributed photovoltaic systems," *Energies*, vol. 12, no. 18, p. 3576, 2019.

[84] H. Lim and N. Lee, "Survey and proposal on binary search algorithms for longest prefix match," *IEEE Communications Surveys Tutorials*, vol. 14, no. 3, pp. 681–697, 2012.

[85] R. D. Nowak, "The geometry of generalized binary search," *IEEE Transactions on Information Theory*, vol. 57, no. 12, pp. 7893–7906, 2011.

[86] X. Li and M. Li, "Multiobjective local search algorithm-based decomposition for multiobjective permutation flow shop scheduling problem," *IEEE Transactions on Engineering Management*, vol. 62, no. 4, pp. 544–557, 2015.

[87] F. Meyer auf der Heide, "A polynomial linear search algorithm for the n-dimensional knapsack problem," *Journal of the ACM (JACM)*, vol. 31, no. 3, pp. 668–676, 1984.

[88] A. Marquez, J. Leon, S. Vazquez, L. Franquelo, J. Carrasco, and E. Galvan, "Binary search based mppt algorithm for high-power pv systems," in *2016 10th International Conference on Compatibility, Power Electronics and Power Engineering (CPE-POWERENG)*, pp. 168–173, IEEE, 2016.

[89] M. Zia, E. Elbouchikhi, and M. Benbouzid, "An energy management system for hybrid energy sources-based stand-alone marine microgrid," in *IOP Conference Series: Earth and Environmental Science*, vol. 322, p. 012001, IOP Publishing, 2019.

[90] D. M. S. Regis, S. P. Kumar, and G. G. Devadhas, "An optimum setting of controller for a dc-dc converter using bacterial intelligence technique," in *ISGT2011-India*, pp. 204–210, IEEE, 2011.

[91] X. Li, M. Chen, and Y. Tsutomu, "A method of searching pid controller's optimized coefficients for buck converter using particle swarm optimization," in *2013 IEEE 10th International Conference on Power Electronics and Drive Systems (PEDS)*, pp. 238–243, IEEE, 2013.

[92] J. Radosavljević, M. Jevtić, and D. Klimenta, "Energy and operation management of a microgrid using particle swarm optimization," *Engineering Optimization*, vol. 48, no. 5, pp. 811–830, 2016.

[93] J. Mei and J. L. Kirtley, "A non-cooperative game theory based controller tuning method for microgrid dc-dc converters," in *2018 IEEE Power & Energy Society General Meeting (PESGM)*, pp. 1–5, IEEE, 2018.

[94] A. Debnath, T. O. Olowu, I. Parvez, and A. Sarwat, "Step-size optimization of new straight line approximation-based mppt algorithm for photovoltaic systems," in *2021 IEEE 12th International Symposium on Power Electronics for Distributed Generation Systems (PEDG)*, pp. 1–6, IEEE, 2021.

[95] A. Debnath, T. O. Olowu, S. Roy, and A. Sarwat, "Voltage regulation and battery stress-reduction strategy for dc microgrid," in *2021 6th IEEE Workshop on the Electronic Grid (eGRID)*, pp. 01–06, 2021.

[96] A. Debnath, T. O. Olowu, S. Roy, I. Parvez, and A. Sarwat, "Particle swarm optimization-based pid controller design for dc-dc buck converter," in *2021 North American Power Symposium (NAPS)*, pp. 1–6, 2021.

[97] H. Bevrani, T. Ise, and Y. Miura, "Virtual synchronous generators: A survey and new perspectives," *International Journal of Electrical Power & Energy Systems*, vol. 54, pp. 244–254, 2014.

[98] S. Li, Y. Sun, M. Ramezani, and Y. Xiao, "Artificial neural networks for volt/var control of der inverters at the grid edge," *IEEE Transactions on Smart Grid*, vol. 10, no. 5, pp. 5564–5573, 2018.

[99] M. G. Villalva and E. Ruppert, "Analysis and simulation of the p&o mppt algorithm using a linearized pv array model," in *2009 35th Annual Conference of IEEE Industrial Electronics*, pp. 231–236, IEEE, 2009.

[100] R. Gugulothu, B. Nagu, and D. Pullaguram, "Energy management strategy for standalone dc microgrid system with photovoltaic/fuel cell/battery storage," *Journal of Energy Storage*, vol. 57, p. 106274, 2023.

VITA

ANJAN DEBNATH

2008	B.Sc., Electrical and Electronics Engineering, Bangladesh University of Engineering and Technology Dhaka, Bangladesh
2019 - 2022	M.S., Electrical Engineering Florida International University Miami, Florida
2019 - 2023	Ph.D., Electrical and Computer Engineering Florida International University Miami, Florida

A Debnath, S Roy, A Stevenson, TO Olowu, A Sarwat - "A Unified Control Strategy for Voltage Regulation in a Microgrid System" – (under-review) IEEE Transactions on Industry Applications,2023

A Debnath, TO Olowu, I Parvez, MG Dastgir, A Sarwat - "A Novel Module Independent Straight Line-Based Fast Maximum Power Point Tracking Algorithm for Photovoltaic Systems" – Energies, 2020.

A Debnath, S Roy, A Stevenson, TO Olowu, A Sarwat – "Dynamic Frequency Regulation based on Hierarchical Control of DERs in Microgrid" – (accepted) IEEE PESGM, 2023

A. Debnath, S. Roy, A. Stevenson, T. O. Olowu and A. Sarwat, "ANN-based Dynamic Frequency Regulation of PV-based Hybrid Microgrid system," 2023 IEEE Power & Energy Society Innovative Smart Grid Technologies Conference (ISGT), Washington, DC, USA, 2023, pp. 1-5, doi: 10.1109/ISGT51731.2023.10066418.

A. Debnath, S. Roy, T. O. Olowu, I. Parvez and A. Sarwat, "A Unified Controller

for Hybrid PV-Battery system with DC Microgrid Voltage Regulation in Grid-connected and Islanding-mode," 2022 IEEE Industry Applications Society Annual Meeting (IAS), Detroit, MI, USA, 2022, pp. 1-6, doi: 10.1109/IAS54023.2022.9940125.

A. Debnath, T. O. Olowu, S. Roy, I. Parvez and A. Sarwat, "Particle Swarm Optimization-based PID Controller Design for DC-DC Buck Converter," 2021 North American Power Symposium (NAPS), College Station, TX, USA, 2021, pp. 1-6, doi: 10.1109/NAPS52732.2021.9654737.

A. Debnath, T. O. Olowu, S. Roy and A. Sarwat, "Voltage Regulation and Battery Stress-Reduction Strategy for DC microgrid," 2021 6th IEEE Workshop on the Electronic Grid (eGRID), New Orleans, LA, USA, 2021, pp. 01-06, doi: 10.1109/eGRID52793.2021.9662139.

A. Debnath, T. O. Olowu, I. Parvez and A. Sarwat, "Step-size Optimization of New Straight-Line approximation-based MPPT Algorithm for Photovoltaic Systems," 2021 IEEE 12th International Symposium on Power Electronics for Distributed Generation Systems (PEDG), Chicago, IL, USA, 2021, pp. 1-6, doi: 10.1109/PEDG51384.2021.9494180.

A. Debnath, T. O. Olowu, I. Parvez and A. Sarwat, "A Binary Search Algorithm based Optimal Sizing of Photovoltaic and Energy Storage Systems," 2021 IEEE Green Technologies Conference (GreenTech), Denver, CO, USA, 2021, pp. 563-568, doi: 10.1109/GreenTech48523.2021.00094.

TO Olowu, A Debnath, I O Olasupo – "Gaussian Process Regression-based Smart Inverters' Volt-VAR Control" – (accepted), IEEE IAS Annual Meeting,2023.

A Debnath, Parvez, I., Olowu, T.O., Dastgir, M.G. and Sarwat, A., - "Voltage Regulation of Photovoltaic System with varying Loads", IEEE SouthEastConf, 2021.